Radio-frequency atomic magnetometers: an analysis of interrogation regimes

Jenelle Rajroop

A dissertation submitted in partial fulfilment

of the requirements for the degree of

Doctor of Philosophy

of

University College London.

Physics and Astronomy

University College London

May 31, 2018

I, Jenelle Rajroop, confirm that the work presented in this thesis is my own. Where information has been derived from other sources, I confirm that this has been indicated in the work.

Abstract

An atomic magnetometer is a sensor which is used to measure a magnetic field through its interaction with the atomic sample. Significant research into atomic magnetometry has led to the development of very sensitive atomic sensors capable of matching the sensitivity of the most sensitive magnetometers, superconducting quantum interference devices (SQUIDs). Because SQUIDS require cryogenics to operate, atomic magnetometers provide a sensitive, yet low-cost alternative. They have found use in many areas such as medicine, security, explosives detection and fundamental physics research.

One of the primary factors influencing sensitivity is the detuning of the probe beam from the resonant transitions of the atomic ground state. A caesium room temperature radio-frequency (rf) magnetometer is constructed and used to investigate the influence of the probe beam detuning on the magnetometer signal of the $F = 3$ and $F = 4$ ground states. The results of probing near and far from resonance revealed an off-resonant regime and two absorptive regimes. In the off-resonant regime, the atomic spins are unperturbed by the probe beam; it is a quantum non-demolition (QND) interaction. The two absorptive regimes, found when the probe beam is in the vicinity of either the $6^2S_{\frac{1}{2}}F = 3 \rightarrow 6^2P_{\frac{3}{2}}F' = 2,3,4$ or the $6^2S_{\frac{1}{2}}F = 4 \rightarrow 6^2P_{\frac{3}{2}}F' = 3,4,5$ transitions, is characterised as a non-QND interaction in which the probe beam influences the measurement.

The sensitivity of the rf magnetometer is determined to be ≈ 1.98 $\mathrm{fT}/\sqrt{\mathrm{Hz}}$. In addition, the exploration of the relationship between the signal to noise ratio (SNR) and probe beam detuning revealed that the SNR is constant with detuning but the larger the detuning, the higher the probe beam power needs to be to reach the optimum SNR.

Acknowledgements

First and foremost, I extend my sincerest gratitude to my two supervisors, Dr. Witold Chalupczak of the National Physical Laboratory (NPL) and Professor Ferruccio Renzoni of the University College London (UCL). Both have been invaluable during my years as a PhD student. I would especially like to thank Dr. Chalupczak for all his advice and assistance, as a substantial portion of my time was spent at NPL.

Special thanks go to Dr. Rafal Gartman of NPL, who was always on hand to assist me in the laboratory, and discuss unfamiliar physics concepts.

In addition, I would like to thank my mum, Joyslen, and my partner, Dr. Shahab Shahipasand, for their support, patience, understanding and encouragement.

Contents

List of Figures

List of Tables

Nomenclature

Physics Constants

ε_0	Permittivity of free space	$8.854187817 \times 10^{12} F/m$
$\hbar$	Reduced Planck constant	$1.054571800(13) \times 10^{34} Js$
μ_B	Bohr magneton	$9.274009994(57) \times 10^{24} J/T$
c	Speed of light in a vacuum inertial system	$299,792,458 m/s$
h	Planck Constant	$6.62607 \times 10^{-34} Js$
k_B	Boltzmaan constant	$1.38064852(79) \times 10^{23} J/K$

Symbols

a_s	Strength of the magnetic dipole interaction between the electron and nuclear spin
α_0	Dimensionless scalar polarisability
α_1	Dimensionless vector polarisability
α_2	Dimensionless tensor polarisability
β	Attenuation constant describing attenuation of light in a medium
β_{phase}	Phase angle between the amplitudes of the light in the x- and y-directions
$\boldsymbol{\chi}$	Electric susceptibility of the medium
$\boldsymbol{B}_0$	Primary static magnetic field

$\boldsymbol{B}_{rf}$ Weak oscillating radio-frequency (rf) magnetic field

$\boldsymbol{E}$ Electric field of atom

$\boldsymbol{F}$ The total atomic spin

$\boldsymbol{I}$ The nuclear angular momentum

$\boldsymbol{J}$ The total electronic angular momentum

$\boldsymbol{L}$ The orbital angular momentum of the electron

$\boldsymbol{M}$ The magnetisation vector in the transverse plane

$\boldsymbol{P}$ Polarisation of the medium

$\boldsymbol{S}_{ab}$ Total electronic spin of the colliding atoms, a and b

$\boldsymbol{S}_{a}$ Electronic spin of atom a

$\boldsymbol{S}_{b}$ Electronic spin of atom b

$\boldsymbol{S}_{St}$ Stokes' vector

$\boldsymbol{S}$ The spin angular momentum of the electron

Δ Detuning of the angular frequency of the probe beam from the angular frequency of the probe beam

$\Delta\nu_{FWHM}$ Full width at half maximum (FWHM) of transition, in non-angular frequency units

Δf Bandwidth in Hz over which the noise is measured

Δt Natural lifetime of the excited state

ΔV Johnson Noise

ε Coefficient that depends on the wavelength of light, its detuning from the resonant transition and the transition width

γ Atomic gyromagnetic ratio

γ_{decay} Decay rate of optical coherences

Γ_{nat} Natural linewidth

Γ_{power} Power broadened linewidth

$\hat{H}_{elec}$ Hamiltonian describing the atom in an external electric field

$\hat{H}_{int}$ Effective Hamiltonian describing the interaction between a polarised atomic medium and linearly polarised light in terms of the ground state spin

$\hat{H}_{mag}$ Hamiltonian describing the atom in an external magnetic field

λ Wavelength of light wave measured in a vacuum

λ_m Wavelength of light wave measured in medium

μ_I Nuclear moment of nucleus

μ_J Magnetic moment of electron

μ_m Magnetic dipole moment of atom

ν_0 Resonant frequency of atomic transition, in non-angular units

ν_{col} Frequency of atomic collisions

ν_{hfs} Hyperfine frequency splitting (9192MHz) of the Caesium (Cs) $F = 3$ and $F = 4$ ground states

ν_{laser} Absorbed frequency of laser

ν_L Non-angular Larmor frequency

$\nu_{non-linearZeeman}$ Frequency of separation of magnetic sublevels of the ground state due to the non-linear Zeeman effect

ω Angular frequency of the probe beam

ω_0 Angular frequency of the resonant transition

ω_1 Angular frequency of the y' and z' axes about the x axis in the rotating coordinate system

ρ_{atomic} Atomic density

$\sigma(m_J)$ Differential cross-section for excitation of magnetic sublevels with quantum number, m_J

σ_{col} Cross-section of atomic collisions

τ The time taken to acquire the measurement

τ_{spon} Spontaneous decay rate of the upper state lifetime

θ Angle of rotation of the plane of linearly polarised light

A Area of the atomic cloud

A_{if} Spontaneous decay rates from the final (f) to initial (i) states

d_{atom} Electric dipole moment of atom

E_x Amplitude of of the electric field vector in the y-direction of polarised light propagating in the z-direction

E_y Amplitude of of the electric field vector in the y-direction of polarised light propagating in the z-direction

g_F Landé g-factor

g_J Electron spin g-factor

I_1 Intensity of the probe beam hitting the first photodiode of the balanced photodetector

I_2 Intensity of the probe beam hitting the second photodiode of the balanced photodetector

I_L Intensity of light

I_{sat} Saturation intensity

k Wavenumber of of the polarised light

L Length of medium

m_{Cs} Cs atomic mass

n Refractive index of medium

N_{atoms} Total number of atoms

n_{atoms} Number density of atoms

N_{flux} Photon flux per unit time

N_{pr} Number of probe photons

R Resistance of resistor

T Temperature of moving atoms in Kelvin

T_1 Lifetime of the longitudinal magnetisation vector

T_2 Lifetime of the transverse magnetisation vector

T_{shield} Static shielding factor of magnetic shields

v_{th} Most probable speed of atoms

x Ratio of the paramagnetic interaction (Zeeman Energy) to the hyperfine separation

Chapter 1

Introduction

For many centuries, magnetometers have played an important role in the measurement of the strength and sometimes direction of magnetic fields [1]. The simplest absolute magnetometer, consisting of a permanent bar magnet suspended horizontally by a gold fibre, was devised by Carl Friedrich Gauss in 1832 [1]. Modern day magnetometers have come a long way since then thanks to numerous technological advancements, leading to the development of a wide range of sensors in use today. These include the fluxgate magnetometer, superconducting quantum interference devices (SQUIDs), the proton precession magnetometer, the helium magnetometer and of course, atomic magnetometers. A good way of characterising a magnetometer is to determine its sensitivity to magnetic fields. The field sensitivity, measured in units of $\mathrm{T}/\sqrt{\mathrm{Hz}}$, represents the precision obtained after one second of integration; this improves as the square root of the measurement time, thus detection of short-lived signals require greater sensitivity than long-lived signals [2]. Atomic magnetometers are the focus of this thesis, but to understand and appreciate their capabilities, it is useful to discuss also the other types of sensors available, and compare their sensitivities with atomic magnetometers.

The fluxgate magnetometer, used in academic and industrial applications, utilises two coils wrapped around ring cores of a highly magnetically permeable alloy to measure magnetic fields. It was originally developed in the 1940s for use in anti-submarine warfare, and after the second world war, it found use in geophysical surveys for exploration of natural resources [3]. Though its sensitivity is limited to

about 1 pT/$\sqrt{\text{Hz}}$, it is primarily used for field operation because of its portability and high measurement accuracy [2].

The proton precession magnetometer was the first magnetometer which used the same principle underlying atomic magnetometers, which is measuring the frequency of atomic spin precession. These magnetometers were developed in the 1940s and 1950s by Bloch [4, 5], and Varian and Packard [6] as an offshoot of the research involving nuclear magnetic resonance (NMR). This magnetometer consists of a coil of wire surrounding a hydrogen-containing liquid such as water, kerosene, etc. The proton, a magnetic dipole, can be polarised by the application of a magnetic field produced by a direct current (dc) in the coil. This magnetic field is orthogonal to the field to be measured. After the protons' spins are polarised, the current in the coil is abruptly switched off, and the spinning protons precess about the direction of the ambient magnetic field to be detected, at a frequency that is proportional to the field intensity. The precession is detected by magnetic induction, typically in the same coils used to generate the magnetic field which polarises the spins. The first commercial proton-precession magnetometers appeared in the 1960s and are still widely used today for many applications such as ground, marine and airborne surveys [3]. This is because the sensors can be used on a mobile platform, as they measure the field independent of orientation. The maximum sensitivity of commercial magnetometers based on proton precession is generally 0.01 nT [3].

There are two types of helium magnetometers. Optical magnetometers using ^{4}He as the atomic medium have been around since the 1960s [3]. These magnetometers use polarisation of the 2^3S_1 metastable state populated by a high-frequency discharge as opposed to atomic magnetometers which utilise ground state polarisation [7]. Colegrove, Walters and Schearer demonstrated a method for spin-exchange optical pumping of metastable helium atoms to create spin-polarized He-3 nuclei [8, 9], which led to the development of the He-3 nuclear free-precession magnetometer by Slocum and Marton in 1974 [10]. Commercially, helium magnetometers have been used in many different applications over the years, including geophysical, space exploration and military [3]. Robust and stable helium magnetome-

ters have demonstrated sensitivities approaching 40 $\mathrm{fT}/\sqrt{\mathrm{Hz}}$ [3].

Magnetometers based on superconducting quantum interference devices (SQUIDs) have been known to exhibit the greatest sensitivity (1 $\mathrm{fT}/\sqrt{\mathrm{Hz}}$) and are the greatest competitors of atomic magnetometers [11]. In 1962, Brian Josephson predicted that an electron pair could tunnel between closely spaced superconductors even with no potential difference [12]. This effect was observed by Anderson and Rowel in 1964 [13]. This discovery led to the development of the SQUID magnetometer which consists of a circulating current loop of two superconductors, separated by thin insulating layers to form two parallel Josephson junctions [14]. These junctions are sensitive to magnetic flux perpendicular to the loop, causing changes in the current flow. SQUID sensors have a large bandwidth, along with a wide and flat frequency response ranging from dc to several GHz [15], and are used in a variety of applications because of their high sensitivity. These include clinical biomagnetic applications (monitoring of the heart and brain), magnetotellurics (measuring electrical currents flowing in the earth), in paleomagnetics (where rock samples are measured for remnant field direction and density, demagnetised, then re-measured to determine the sample's chronological magnetic history), and stationary electromagnetic surveys as magnetic current sensors [15]. SQUIDs cannot be used on mobile platforms because they require cryogenic equipment which makes them bulky. In addition, the running costs are extremely high. These limitations make SQUIDs unfeasible for many portable applications, hence they are only used where the highest sensitivity is critical for successful measurements.

Atomic magnetometers have been around for more than fifty years as evidenced by the fact that the rubidium magnetometer was first used for geophysical measurements in 1957 [3]. Early atomic magnetometers utilised an alkali vapour discharge lamp in which light from the lamp passed through a glass cell containing the vapour and was focused on a photodetector on the other side of the vapour cell [16], [17]. In recent decades, the availability of inexpensive laser diodes which replaced the lamps in many of the devices has been somewhat responsible for increasing the research into atomic magnetometers because such lasers are encouraging

researchers to create compact, laser-pumped atomic sensors [15]. Recently, atomic magnetometers using microfabricated vapour cells with volumes of about 10 mm^3 have been developed. These devices are portable, with power consumption less than 200 mW and a total physics package volume less than 10 cm^3 [18], [19]. Currently, the most sensitive atomic magnetometer is the spin-exchange-relaxation-free (SERF) magnetometer. Allred et al. [20] in 2002 first presented this magnetometer which operates at zero-field to maximise the polarisation lifetime. In 2003, Kominins et al. [21] demonstrated a sensitivity of 10^{-17} $T/\sqrt{Hz}$ in a cell with volume less than 1 cm^3 using this magnetometer, with the potential to achieve sensitivity better than 1×10^{-20} $T/\sqrt{Hz}$.

Atomic magnetometers are a low cost alternative to SQUIDS since they do not require cryogenic equipment and can function at room temperature. They are able to operate in both shielded and unshielded environments. They can be manufactured from relatively inexpensive materials and have the capability to be portable. In terms of sensitivity, they have the potential to surpass that of SQUIDs. Thus, atomic magnetometers combine all the advantages of the various magnetometers discussed in this introduction without their disadvantages, thus are a very appealing option. Figure 1.1 illustrates the sensitivities of various magnetometers, together with the amplitudes of several important magnetic field signals.

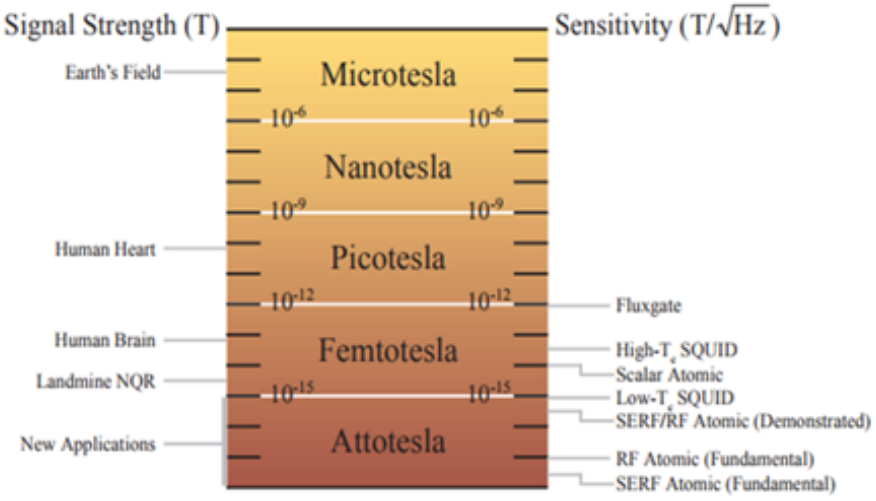

Figure 1.1: Comparison of the demonstrated sensitivity of various magnetometers, along with the amplitudes of several magnetic field signals. Image taken from [2].

Atomic magnetometers have found use in many applications, some of which will be highlighted here. One prominent application is in the field of biological magnetic studies in which detecting magnetic fields of the brain (magnetoencephalography (MEG)) and the heart (magnetocadiography (MCG)) are the primary focus. MCG has been shown to yield richer diagnostic information than traditional electrocardiography [22]. However, MCG for clinical application has been considered too expensive because magnetically shielded rooms are required, therefore, low cost sensors able to operate in unshielded environments such as atomic magnetometers represent a feasible solution. Studies into using the atomic magnetometer for MCG have produced very good results [23–29]. MEG has been used extensively for functional brain studies [30]. With the exception of atomic magnetometers, there are no other devices which can rival low critical temperature SQUIDs (Tc-SQUIDs) in sensitivity at low frequencies, in the range of interest for MEG [16]. It was demonstrated that a SERF magnetometer can be used successfully for the detection and imaging of brain activities [31].

Another area of application is the detection of NMR signals. Inductive radio-frequency (rf) pick-up coils are usually used for NMR detection, however, their sensitivity drops at low frequency, thus limiting low-field NMR applications. SQUIDs have been used for low-field NMR but as they require cryogenic cooling, they are not an advantageous alternative due to the bulky setups. Atomic magnetometers have successfully been used to measure the magnetic fields generated by nuclear magnetisation [32–34]. One of the promising NMR applications is "remote" NMR, where spin polarisation, NMR-signal encoding and detection are performed sequentially in different parts of the apparatus [35]. The most potentially useful atomic magnetomter for NMR and even magnetic resonance imaging (MRI) applications is the high-density rf magnetometer developed by Savukov et al. in 2007 [36]. The principles underlying the rf magnetometer are discussed in detail in chapter 3.

Tests of fundamental physics is another area which has benefited from atomic magnetometers because atomic magnetometers are intrinsically sensitive probes of the spin precession and hence, play an important role in tests of fundamental sym-

metries. Some of the research areas which have benefited from atomic magnetometry include the search for new fundamental spin dependent interactions such as spin-gravity coupling [37], anisotropic spin coupling [38], and detecting axion-like domain walls [39]. Another example of a fundamental application is the hunt for permanent electric dipole moments (EDMs). The permanent electric dipole moment (EDM) of a particle or composite system is a displacement between negative and positive charges for a neutral object such as an atom or the neutron, or a displacement between the centre of mass and the centre of charge for a non-neutral object such as the electron. One typical approach is to find the difference between the precession frequency of a neutral system in the magnetic field parallel and anti-parallel with the electric field; this frequency difference yields a direct measurement of the EDM [40, 41]. One of the research teams at the University of California, Berkley (UC Berkley) is currently working on using a Cs-^{129}Xe SERF co-magnetometer to search for EDMs [2, 42–44].

Soon after the first demonstration of atomic magnetometry, they were being used to measure the Earth's magnetic field with great precision. On account of these early successes, researchers at NASA began collaborating with researchers at Varian Associates in developing atomic magnetometers for space exploration [3]. The first alkali vapour magnetometer used in space was in March 1961, aboard the Explorer X satellite; but their size, mass, and power imposed significant constraints on their use in space [45]. Thus, currently, most space missions rely on fluxgate magnetometers because of their small size and power consumption [46]. However, in advanced space applications, optically pumped ^{4}He magnetometers have been the magnetometer of choice due to their relative simplicity, reliability and high absolute accuracy [46]. Recent breakthroughs in atomic magnetometry research relating to both sensitivity and size has reignited its potential in space applications [46].

Other areas which have benefited from atomic magnetometers include geophysical exploration, archaeology and military applications. As more research is undertaken into improving the sensitivity of atomic magnetometers, the number of potential applications will grow.

This thesis is intended to contribute original research to the field of atomic magnetometers by developing a portable, sensitive room temperature rf magnetometer. This magnetometer will then be used to investigate the influence of the probe beam detuning on the magnetometer signal. Chapter 2 provides the necessary background theory for the experiments described in this thesis. Chapter 3 describes the principle behind the rf and dc magnetometers, along with a discussion of the fundamental noise sources and relaxation mechanisms. In Chapter 4, the technical details of the experimental setup are discussed. Chapter 5 focuses on examining how the detuning of the probe beam affects the magnetometer signal. The sensitivity of the magnetometer is estimated in Chapter 6. Finally, Chapter 7 concludes the thesis by highlighting the important results and discusses the future of the rf magnetometer.

Chapter 2

Theory and Background

2.1 Introduction

This chapter aims to provide the background theory relevant for the experiments discussed in this thesis. Firstly, the general properties of atoms and light will be described. Then, the two types interactions between atoms and light, resonant and off-resonant, will be reviewed. Finally, the interaction of rf magnetic fields with a polarised atomic medium will be discussed.

2.2 Atomic Ground State Spin

Alkali metal atoms have a single unpaired electron, the valence electron, orbiting a core of closed electronic sub-shells, surrounding the nucleus [47]. The valence electron, together with the nucleus, is used to approximate the energy of the atom [2, 48]. Alkali metal atomic vapour typically used in atomic magnetometry are caesium (Cs), rubidium (Rb) and potassium (K).

In this project, Cs is the alkali metal atom of choice for a few reasons. Firstly, at any given temperature, Cs has an atomic density which is ten times higher than Rb [49], and at room temperature (22 °C), it has a relatively high atomic density of 0.33 $\times$ 10^{11} cm^{-3} [50], which is especially relevant because all experiments described in this project have been performed with Cs at room temperature. Comparison of the atomic vapour densities of Cs, Rb and K are shown in Appendix A. Secondly, the relevant optical transitions of Cs can easily be accessed with inexpensive laser diodes [51]. Thirdly, Cs is the heaviest stable alkali metal with only one naturally

occurring stable isotope, caesium-133, ^{133}Cs [52]. Thus, obtaining a pure sample of Cs is relatively easy because no isotopic separation is required. This contrasts with Rb and K which have two and three naturally occurring isotopes, respectively [52]. Hence, they require isotopic separation in order to obtain a pure sample.

The total atomic spin, F, is a sum of the nuclear angular momentum, I, and the electronic angular momentum, J, to give $F = I + J$. For Cs, $I = \frac{7}{2}$. The electronic angular momentum, J, is due to the spin-orbit interaction which is a coupling between the orbital angular momentum, L, of the electron and its spin angular momentum, S, to give $J = L + S$ [53].

Spectroscopic notation is a standard way in atomic physics of writing down the angular momentum quantum numbers of a state. The general form is $^{2S+1}L_J$, where $2S+1$ represents the spin multiplicity which indicates the number of degenerate states there are, L is the orbital angular momentum quantum number, written as $S, P, D, F, \ldots$, etc. for $L = 0, 1, 2, 3, \ldots$,etc, and J is the total electronic angular momentum quantum number.

Figure 2.1 illustrates the atomic structure of Cs. The Cs ground state is an "S" shell with $L = 0$ and $J = \frac{1}{2}$. Therefore, in spectroscopic notation, the Cs ground state is represented as $^2S_{\frac{1}{2}}$. The hyperfine interaction splits this ground state into two levels, $F = 3$ and $F = 4$, separated by 9192 MHz.

The first excited state of Cs is a "P" shell with $L = 1$. The spin-orbit interaction results in two values of J, $J = \frac{1}{2}$ and $J = \frac{3}{2}$, spectroscopically represented as $^2P_{\frac{1}{2}}$ and $^2P_{\frac{3}{2}}$, respectively. The energy transitions between the ground state and the $^2P_{\frac{1}{2}}$ and $^2P_{\frac{3}{2}}$ levels are termed the D_1 and D_2 transitions, respectively. The hyperfine interaction splits the $^2P_{\frac{1}{2}}$ state into two levels, $F' = 3$ and $F' = 4$, while the $^2P_{\frac{3}{2}}$ state is split into four levels, resulting in $F' = 2, 3, 4$ and 5, respectively.

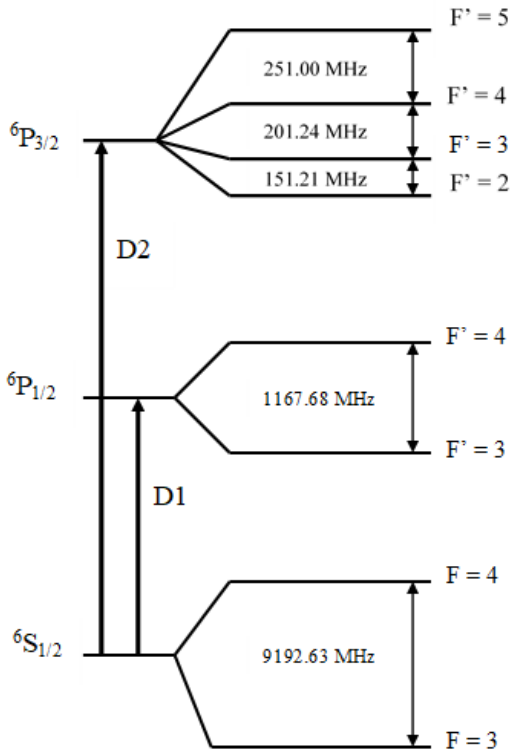

Figure 2.1: Caesium (Cs) structure showing the D_1 and D_2 transitions. Due to the non-zero nuclear spin, the hyperfine interaction splits the ground state into two levels, $F = 3$ and $F = 4$. The spin-orbit interaction splits the first excited state into two levels with $J = \frac{1}{2}$ and $J = \frac{3}{2}$. The hyperfine interaction further splits the $^2P_{\frac{1}{2}}$ state into two levels, $F' = 3$ and $F' = 4$, while the $^2P_{\frac{3}{2}}$ state is split into four levels, $F' = 2, 3, 4$ and 5.

2.2.1 Atom in an External Magnetic Field

Each hyperfine level (F) contains $2F + 1$ magnetic sublevels, m_F. These sublevels are degenerate. However, in the presence of a magnetic field, the degeneracy is lifted [53]. As the experiments described in this thesis involve detecting a magnetic field, it is useful to take a closer look at the effect the magnetic field has on the atom by looking at the Hamiltonian which describes the alkali atom in an external magnetic field. The Hamiltonian which describes an atom in an external magnetic field, $\boldsymbol{B}_0$, is:

$$\hat{H}_{mag} = ha_s \boldsymbol{I}.\boldsymbol{J} - \frac{\mu_J}{J}\boldsymbol{J}.\boldsymbol{B}_0 - \frac{\mu_I}{I}\boldsymbol{I}.\boldsymbol{B}_0 \tag{2.1}$$

Equation 2.1 is known as the Breit-Rabi equation [54]. The first term, $ha_s\boldsymbol{I}.\boldsymbol{J}$ is the hyperfine interaction as described in section 2.2 where a_s is the strength of the

magnetic dipole interaction between the electronic and nuclear spin, and h is the Planck constant. The last term in equation (2.1) always gives a small correction compared to the second term because the magnitude of the nuclear moment is $\mu_I = -2.582025(4)\mu_B$ [55], while the magnetic moment of the valence electron, an s-electron with $L = 0$, is $\mu_J = -1.001159652(41)\mu_B$ [56]. However, the relative strength between the first and second term depends on $\boldsymbol{B}_0$.

The energy shift given by perturbation theory for the Hamiltonian (equation (2.1)) is:

$$E_{F,m} = -\frac{h\nu_{\text{hfs}}}{2(2I+1} - \frac{\mu_I}{I}B_0 m_F \pm \frac{h\nu_{\text{hfs}}}{2}\sqrt{1+\frac{4m_F}{2I+1}x+x^2}, \tag{2.2}$$

where $\pm$ is used for $F = I \pm \frac{1}{2}$, m_F is the magnetic quantum number which is quantised along the magnetic field direction, $B_0 = |\boldsymbol{B}_0|$, and $\nu_{\text{hfs}} = 9192$ MHz is the hyperfine frequency splitting of the $F = 4$ and $F = 3$ ground states which is related to a by $h\nu_{\text{hfs}} = (\frac{ha_s}{2})/(2I+1)$. The parameter, x, is given by:

$$x = \frac{(-\frac{\mu_J}{J} + \frac{\mu_I}{I})B_0}{h\nu_{\text{hfs}}}. \tag{2.3}$$

Physically, x is the ratio of the paramagnetic interaction ("Zeeman energy") to the hyperfine separation [57].

For interactions with very small magnetic fields, x is small, hence there is a linear splitting of energy levels. This is known as the linear Zeeman effect. The energy difference between neighbouring sublevels is equal and results in the observation of only one transition frequency. This linearity is the same for very strong fields where the splitting of energy levels are again linear in B_0 because I and J fully decouple. This is known as the Paschen-Back effect.

However, in the intermediate region, the situation is somewhat different. As x increases due to interaction with stronger magnetic fields, the dependence of the energy levels on B_0 becomes non-linear in what is referred to as the non-linear Zeeman effect. The degeneracy between neighbouring sublevels is lifted, revealing several different transition frequencies.

The magnetic sublevels of a ground state are studied by inducing transitions with $\Delta m_F = \pm 1$. To find the energy separation between adjacent sublevels, equation (2.2) is expanded to first order in magnetic field strength, B_0, (leaving out the constant shift independent of B_0). This yields:

$$E^1_{F,m} = g_F \mu_B B_0 m_F, \tag{2.4}$$

where the Landé g-factor, $g_F = \frac{1}{\mu_B}(-\frac{\mu_I}{I} \pm -\frac{\mu_J/J + \mu_I/I}{2I+1})$.

The resonance condition for transitions between sublevels, m_F and m_{F+1} for the same F state is obtained by taking the difference between adjacent sublevels, $E(F, m_{F+1})$ and $E(F, m_F)$. To first order, this gives:

$$\nu_L = \frac{E_{m_{F+1}} - E_{m_F}}{h} = \frac{g_F \mu_B B_0}{h}, \tag{2.5}$$

where ν_L is the Larmor frequency. It is discussed in more detail in section 2.6. Equation (2.5) is true as long as the energy levels are a linear function of B_0.

To calculate the non-linear Zeeman (NLZ) effect, it is sufficient to do the approximation $\mu_I = 0$. Therefore, the resonant transition frequency for adjacent sublevels, $E(F, m_{F+1})$ and $E(F, m_F)$, expanded to first order is:

$$\nu_L = \frac{g_F \mu_B B_0}{h} = -\frac{\mu_J/J}{h(2I+1)} B_0 = \frac{g_J \mu_B B_0}{h(2I+1)}, \tag{2.6}$$

where $g_J = -\frac{\mu_J/J}{\mu_B}$ is the electron spin g-factor.

The resonance frequencies correct to second order in B_0 are found to be:

$$\nu_L = \frac{g_J \mu_B B_0}{h(2I+1)} - \frac{2B_0^2 \overline{m_F} (g_J \mu_B)^2}{h^2 (2I+1)^2} = \nu_L - \frac{\nu_L^2}{\nu_{\text{hfs}}}(2m_F + 1). \tag{2.7}$$

where the mean m_F quantum number is $\overline{m_F} = m_F + \frac{1}{2}$ [58]. From equation (2.7), the separation, ν_{NLZ}, between two neighbouring sublevels with $\Delta m_F = \pm 1$ is given by the quadratic term:

$$\nu_{NLZ} = \frac{2\nu_L^2}{\nu_{\text{hfs}}}. \tag{2.8}$$

The experiments in this thesis have been carried out in the presence of magnetic fields where the linear and non-linear Zeeman effects dominate. Figure 2.2 shows the difference between the linear and non-linear Zeeman effects in the $F = 4$ ground state.

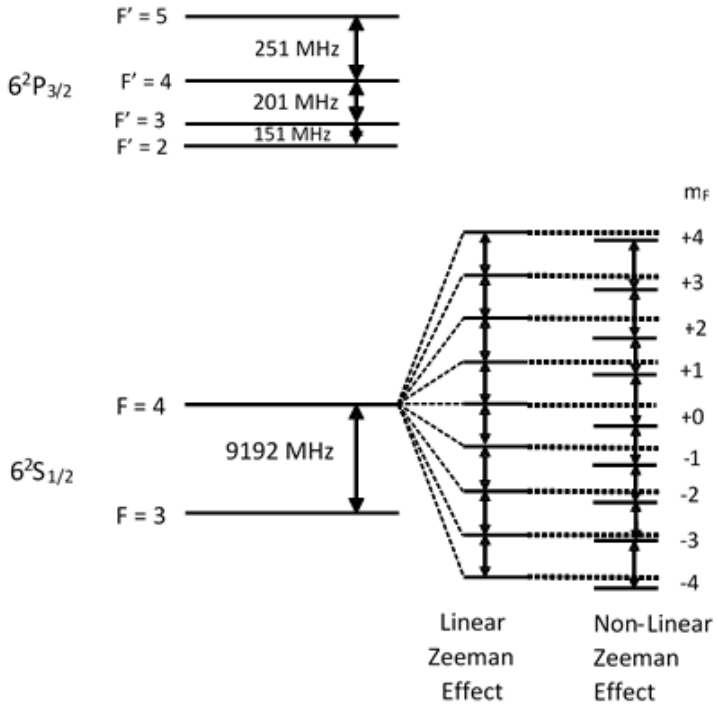

Figure 2.2: Energy diagram illustrating the linear and non-linear Zeeman effects in the $F = 4$ ground state. In the linear Zeeman effect, the energy difference between the adjacent magnetic sublevels is equal, therefore, the various components all appear at the same transition frequency. In the non-linear Zeeman effect, the non-equal energy differences between the adjacent sublevels result in the observation of several different transition frequencies.

It is convenient to describe the atomic system in a static magnetic field using the collective atomic spin [59]:

$$F = \sum_{i=1}^{N_{atoms}} f^{(i)}. \tag{2.9}$$

where N_{atoms} is the total number of atoms and $f^{(i)}$ is the spin of the i^{th} atom [2]. The component of F parallel to the magnetic field, the quantisation axis, (longitudinal magnetisation of the medium), is defined by the population imbalance of the ground

state sublevels [60]. The component of F perpendicular to the magnetic field (the transverse magnetisation of the system) is represented by ground state coherences (a linear superposition between sublevels) [60].

2.3 Broadening Effects

The linewidth is defined as the width, typically the full width at half maximum (FWHM), of its optical spectrum. The width of a spectral line is affected by factors such as natural broadening from spontaneous emission, Doppler broadening due to atomic motion, collisional broadening due to atomic density, and power broadening from intense pump and probe beams [61]. The effect of each of these broadening mechanisms will be discussed in this section.

2.3.1 Natural Broadening

Any population in the excited state decays to the ground state by spontaneous emission, emitting photons in all directions. As a consequence of the Heisenberg uncertainty principle:

$$\Delta E \Delta t \sim \hbar. \tag{2.10}$$

The energy level of an excited state can never be determined precisely because its lifetime, Δt, is finite. The uncertainty in Δt is the natural lifetime of the excited state, $\Delta t = \tau_{nat}$. The uncertainty in frequency is given by: $\Delta \nu_{un} = \frac{\Delta E}{2\pi\hbar}$. Thus, the width of the spectral line is broadened over a natural linewdith, Γ_{nat}, given by [2, 62]:

$$\Gamma_{nat} = 2\pi\Delta\nu_{un} = \frac{1}{\tau_{nat}}. \tag{2.11}$$

The spectral distribution characterised by Γ_{nat} has a Lorentzian line profile expressed as:

$$\phi(\nu) = \frac{\Gamma_{nat}}{4\pi^2} \frac{1}{(\nu - \nu_0)^2 + (\frac{\Gamma_{nat}}{4\pi^2})^2}. \tag{2.12}$$

where Γ_{nat} is related to the spontaneous decay rates, A_{if}, of all excited states, i, into all lower states, f, through $\Gamma_{nat} = \sum_f A_{if}$, and ν_0 is the centre frequency of the transition.

For the D1 and D2 transitions in alkali atoms, the natural linewidth, Γ_{nat}, is about $4-6$ MHz [2].

2.3.2 Collisional or Pressure Broadening

When an atom with energy levels, E_i and E_k, collides with other atoms or ions, the electron energy levels will be shifted. The energy shift depends on the structure of the electron shell of both colliding atoms and on the mutual distance between the atoms' centre of masses. The magnitude of this effect is dependent on the frequency of such collisions, which itself is dependent on the number density, n_{atoms}, of perturbing atoms or molecules. The frequency of collisions can be estimated from:

$$\nu_{col} = v_{th} n_{atoms} \sigma_{col}, \tag{2.13}$$

where $v_{th} = \sqrt{2k_B T/m_{Cs}}$ is the most probable thermal speed of the atoms, k_B is the Boltzmann constant, m_{Cs} is the Cs atomic mass, T is the temperature of the moving atoms and σ_{col} is the cross-section for collisions. The line profile is again Lorentzian, just like the case of natural broadening (equation (2.12)). The effects of natural and collisional broadening can be combined to give an effective linewidth, $\Gamma_{eff} = \Gamma_{nat} + 2\nu_{col}$, with the resulting line profile expressed as:

$$\phi(\nu) = \frac{\Gamma_{eff}}{4\pi^2} \frac{1}{(\nu-\nu_0)^2 + (\frac{\Gamma_{eff}}{4\pi^2})^2}. \tag{2.14}$$

2.3.3 Doppler Broadening

The random thermal motion of absorbing Cs atoms leads to small variations in the absorbed frequency of the laser, ν_{laser}, due to the Doppler effect. When the atom is moving towards or away from the laser, it will see radiation that is blue or red-shifted, respectively. An atom stationary in the rest frame of the laser will absorb radiation of resonant frequency, ν_0. However, an atom moving towards the laser and seeing blue shifted radiation will only be able to absorb radiation at a frequency less than ν_0. Similarly, an atom receding from the laser will only absorb radiation

greater than ν_0. The Doppler effect will shift ν_{laser} toward:

$$\nu_{laser} = \nu_0(1 \pm \frac{v_z}{c}). \tag{2.15}$$

where v_z is the velocity component of the absorbing atom along the line of sight of the laser beam which in this case is the z-direction, ν_0 is the resonant frequency of the transition and c is the speed of light.

Therefore, there will be an ensemble of atoms at different velocities absorbing a range of laser frequencies, and the Doppler broadened linewidth measured as the FWHM is found to be:

$$\Delta\nu_D = 2\frac{\nu_0}{c}\sqrt{\frac{2k_BT}{m_{Cs}}ln\,2}. \tag{2.16}$$

where k_B is the Boltzmann constant, T is the temperature of the moving atoms in Kelvin, ν_0 is the resonant frequency of the transition and m_{Cs} is the Cs atomic mass. At room temperature, the Doppler-broadened linewidth, $\Delta\nu_D$, is significantly larger than the natural linewidth, Γ_{nat}.

2.3.4 Power Broadening

Power broadening is defined as line broadening of atomic energy levels caused by the presence of light [63]. It occurs because the on-resonance absorption in the centre of the linewidth profile is saturated at much lower intensities than the off-resonant wings [63]. Hence, with increasing intensity, absorption in the wings rises faster than absorption in the centre, leading to a broadening of the spectral profile. The power broadened linewidth is given as:

$$\Gamma_{power} = \Gamma_{nat}\sqrt{1 + \frac{I}{I_{sat}}}. \tag{2.17}$$

where I is the laser intensity and I_{sat} is the saturation intensity. I_{sat} is the intensity at which half the atomic population is in the excited state and half in the ground state so incoming photons have equal probability of exciting atoms in both levels. I_{sat} is given by:

$$I_{sat} = \frac{\pi}{3}\frac{hc\Gamma_{nat}}{\lambda^3}. \tag{2.18}$$

where h is the Planck constant, c is the speed of light, Γ_{nat} is the natural linewidth and λ is the wavelength of the light. The saturation intensity of Cs is $I_{sat} = 1.1$ mW/cm^2 [47].

2.4 Polarisation States of Light

Light carries energy, linear momentum and angular momentum which is associated with the polarisation state of light [64, 65]. The experiments discussed in this thesis all involve the interaction of polarised light with atomic spins. Therefore, it is convenient to define the different types of polarisation states using the Stokes' vectors [66, 67]. The Stokes' vector, $\boldsymbol{S}_{St} = (S_1, S_2, S_3)$, for a pulse of light, propagating in the z-direction is defined as:

$$S_1 = E_x^2 - E_y^2, \tag{2.19}$$

$$S_2 = 2E_xE_y \cos\beta_{phase}, \tag{2.20}$$

$$S_3 = 2E_xE_y \sin\beta_{phase}. \tag{2.21}$$

where E_x is the amplitude of the light in the x-direction, E_y is the amplitude in the y-direction and β_{phase} is the phase angle between the two components. S_1 represents linear polarisation which can either be in the x- or y-directions. S_2 describes $\pm 45°$ linear polarisation between E_x and E_y. S_3 describes circular polarisation which can either be right-handed (σ_-) or left-handed (σ_+). The various polarisation states are shown in Figure 2.3.

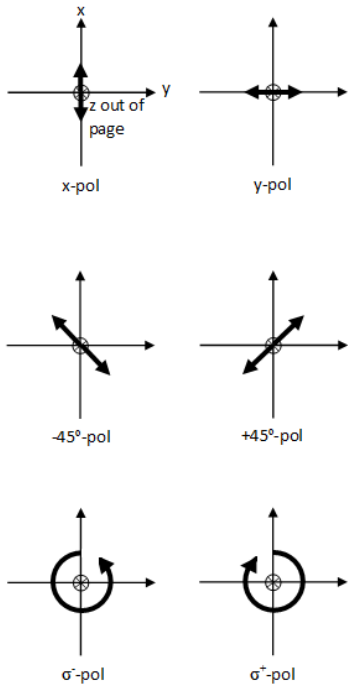

Figure 2.3: The different ways of describing the polarisation state of light.

2.5 Interaction between Polarised Light and Atomic Spins

Any coherent interaction between light and atoms needs to conserve energy, linear momentum and angular momentum [68]. In atomic magnetometry, the focus is on: (1) the transfer of angular momentum to atoms (optical pumping) and (2) the mapping of the atomic state onto the light polarisation (Faraday effect). The former case benefits from a resonant interaction while the latter from an off-resonant interaction. These two interactions will be the subjects of discussion in this section.

2.5.1 Resonant Interaction

Optical pumping changes the population distribution among the Zeeman sub-levels of the ground state atoms through transfer of angular momentum [51, 69–71]. In the experiments performed in this thesis, circularly polarised light, referred to as the pump beam, is used to perform optical pumping.

To have a better understanding of this process, the case where photons are

resonant with the $6^2S_{\frac{1}{2}}F = 4 \rightarrow 6^2P_{\frac{3}{2}}F' = 3$ transition will be considered. It is assumed to be a closed transition, in which all atoms that are excited to the upper state return to the initial state by spontaneous decay [72]. When an atom absorbs a resonant photon, the angular momentum of the photon is transferred to the atom because of angular momentum conservation. So, a σ_+ photon will cause a ground state m_F atom to jump to an excited state magnetic sublevel with $m_{F'} = m_F + 1$. From the excited state, the atom can spontaneously decay back down to the ground state via one of three possible decay channels [73]. The selection rule which governs this process is $\Delta m_F = 0, \pm 1$ because the emitted photon can have any polarisation state. Using Figure 2.4 to illustrate optical pumping, if an atom is initially in the $F = 4$, $m_F = 0$ state, the resonant photon will excite the atom to the $F' = 3$, $m_F = 1$ state. From here, it may decay to the $F = 4$, $m_F = 0$, 1, 2 states. This leads to an overall change of the ground state m_F value by 0, $+1$, or $+2$. The probabilities for the absorption and the different decay channels are determined by their Clebsch-Gordan coefficients [74].

Hence, there is a finite probability that the atom will decay to a larger m_F sublevel. And, if the pumping process is repeated several times, the atom will eventually occupy the outermost state, $F = 4$, $m_F = 4$. When this happens, the optical pumping process stops because there is no corresponding state in the excited level available for transition. For this reason, the atoms in the outermost state, or stretched state, are called dark states due to their inability to absorb light [51].

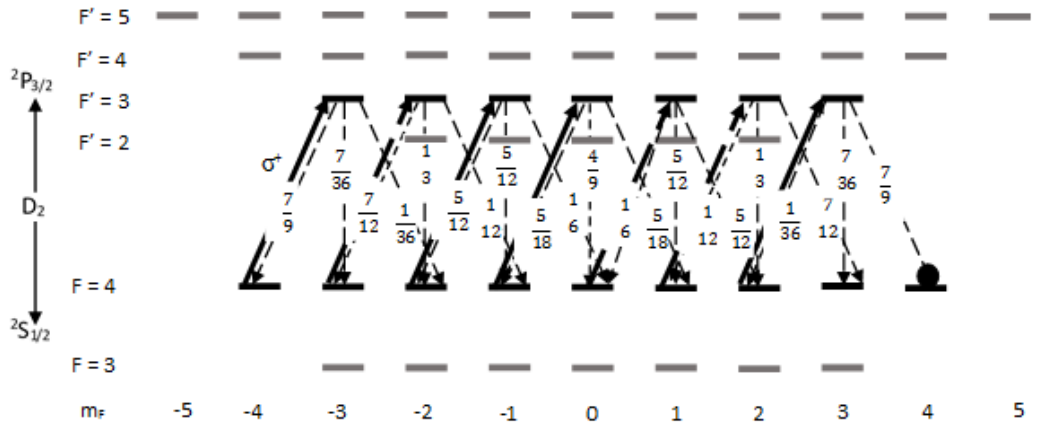

Figure 2.4: Diagram illustrating optical pumping on a closed D_2 line transition. σ^+ photons resonant with the $6^2S_{\frac{1}{2}}F = 4 \rightarrow 6^2P_{\frac{3}{2}}F' = 3$ transition, will cause $F = 4$ ground state m_F atoms to jump to the $F' = 3$ excited state magnetic sublevel with $m_{F'} = m_F + 1$. Atoms will spontaneously decay back to the $F = 4$ ground state level via one of three possible decay channels because $\Delta m_F = 0, \pm 1$. The probabilities for the absorption and the different decay channels are determined by their Clebsch-Gordan coefficients. Eventually, after many pumping cycles, atoms will accumulate in the outermost state (the stretched state) and cannot absorb any more photons. Therefore, orientation is produced within the ground state as the atomic spins are aligned along the same direction as the pump beam which is parallel to the static magnetic field. Light grey bars represent unperturbed energy levels.

The imbalance in the populations of the Zeeman sublevels as a result of optical pumping using circularly polarised light means that the ensemble of atoms possesses a net angular momentum, which manifests as a longitudinal magnetisation of the medium. This is known as orientation, and in terms of the total electronic angular momentum quantum number, J, is defined as [75, 76]:

$$< O_o >= \sum_{m_J} |\sigma(m_J)|^2 \frac{m_J}{\sqrt{J(J+1)}}. \tag{2.22}$$

where $\sigma(m_J)$ is the differential cross section for excitation of the magnetic sublevels with quantum number, m_J. An oriented distribution of atomic spins is one in which the spins have both a preferred axis and a preferred direction [77].

When optical pumping is done by linearly polarised light, the atomic ensemble possesses no net angular momentum and is invariant under a rotation of the symme-

try axis (the direction of propagation of the beam) [75]. This is due to the balance of the populations in the Zeeman sublevels, and is known as alignment [75–77], which again can be defined in terms of J [75, 76]:

$$< A_o >= \sum_{m_J} |\sigma(m_J)|^2 \frac{[3m_J^2 - J(J+1)]}{J(J+1)}. \tag{2.23}$$

An aligned distribution of atomic spins is one in which the spins have a preferred axis but no preferred direction [77].

In the experiments discussed in this thesis, the focus is on producing orientation within the ground state so that atomic spins are aligned along the same direction as the magnetic field.

2.5.1.1 Indirect Optical Pumping

In reality, the $6^2S_{\frac{1}{2}}F = 4 \rightarrow 6^2P_{\frac{3}{2}}F' = 3$ transition is not a closed transition. Some of the atoms in the excited state will inevitably escape to the $F = 3$ ground state. Usually, another laser, known as the repump laser, is employed to transfer atoms from the $F = 3$ ground state to the $F = 4$ ground state. One significant disadvantage of this method in applications which rely on rf magnetic fields to create coherences between magnetic sublevels of the ground state is the power broadening occurring due to the resonant optical interaction with states involved in the rf transitions [59, 78, 79].

The National Physical Laboratory (NPL) has demonstrated a novel technique called indirect optical pumping whereby off-resonant pumping, in combination with spin exchange collisions (SEC), enable a high degree of spin polarisation in a low density alkali metal vapour. SEC are collisions between two atoms with electrons having opposite spins, whereby the total atomic spin can be conserved but the individual electron spins are reversed. SEC are discussed in more detail in chapter 3, section 3.3.5.1. In their paper, Chalupczak et al. [78] demonstrated that optically pumping the $F = 3$ ground state results indirectly in atomic spin orientation in the $F = 4$ state, allowing observation of the relevant narrow rf resonances . The influence of SEC on the results of optical pumping is different for low and high powers.

Here, the theory and main findings from the paper are summarised.

In such a scheme, one laser is used. It is tuned to a transition, involving the ground state that is of no interest. It will be assumed that like in section 2.5.1, the goal is to put most of the atoms in the outermost sublevel of the $F = 4$ ground state. Hence, the laser is tuned to the $6^2S_{\frac{1}{2}}F = 3 \rightarrow 6^2P_{\frac{3}{2}}F' = 2$ transition.

At low light powers ($< 1\ \mu W$), it can be assumed that the $6^2S_{\frac{1}{2}}F = 3 \rightarrow 6^2P_{\frac{3}{2}}F' = 2$ transition is a closed transition so regular optical pumping should only alter the population of the $F = 3$ ground state as described in section 2.5.1, while the $F = 4$ ground state sublevels should be left unperturbed, therefore exhibit a flat population distribution. However, Chalupczak et al. [78] observed that a population imbalance builds up in the $F = 4$ ground state, which replicates that produced in the $F = 3$ ground state by optical pumping. This occurs because after light generates orientation in the $F = 3$ ground state, SEC which involve all atoms, then distribute the overall angular momentum (or orientation) among both hyperfine manifolds. This SEC process is referred to as SEC replication. The results from the experiment are shown in Figure 2.5.

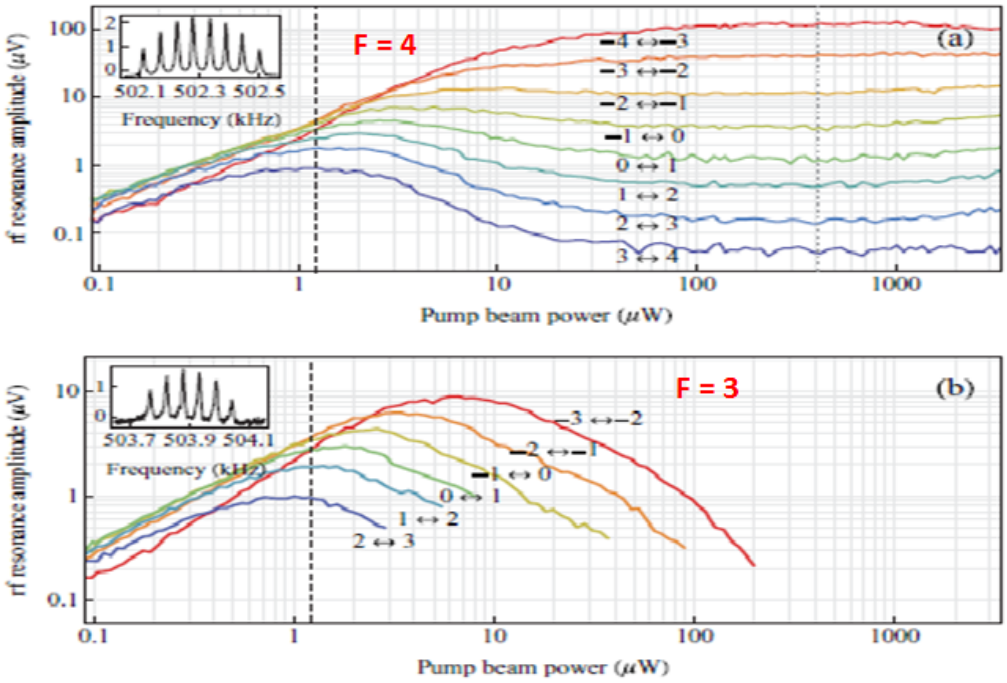

Figure 2.5: Results from Chalupczak et al. [78] showing how orientation indirectly builds up in the $F = 4$ ground state as a consequence of directly pumping the $F = 3$ ground state, off-resonant population pumping from the F = 3 to the F = 4 state, and SECs. At low light powers ($< 1\ \mu W$), orientation builds up in the $F = 4$ ground state because after orientation is produced in the $F = 3$ ground state by optical pumping, SEC then distributes the overall angular momentum among both hyperfine manifolds. At higher powers (($> 1\ \mu W$), orientation in the $F = 4$ ground state builds up because of SEC recycling and transfer pumping from $F = 3$ to $F = 4$ [78]. Insets show the rf spectra taken with a pump power of 0.1 μW for the two ground states. Image is taken from [78].

At higher light powers ($> 1\ \mu W$), the $6^2S_{\frac{1}{2}} F = 3 \rightarrow 6^2P_{\frac{3}{2}} F' = 2$ transition can no longer be considered a closed transition, so atoms can be excited to the $F' = 3$ and $F' = 4$ states according to quantum mechanics selection rules. By spontaneous emission, atoms in these states can directly decay to the $F' = 4$ ground state. Hence, there is a transfer of population from the $F = 3$ ground state to the $F = 4$ ground state. The depletion of all the sublevels in the $F = 3$ ground state implies that all the sublevels of the $F = 4$ ground state should increase. However, this was not the case as only the outer sublevels showed an increase. This is again attributed to SEC which operate under different conditions and reveal new features. The light disturbs the population balance between both ground state levels such that the $F = 4$ ground

state exceeds $F = 3$. SEC will then transfer atoms from $F = 4$ to $F = 3$, but there is some selectivity. Not all of the $F = 4$ magnetic sublevels are equally prone to be brought back to $F = 3$ because the effective SEC relaxation rates vary significantly among the sublevels, with the stretched state having the longest relaxation rate. So, an atom which is transferred from $F = 4$ to $F = 3$ will be subjected to intense optical pumping cycles before being transferred to the $F = 4$ ground state. There, it will most likely occupy a non-stretched sublevel so SEC will transfer it back to $F = 3$ where the optical pumping process repeats until the atom finally reaches the outermost state of $F = 4$. Once there, it is preserved from SEC relaxation for a very long time. This selectivity of SEC relaxation allows an accumulation of atoms in the stretched or outermost state because of the long SEC relaxation rate and the speeding up of pumping in the other $F = 4$ sublevels. This SEC mechanism is referred to as SEC recycling. The combination of optical pumping and SEC recycling puts most of the atoms in the stretched state, resulting in a high degree of orientation. The results of the high intensity regime are displayed in Figure 2.5. A schematic illustration of the two SEC mechanisms for the two intensity regimes is shown in Figure 2.6.

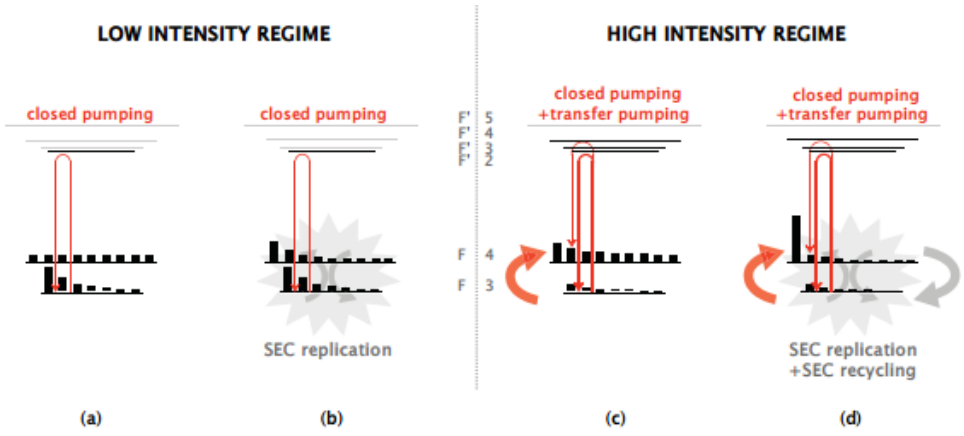

Figure 2.6: Schematic illustration of the distinct SEC contributions to the optical pumping mechanism for the two light intensity regimes. Image taken from [78].

Narrowing of the linewidths became more pronounced in the high intensity regime, when the medium approached a high degree of orientation. It was observed that the most dominant resonance narrowed by about 5 Hz from its initial

value in the low intensity regime. This comes from the buildup of orientation in the stretched state and is known as light narrowing. Light narrowing can be described as a substantial narrowing of the magnetic resonance linewidth with increasing pump power. Increasing the pump intensity results in nearly full atomic polarisation in the medium as almost all of the alkali atoms are in the stretched state, that is, they are all oriented in the same direction. When two atoms in this state undergo a SEC, both atoms will have the same orientation at the end of the collision as before the collision. There is no chance for the atoms to switch hyperfine levels. Therefore, the phase of the transverse precessing component is preserved and results in a narrowing of the linewidth.

The combination of high orientation and narrow resonance lines creates an opportunity for enhanced sensitivity of rf magnetometers. With standard optical pumping, increasing the pump power gives a larger signal amplitude but linewidth broadens as well. Implementation of indirect pumping combined with SEC addresses simultaneously two aspects relevant to the sensitivity of the rf magnetometer: (1) it depletes the $F = 3$ state so that more atoms can contribute to the signal amplitude and (2) it creates a high degree of orientation in the $F = 4$ state, which leads to narrowing of the largest rf resonances and improved signal to noise ratio (SNR) [78].

2.5.2 Off-Resonant Interaction

An off-resonant interaction represents the dispersive nature of the coupling between the polarised light and atoms [80]. Here, the light interacts with the atomic energy levels through the AC Stark shift, causing a shift in the atomic energy levels. Because the frequency of the light is far from the transition frequency, spontaneous emission and absorptive effects can be neglected.

This section will look at how the AC Stark shift arises and the effect the polarisability has on the atomic spins. Then, attention will be turned to an effective Hamiltonian which is useful in describing the interaction between a linearly polarised beam and a polarised atomic medium.

2.5.2.1 AC Stark Shift

Figure 2.7: Diagram illustrating the light shifts in the ground state of an alkali atom. Energy levels are not to scale. Light grey bars represent unperturbed energy levels.

The Stark shift is the electric analogue to the Zeeman effect in which the splitting of atomic spectral lines is a result of an externally applied constant electric field [81]. When the atom's energy levels are under the influence of an oscillating electric field (e.g a laser field), the phenomenon is known as the AC Stark shift or light shift. The first detailed experiments into light shifts were performed by Arditi and Carver in 1961 [82]. The presence of an intense far-detuned electric field shifts the energy levels of the atoms. The electric dipole moment, d_{atom}, of the atom interacts with the electric field of the probe beam according to the following Hamiltonian [72]:

$$\hat{H} = -d_{atom}\boldsymbol{E}. \tag{2.24}$$

where $\boldsymbol{E}$ is the electric field.

Generally speaking, the AC Stark shift depends on three factors: the intensity of the light, the polarisation of the field and the dynamical polarisability of the atomic state [83]. It is the polarisability of an atom which governs its response to an applied electric field. In 1967, Happer and Mathur showed that by exploiting the rotational symmetry of the interaction of the light with atoms, the total light shift can be divided into three classes according to the geometry or symmetry of the interaction of the light with atoms: the scalar, vector and tensor terms [84]. The total light shift (Figure 2.7), δE, is represented by a single operator in which each

term is categorised according to its effect on the atomic ground state [84]:

$$\delta E = \delta E_0 + h\delta a_s \boldsymbol{I}.\boldsymbol{J} - \mu_m \delta \boldsymbol{H} + \delta E_2. \tag{2.25}$$

The centre-of-mass light shift (δE_0) is an equal displacement of all the atomic ground-state sublevels; the atom is shifted as a whole [85]. The hyperfine light shift ($h\delta a_s \boldsymbol{I}.\boldsymbol{J}$) is equivalent to the change in the magnetic-dipole coupling constant, causing the hyperfine transition frequencies to change. Both these quantities are scalar in nature and do not depend on the light polarisation.

The quantity, $\mu_m \delta \boldsymbol{H}$, is called the vector light shift and is thought of as an interaction of the magnetic dipole-moment, μ_m, of the atom with an effective magnetic field, $\delta \boldsymbol{H}$, directed parallel or anti-parallel to the the light propagation direction [86]. Residual circular polarisation of the probe beam is made up of a superposition of two incoherent σ^+ and σ^- polarised beams, which produces the effective magnetic field along the light propagation direction. The shift is linear in m_F.

The last term in equation (2.25) is called the tensor light shift. It is equivalent to the electric field of the probe beam, applied to the atoms, which results in an induced dipole, existing perpendicular to the electric field. Normally, in alkali metals with a low atomic number, Z, the tensor light shift is negligible compared to the second and third terms in equation (2.25), because of the small excited state hyperfine structure. However, in alkali atoms such as Cs and Rb, the first excited state structure is well resolved under the right conditions and this makes the tensor light shift non-negligible [84]. The tensor interaction changes the frequencies of the individual transitions between neighbouring sublevels thanks to the quadratic dependence on m_F [87]:

$$\Delta E_m^{LS} = h\varepsilon(3\cos^2\phi - 1)[3m_F^2 - F(F+1)]I_L. \tag{2.26}$$

where I_L is the light intensity, ϕ is the angle between the initial polarisation and the magnetic field, and ε is a coefficient that depends on the wavelength of light, its detuning from the transition, and the transition width. The m_F^2 dependence leads

to unequal energy differences between neighbouring sublevels, thus the signal contains components at different frequencies. The light shift can be varied by changing the light frequency, intensity and the angle, ϕ [87].

2.5.3 The Effective Hamiltonian

To determine what happens in an off-resonant interaction between polarised atomic spins and a linearly polarised probe beam, an effective Hamiltonian is used to describe the interaction in terms of the ground state spin. Details of the derivation of this effective Hamiltonian have been provided by Julsgaard [80]. Here, the simplified version is quoted for brevity:

$$\hat{H}_{int} = C \int_0^L (\alpha_0 E^2(z,t) + \alpha_1 S_3(z,t) F_z(z,t) + \alpha_2 D) \rho_{atomic} A dz. \tag{2.27}$$

where A is the area of the atomic cloud, ρ_{atomic} is the atomic density, F_z is the component of the polarised atomic spin vector, $\boldsymbol{F}$, in the z-direction and C and D are constants. The light is assumed to propagate along the z-direction and goes from 0 to L, where L is the length of the medium. α_0, α_1, and α_2 are the dimensionless scalar, vector and tensor polarisabilities which are functions of the detuning, Δ, defined as:

$$\Delta = \omega - \omega_0. \tag{2.28}$$

where ω_0 is the resonant transition frequency and ω is the probe frequency. Red (blue) detuning refers to when the probe laser frequency is less (greater) than the resonance frequency, that is, $\omega < \omega_0$ ($\omega > \omega_0$) [88].

The first term in equation (2.27) containing the scalar polarisability, α_0, will produce a scalar shift of all ground state atoms, proportional to the photon density. This term is of no interest because it is common to all sublevels in the ground state.

The principal relevant term from equation (2.27) is the second term. This term containing the vector polarisability, α_1, produces a rotation in which the Stokes vector, $\boldsymbol{S}_{St}$, will be rotated around the z-axis. The rotation will be proportional to F_z. The $\sigma^{\pm}$ components of S_3 experience a difference in refractive index due to F_z which leads to a phase shift between the two components and results in a rotation

of the polarisation of $\boldsymbol{S}_{St}$. For small rotation angles, the components of $\boldsymbol{S}_{St}$ is:

$$S_1^{out} = S_1^{in}, \tag{2.29}$$

$$S_2^{out} = S_2^{in} + bF_z(t)S_1(t), \tag{2.30}$$

$$S_3^{out} = S_3^{in}. \tag{2.31}$$

where $\boldsymbol{S}^{in}$ and $\boldsymbol{S}^{out}$ denote the light before and after the interaction, and b which is proportional to α_1, is a constant that describes the strength of the interaction. The S_1 component of the Stokes vector, $\boldsymbol{S}_{St}$, is rotated around the z-axis by $bF_z(t)$ because F_z is imprinted on the output of S_2. This is known as the Faraday effect.

In the standard Faraday effect, the plane of polarisation of a linearly polarised probe beam propagating through the medium is rotated when the medium is subject to a magnetic field, applied in the direction of light propagation. Linearly polarised light is defined as light in which the electric field vector is confined to a single plane along the direction of propagation. It can be thought of as a superposition of two orthogonal circularly polarised fields. The refractive index, n, associated with the medium of atomic spins is the same for both components. The splitting of energy levels in the presence of a magnetic field leads to a difference between the resonance frequencies for the two circular polarisations, which displaces the individual dispersion curves. The medium is said to be circularly birefringent. The difference between n_+ and n_- leads to a difference in phase velocities for the two components which manifests as a rotation of the plane of polarisation.

To understand this phenomenon, a simple two-level atomic model will be used to demonstrate how the atoms rotate the plane of polarisation. The derivation presented here largely follows that given in [89]. The two oppositely directed circularly polarised electric fields of equal amplitude, propagating independently through the medium in the $+z$-direction can be mathematically represented as:

$$\boldsymbol{E}_{\pm}(z,t) = E_0(\hat{\boldsymbol{x}} \pm i\hat{\boldsymbol{y}})\ exp\ i(kz - \omega t), \tag{2.32}$$

The incident field may be written as a superposition:

$$\boldsymbol{E}(0,t) = \boldsymbol{E}_+(0,t) + \boldsymbol{E}_-(0,t) = 2E_0\hat{\boldsymbol{x}}\ exp\ i(k0 - \omega t), \tag{2.33}$$

where E_0 is the initial amplitude of the wave, ω is the angular frequency of the wave and t is a given point in space. Equation (2.33) indicates an electric field with polarisation along the x-direction.

Because the speed of electromagnetic waves in a medium is governed by its refractive index, n, it is assumed that the two circularly polarised fields, $\boldsymbol{E}_\pm$, propagate with indices of refraction, $n_\pm$. The wavenumber for the two fields, $k_\pm$ is given by [90] :

$$k_\pm = \frac{2\pi}{\lambda_m} = \frac{2\pi}{\lambda/n_\pm} = \frac{2\pi}{\lambda}n_\pm, \tag{2.34}$$

where λ_m is the wavelength of the waves in the medium and λ is the wavelength of the light measured in a vacuum.

Any attenuation of the waves in the medium is taken into account by including the attenuation constants, $\beta_\pm$, and assuming that there is equal attenuation for the two polarisations, that is, $\beta_+ = \beta_- = \beta$. Hence, the emergent field through the medium of length, L, is:

$$\boldsymbol{E}_\pm(L,t) = 2E_0\ exp(-\beta L)(\hat{\boldsymbol{x}}\cos\Delta\theta - \hat{\boldsymbol{y}}\sin\Delta\theta)\ exp\ i(\frac{2\pi}{\lambda}\frac{n_+ + n_-}{2}L - \omega t). \tag{2.35}$$

Equation (2.35) shows that the plane of the linearly polarised light has been rotated by an angle, $\Delta\theta$, given by:

$$\Delta\theta = \frac{2\pi}{\lambda}(\frac{n_+ - n_-}{2})L. \tag{2.36}$$

Equation (2.36) indicates that the angle the plane of polarisation has rotated by is dependent on the difference between the two refractive indices.

To understand how the macroscopic quantity, n, is related to the microscopic behaviour of the medium, it is first assumed that the medium as a whole develops a

polarisation, $\boldsymbol{P}$, in response to the electric field, $\boldsymbol{E}$, of the incident light, given by:

$$\boldsymbol{P} = \varepsilon_0 \chi \boldsymbol{E}, \tag{2.37}$$

where ε_0 is the permittivity of free space and χ is the electric susceptibility. χ is a dimensionless, complex and frequency dependent quantity which characterises how the medium responds to light.

Now, for the medium of atoms with number density, n_{atoms}, a very simple atomic model in which the atomic ground state is non-degenerate and the excited state has three magnetic sublevels which split in the presence of a small static magnetic field, $\boldsymbol{B}_0 = B_0\hat{\boldsymbol{z}}$, as illustrated in Figure 2.8, is assumed.

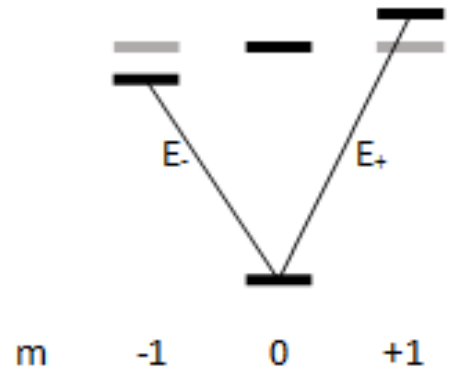

Figure 2.8: A simple atomic model used to compute Faraday rotation in an alkali vapour (not to scale). The ground state is non-degenerate and the excited level is split into three magnetic sublevels by a small static magnetic field applied in the z-direction, $\boldsymbol{B}_0 = B_0\hat{\boldsymbol{z}}$. Grey bars indicate the unperturbed energy levels.

Because of conservation of angular momentum, it is known that each circularly polarised field in equation (2.32) can only induce transitions in the medium with $\Delta m = \pm 1$, therefore, each circular polarisation will separately interact with its own two-level system, and consequently travel through the medium with its own index of refraction and attenuation constant. These values can be obtained from the susceptibility of a generic two-level atomic system, which is given as a function of

optical frequency by [91]:

$$\chi(\nu) = \frac{n_{atoms}\lambda^3}{16\pi^3\tau}\frac{1}{(\nu_0-\nu)-i\frac{\Delta\nu}{2}}, \tag{2.38}$$

where $\lambda = c/\nu$, ν_0 is the centre frequency of the transition, $\Delta\nu = (2\pi\tau_{spon})^{-1}$ is the FWHM (in non-angular frequency), and τ_{spon} is the spontaneous decay rate of the upper state lifetime.

It is seen that the refractive index as a function of frequency, $n(\nu)$, is found to be [91]:

$$n(\nu) - 1 = \frac{n_{atoms}\lambda^3}{32\pi^3\tau_{spon}}\frac{\nu_0-\nu}{(\nu-\nu_0)^2+(\frac{\Delta\nu}{2})^2}, \tag{2.39}$$

which shows a dispersive dependence on frequency.
Consequently, it is found that the rotation angle, $\Delta\theta$, is:

$$\Delta\theta(\nu) = \frac{n_{atoms}\lambda^2 L}{32\pi^2\tau_{spon}}\left[\frac{\nu_{0+}-\nu}{(\nu_{0+}-\nu)^2+(\frac{\Delta\nu}{2})^2} - \frac{\nu_{0-}-\nu}{(\nu_{0-}-\nu)^2+(\frac{\Delta\nu}{2})^2}\right]. \tag{2.40}$$

where $\nu_{0\pm}$ are the shifted resonance frequencies due to the magnetic field.

The Faraday readout of spin, F_z, from the effective Hamiltonian (equation (2.27)) is a quantum non-demolition measurement (QND) [92, 93]. QND requires the fulfilment of the sufficient condition: the measured quantity, F_z, must be an integral of the motion for the coupled probe and atomic spins, that is, it must not only return to its initial value (in the Heisenberg picture) at the end of the interaction, but it must remain constant throughout the interaction [94]. This condition is equivalent to the relation:

$$i\hbar\frac{\partial\hat{F}_z}{\partial t} + [\hat{F}_z, \hat{H}_{int}] = 0. \tag{2.41}$$

As $\hat{F}_z$ is constant during the interaction with the probe beam, it has no explicit time dependence, so:

$$\frac{\partial\hat{F}_z}{\partial t} = 0. \tag{2.42}$$

Therefore, it follows that for the measurement to be QND, F_z must commute with

the effective interaction Hamiltonian, $\hat{H}_{int}$:

$$[\hat{F}_z, \hat{H}_{int}] = 0. \tag{2.43}$$

and since $\hat{H}_{int} \propto S_3\hat{F}_z$, this condition is fulfilled for the Faraday effect. Thus, information about the atomic spin is able to be obtained via the probe beam without interfering with it. The atomic spin is unperturbed by the probe light and subsequent interrogations will yield the same result [94].

Now, the term which contains the tensor polarisability, α_2, produces higher order couplings between the light and atoms, represented by the constant, D. This type of interaction is a non-QND interaction, indicating a perturbation of the probe that alters the state of the atoms. It arises due to the quadratic dependence of m_F on the energy.

The relative magnitude of the last two terms in equation (2.27) is dependent on the strength of the coupling between the probe beam and atomic spins. The dependence of the signal on the detuning defines the spectral line. To probe in the limit where the tensor term is negligible means that the probe beam should be at a low intensity or with its detuning far greater than the frequency separation between the hyperfine components of the excited levels. Conversely, higher intensities and smaller detunings will magnify the tensor interaction.

2.6 Interaction with rf Magnetic Fields

In section 2.5.1, it was stated that optical pumping with circularly polarised light is used to orient atoms, producing a longitudinal macroscopic polarisation parallel to the magnetic field, $\boldsymbol{B}_0$, which is assumed to lie along the x-axis, that is, $\boldsymbol{B}_0 = B_0\hat{\boldsymbol{x}}$.

Addition of a weak oscillating rf magnetic field, $\boldsymbol{B}_{rf}$, transverse to $\boldsymbol{B}_0$ in the y-direction will tilt the magnetisation vector away from the x-axis, causing it to precess around $\boldsymbol{B}_0$, if its oscillation frequency is approximately equal to the Larmor frequency, ω_L, defined as [95]:

$$\omega_L = \gamma B_0. \tag{2.44}$$

where γ is the atomic gyromagnetic ratio.

Assuming that $\boldsymbol{B}_{rf} = B_{rf}cos(\omega_1 t)\hat{\boldsymbol{y}}$ is applied in the y-directon, the evolution of $\boldsymbol{M}$ in the presence of $\boldsymbol{B}_{rf}$ and $\boldsymbol{B}_0$ in the laboratory frame is:

$$\frac{d\boldsymbol{M}}{dt} = \gamma_0 \boldsymbol{M} \times (B_0\hat{\boldsymbol{x}} + B_{rf}cos(\omega_1 t)\hat{\boldsymbol{y}}). \tag{2.45}$$

When solving equation (2.45), it is convenient to eliminate the time dependence by using the rotating coordinate system in which the y- and z-axes, denoted by y' and z' rotate around the x-axis at angular frequency, $\boldsymbol{\omega}_1 = \omega_1\hat{\boldsymbol{x}}$. $\boldsymbol{\omega}_1$ is a vector whose magnitude gives the angular frequency of rotation of the rotating system, which is the same as the angular frequency of $\boldsymbol{B}_{rf}$, and whose direction is the axis about which the system rotates, that is, the x-axis. Ignoring for the moment $\boldsymbol{B}_{rf}$, the rate of change of $\boldsymbol{M}$ as viewed from the rotating frame is related to the rate of change of $\boldsymbol{M}$ as viewed in the laboratory frame by the expression:

$$(\frac{d\boldsymbol{M}}{dt})_{ROT} = (\frac{d\boldsymbol{M}}{dt})_{LAB} - (\boldsymbol{\omega}_1 \times \boldsymbol{M}), \tag{2.46}$$

$$(\frac{d\boldsymbol{M}}{dt})_{ROT} = \gamma \boldsymbol{M} \times (\boldsymbol{B}_0 + \frac{\boldsymbol{\omega}_1}{\gamma}). \tag{2.47}$$

Equation (2.47) indicates that as far as the rate of change of $\boldsymbol{M}$ is concerned, transforming to the rotating frame at $\boldsymbol{\omega}_1$ is the same as adding a fictitious field, $\frac{\boldsymbol{\omega}_1}{\gamma}$ so that the total effective field is given by [96]:

$$\boldsymbol{B}_{eff} = \boldsymbol{B}_0 + \frac{\boldsymbol{\omega}_1}{\gamma}. \tag{2.48}$$

It follows that around resonance, $\boldsymbol{M}$ is constant in the rotating frame because $\boldsymbol{B}_{eff}$ is 0, which can only happen if $\boldsymbol{\omega}_1 = -\gamma\boldsymbol{B}_0$ [96]. Thus, the effective field acts in the x-direction and is given by:

$$\boldsymbol{B}_{eff} = (B_0 - \frac{\omega_1}{\gamma}).\hat{\boldsymbol{x}} \tag{2.49}$$

Now, $\boldsymbol{B}_{rf} = B_{rf}cos(\omega_1 t)\hat{\boldsymbol{y}}$ can be thought of as a superposition of two counter-

propagating rotational magnetic fields at frequencies $\pm\omega_1$ and amplitudes $\frac{B_{rf}}{2}$. One component oscillates at a negative frequency with respect to the atomic spins so has no effect on the spins. Thus, only the co-rotating component is of interest and in the rotating reference frame, it appears stationary.

Consequently, the total resultant field in the rotating frame is:

$$\boldsymbol{B}_{res} = (B_0 - \frac{\omega_1}{\gamma})\hat{\boldsymbol{x}} + \frac{B_{rf}}{2}\hat{\boldsymbol{y}'}, \tag{2.50}$$

Therefore, the evolution of $\boldsymbol{M}$ in the presence of $\boldsymbol{B}_{res}$ is:

$$(\frac{d\boldsymbol{M}}{dt})_{ROT} = \gamma\boldsymbol{M} \times \boldsymbol{B}_{res} = \gamma\boldsymbol{M} \times (\boldsymbol{B}_0 - \frac{\boldsymbol{\omega}_1}{\gamma} + \frac{\boldsymbol{B}_{rf}}{2}). \tag{2.51}$$

Physically, equation (2.51) states that $\boldsymbol{M}$ acts as though it experiences a static resultant field, $\boldsymbol{B}_{res}$, which causes it to precess in a cone of fixed angle about the direction of $\boldsymbol{B}_{res}$ at angular frequency, $\gamma\boldsymbol{B}_{res}$ (Figure 2.9).

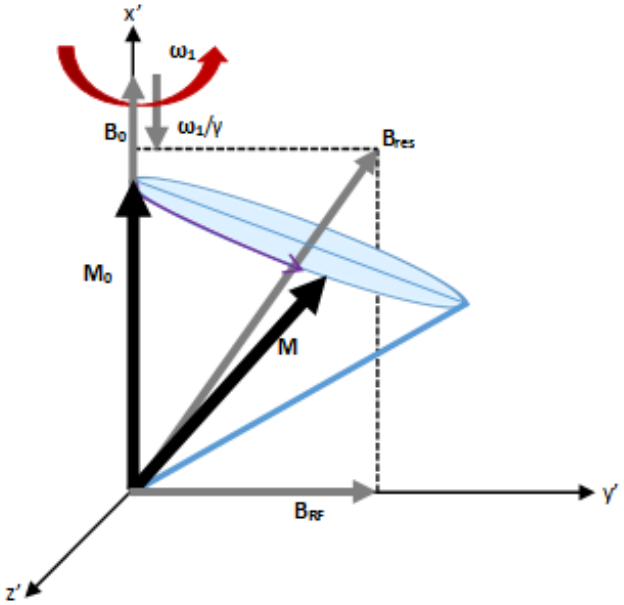

Figure 2.9: Diagram illustrating the evolution of $\boldsymbol{M}$ in the presence of a static magnetic field ($\boldsymbol{B}_0$) and a weak oscillating rf magnetic field ($\boldsymbol{B}_{rf}$) in the rotating coordinate system.

Taking relaxation into account, equation (2.51) becomes:

$$(\frac{d\boldsymbol{M}}{dt})_{ROT} = \gamma \boldsymbol{M} \times (\boldsymbol{B}_0 - \frac{\boldsymbol{\omega}_1}{\gamma} + \frac{\boldsymbol{B}_{rf}}{2}) - \frac{M_{y'}\hat{\boldsymbol{y}'} + M_{z'}\hat{\boldsymbol{z}'}}{T_2} - \frac{(M_x - M_0)\hat{\boldsymbol{x}}}{T_1}. \quad (2.52)$$

where T_1 and T_2 are the lifetimes of the longitudinal and transverse magnetisations, respectively, and $\boldsymbol{M}_0 = M_0\hat{\boldsymbol{x}}$ is the longitudinal magnetisation in the absence of rf excitation. The steady state solutions for equation (2.52) can be be found by setting $(\frac{d\boldsymbol{M}}{dt})_{ROT} = 0$ and solving for the three magnetisation components:

$$M_{y'} = M_0 \frac{\Omega T_2}{1 + (\Delta\omega T_2)^2 + \Omega^2 T_1 T_2}, \quad (2.53)$$

$$M_{z'} = -M_0 \frac{\Delta\omega T_2^2}{1 + (\Delta\omega T_2)^2 + \Omega^2 T_1 T_2}, \quad (2.54)$$

$$M_{x'} = M_0 \frac{1 + (\Delta\omega T_2)^2}{1 + (\Delta\omega T_2)^2 + \Omega^2 T_1 T_2}. \quad (2.55)$$

where $\Delta\omega = \omega_1 - \omega_0$ and $\Omega = \gamma\frac{B_{rf}}{2}$.

The component of the magnetisation that is of interest is along the z-axis in the laboratory frame, that is, M_z. So, transferring from the rotating to laboratory frame gives:

$$M_z = M'_z \cos(\omega_1 t) - M'_y \sin(\omega_1 t), \quad (2.56)$$

$$M_z = M_0 \Omega \frac{T_2 \cos(\omega_1 t) + \Delta T_2^2 \sin(\omega_1 t)}{1 + (\Delta\omega T_2)^2 + \Omega^2 T_1 T_2}. \quad (2.57)$$

The measured signal has a Lorentzian absorptive component that is in-phase with the rf oscillating field and a dispersive out of phase component (Figure 2.10).

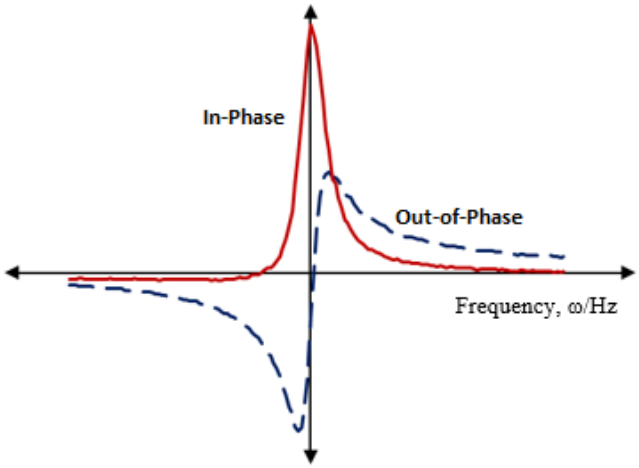

Figure 2.10: Diagram illustrating the absorptive component which is in phase with the rf oscillating field and the dispersive component which is out of phase with the rf oscillating field.

Chapter 3

Theory of Atomic Magnetometers

3.1 Introduction

The purpose of this chapter is to provide the general background theory behind atomic magnetometers. An atomic magnetometer is a sensor which is used to measure a magnetic field through its interaction with the atomic sample. The fundamental components of an atomic magnetometer are an alkali metal vapour, a laser beam to polarise the atoms (the pump beam) and another laser beam to probe the evolution of the polarised atoms (the probe beam) in a magnetic field. The general schematic of the atomic magnetometer is shown in Figure 3.1. Its principal of operation will be described through the concepts presented in chapter 2. In addition, the two classes of magnetometers: the rf and dc magnetometers will be discussed. While the operating principle is the same for both classes, there are some differences in the measurement procedures. The principle difference is attributed to the way in which the two magnetometers measure the transverse component of the macroscopic spin polarisation vector. Finally, the factors which affect the sensitivity of the magnetometer will be examined.

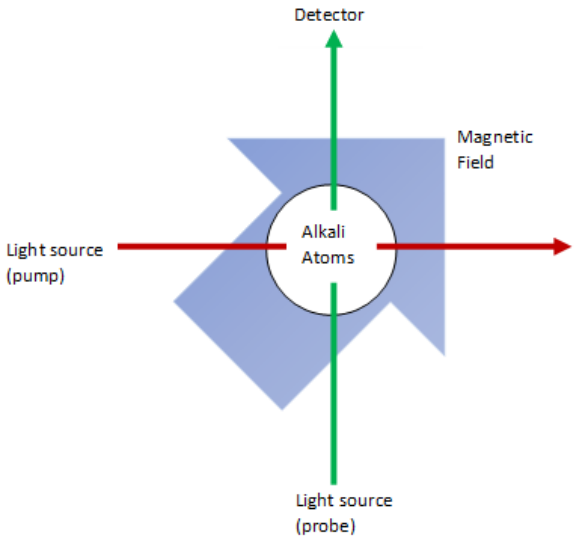

Figure 3.1: General schematic of an atomic magnetometer. The pump beam polarises the atoms, the atomic polarisation orthogonal to the magnetic field precesses about the field and the resultant state of the atoms' polarisation is detected by measuring the polarisation rotation of the probe beam.

3.2 Principle of Operation

Measurement of a magnetic field with an atomic magnetometer consists of three phases which occur simultaneously:

1.) **Preparation of the atomic spin by optical pumping**. In a configuration relevant to the experiments described in this project, circularly polarised light, referred to as the pump beam, is used to create the collective atomic spin. This is achieved by the process of optical pumping [97] as described in chapter 2, section 2.5.1. Other configurations may employ linear polarisation and other types of geometries for optical pumping.

2.) **Interaction of the atomic spin with the magnetic field**. In the presence of a magnetic field orthogonal to the atomic polarisation, the atomic spins' precess about the field axis at the Larmor frequency, ω_L.

3.) **Detection of the magnetic field strength**. The precessing magnetisation is detected by utilising the Faraday effect to measure the polarisation rotation of the probe beam, which is linearly polarised. Choosing the polarisation method

offers certain inherent advantages, such as a reduced sensitivity to laser intensity fluctuations, and the ability to detect very small polarisation-rotation angles [3].

3.2.1 Classes of Atomic Magnetometers

Atomic magnetometers can be used for rf and dc magnetic field measurement. While the operating principle of each type is the same, there are some differences in measurement procedures.

Generally, the atomic magnetometer monitors the ground state coherences. These are equivalent to spin components orthogonal to the static magnetic field. The static magnetic field defines the quantisation axis. These spin components precess about the magnetic field at ω_L. There are two ways to produce the coherences:

- A weak rf magnetic field oscillating at ω_L, perpendicular to the direction of both the static magnetic field and collective atomic spin, creates a polarised spin component transverse to the static magnetic field, which precesses about that field at ω_L. This is the principle behind the rf magnetometer, which measures the field through observation of the amplitude of the transverse polarisation component, that is, the amplitude of the coherences.

- Modulation of the pump beam at ω_L, applied in a direction perpendicular to the static magnetic field produces a collective atomic spin component which precesses about the field. This is the concept underlying the dc magnetometer which measures the field through observation of the frequency of the coherence oscillation.

3.2.1.1 The rf Magnetometer

Savukov et al. [98] in 2005 introduced a tunable rf atomic magnetometer for detection of rf magnetic fields. They showed that that by tuning the Zeeman spin resonance frequency of the atoms to the rf, it was possible to achieve high sensitivity to the rf field. The magnetometer operated at a resonant frequency of 99 kHz with a bandwidth of 400 Hz and had a demonstrated sensitivity of 2 fT/$\sqrt{\text{Hz}}$, along with a calculated fundamental sensitivity of 0.01 fT/$\sqrt{\text{Hz}}$ [98]. In 2007, the rf magnetometer was first used for NMR where it was shown to be intrinsically more

sensitive than an inductive pickup coil of comparable size for frequencies below 50 MHz [36]. In 2006, Lee et al. [99] used the rf magnetometer for detection of nuclear quadrupole resonance (NQR) where a sensitivity of 0.24 fT/$\sqrt{\text{Hz}}$ at a resonant frequency of 423 kHz was demonstrated. In 2012 Chalupczak et al. [100] demonstrated a room temperature rf magnetometer with a sensitivity of 1.16 fT/$\sqrt{\text{Hz}}$ in a range of $10-500$ kHz. A high density ^{87}Rb magnetometer with sensitivity 5 fT/$\sqrt{\text{Hz}}$ and fundamental sensitivity of 3 fT/$\sqrt{\text{Hz}}$ was demonstrated by Savukov et al. [101] in 2014.

The standard setup consists of the cell placed in a static magnetic field, which is applied in a direction, arbitrarily taken to be the x-direction. The static magnetic field is used to tune the Zeeman sublevels in resonance with a measured rf magnetic field.

The circularly polarised pump beam, applied in the same direction as the static magnetic field, pumps the alkali atoms so that they are polarised along x. As discussed in chapter 2, section 2.5.1, the pump beam creates a population imbalance in the ground state by pumping the atoms into the stretched state, thereby generating a longitudinal magnetisation component along the static magnetic field direction.

The weak, oscillating rf field, applied orthogonally (y-direction) to the static magnetic field with a frequency that coincides with the energy splitting of adjacent m_F sublevels, creates ground state coherences between neighbouring sublevels. This is equivalent to a transverse spin component that precesses about the magnetic field at ω_L, as described in chapter 2, section 2.6. The amplitude of the transverse polarisation is proportional to the strength of the rf field.

As the transverse spin component precesses, it will interact with the linearly polarised probe beam, which propagates in a direction orthogonal to the static and rf magnetic fields (z-direction). The precessing spin component will result in an oscillation of the plane of polarisation of the probe beam, which is detected using the Faraday effect.

The rf magnetometer offers many advantages. It is able to operate in an unshielded or partially shielded environment [36]. Adjusting the static magnetic field

allows the rf magnetometer to be tuned to detect rf fields anywhere up to many MHz, with minimal variation in the resonance response amplitude [2]. Consequently, it can be used to quickly scan over a broad frequency range for the appropriate resonance signal [2]. High frequency operation reduces magnetic noise produced by Johnson electrical currents in neighbouring conductors, and it is relatively insensitive to vibrations and laser noise at these frequencies [36, 102].

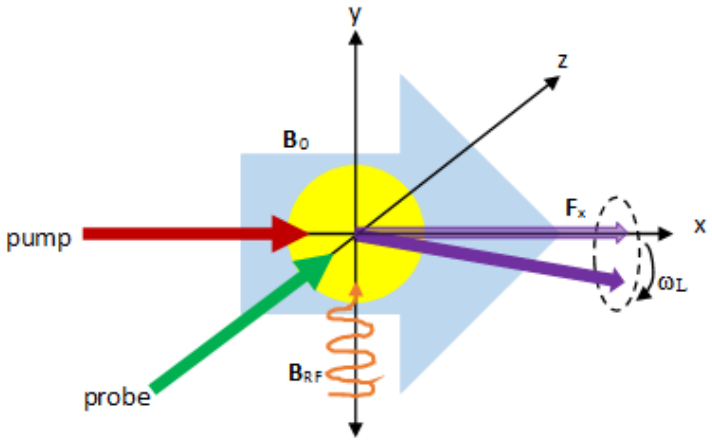

Figure 3.2: Principle of the rf magnetometer. Circularly polarised light, propagating in the x-direction, is used to pump the atoms, producing a macroscopic polarisation, $\boldsymbol{F}_x$, parallel to the static magnetic field ($\boldsymbol{B}_0$). A weak oscillating rf magnetic field, $\boldsymbol{B}_{rf}$, orthogonal to $\boldsymbol{B}_0$ induces a transverse spin component which precesses about $\boldsymbol{B}_0$ at the Larmor frequency, ω_L. The precessing component is detected as a rotation of the plane of polarisation of the linearly polarised probe beam, propogating orthogonally to $\boldsymbol{B}_0$ and $\boldsymbol{B}_{rf}$.

3.2.1.2 The dc Magnetometer

William E. Bell and Arnold L. Bloom in 1961 noticed that an alternative to using rf excitation to produce the ground state coherences was to modulate the optical pumping rate with a frequency resonant with the Larmor precession of atomic spins, in what is referred to as synchronous optical pumping [97]. Since then, there have been numerous research into the application of synchronous optical pumping in the context of atomic magnetometry.

In 1995, Cheron et al. [103–105] demonstrated the realisation of a ^{4}He magnetometer based on optical pumping with a frequency modulated (FM) semiconductor laser diode, with followup work done in 1996 and 2001. Budker et al.

[106] in 2002, used FM modulated light in an ^{87}Rb magnetometer, but in contrast to the work carried out previously [103–105], where the resonant signal was detected by monitoring the transmitted light through the cell, Budker measured the optical rotation of the beam. In 2006, Gawlik et al. [107] focused on using amplitude modulated (AM) light for optical pumping in atomic magnetometry as an alternative to FM light modulation. Polarisation modulation (SM) was first explored by Gilles et al. [108] in 1991, then by Klepel et al. [109] in 1992 and its application to atomic magnetometers was demonstrated by Kish and Romalis [110] in 2010, Huang et al. [111] in 2012 and Fescenko et al. [112] in 2013. Other research into synchronous optical pumping applied to atomic magnetometry can be found in [113–117].

In the dc magnetometer, the magnetic field to be detected, along the x-direction, is perpendicular to the pump beam, which propagates along y. The circularly polarised pump beam resonant with an atomic transition pumps atoms, producing a macroscopic polarisation in the same direction as the pump beam.

Because the macroscopic spin polarisation component is transverse to the static magnetic field, it will begin to precess about the magnetic field at ω_L, immediately after optical pumping. To ensure that the the polarisation component precesses with the same phase each time atoms are optically pumped, the pump beam is modulated at ω_L [3]. Modulation of the pump beam can either be achieved through AM, FM or SM of the beam. These techniques enable the precession of the collective atomic spin and the modulated pumping rate to be synchronised [118]. If modulation is at any other frequency, the precessing polarisation at a particular time will have a different phase to the polarisation produced at an earlier time, hence, coherence of the atomic polarisation will be lost.

Now, if the pump rate is modulated at ω_L, atoms will only ever be pumped after they have completed one complete precessional cycle and are again aligned with the pumping direction [2]. Hence, atoms will always precess in phase with each other. This is the optically driven spin precession first demonstrated by Bell and Bloom in 1961 [97]. Consequently, this type of configuration is known as a Bell-Bloom configuration.

In AM modulation, the pump laser is turned on and pumping occurs when the macroscopic atomic spin polarisation is in the forward direction with respect to the wave vector, $\boldsymbol{k}$, of the propagating pump beam but turned off when the spin polarisation is in the backward direction [15]. Similarly, in FM modulation, the pump laser is on resonance only when the precessing atomic spins are in the forward direction with respect to $\boldsymbol{k}$ [15]. However, in SM modulation, pumping occurs in both directions, in the forward direction by σ^+ light and in the backward direction by σ^- light. Because of this property, SM-pumping is also referred to as "push-pull pumping" [15].

Like the rf magnetometer, the precessing component is detected as a rotation of the plane of polarisation of the linearly polarised probe beam by utilising the Faraday effect.

The advantages of the dc magnetometer include a simpler design than the rf magnetometer, and when used as part of an array of sensors, there is no cross talk among the magnetometers. Cross talk is sometimes a problem among the rf coils of rf array-based magnetometers.

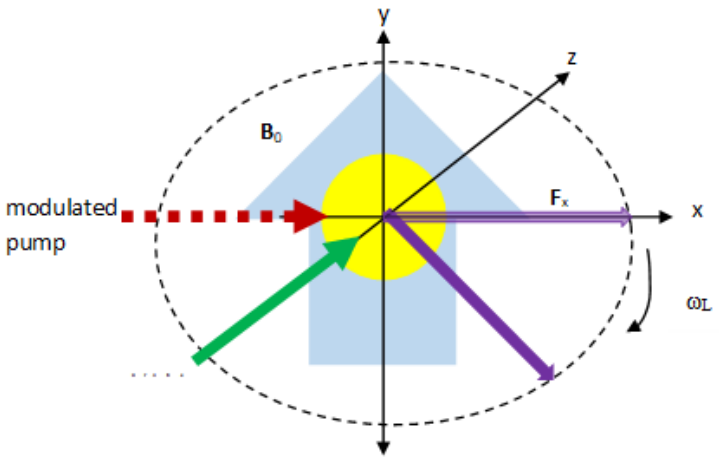

Figure 3.3: Principle of the dc magnetometer. The pump and probe beams are orthogonal to the static magnetic field, $\boldsymbol{B}_0$ so that immediately after pumping, the polarisation begins to precess about the magnetic field. The pump beam is modulated at the Larmor frequency, ω_L, to ensure that the precessing polarisation is always in phase with the polarisation produced at an earlier time. The precessing component is detected as a rotation of the plane of polarisation of the linearly polarised probe beam.

3.3 Sensitivity of the Magnetometer

The sensitivity of a magnetometer can be defined in two ways: it is either the smallest change in the magnetic field level that the sensor is able to distinguish or it is the size of the smallest magnetic field it can detect [2].

The atomic magnetometer is a quantum device and like all quantum devices, it has an intrinsic limit on its sensitivity imposed by quantum mechanics. Therefore, the ability of the atomic magnetometer to make a precise measurement of the magnetic field is fundamentally limited by three sources of noise, excluding electronic noise. These are the atomic projection noise which is the fluctuation of atomic spins, the photonic shot noise caused by fluctuations in the number of photons in the polarimeter used for detection and quantum back-action arising from perturbation of the atomic spins by the probe beam.

3.3.1 Atomic Projection Noise

The atomic projection noise arises from the fact that if an atom is polarised in a particular direction, there is a certain amount of uncertainty in a measurement in an orthogonal direction.

For a fully polarised spin state along the x-axis, where $< F_x >= F$, there will be quantum fluctuations in the measurement of $< F_z >$ and $< F_y >$ because of coherence precession which are picked up by the probe beam along an orthogonal direction such as the z-direction. The standard deviation due to these fluctuations of many measurements on many different atoms is given by [3]:

$$\sigma(F_z) = \sqrt{\frac{F}{2}}. \tag{3.1}$$

The general formula that takes into account uncertainty in the atomic spin component due to quantum fluctuations in the measurement of alkali atoms is described by [46]:

$$\delta B_{apn} = \frac{1}{\gamma}\frac{1}{\sqrt{NT_2\tau}}. \tag{3.2}$$

where γ is the gyromagnetic ratio, T_2 is the lifetime of the transverse magnetisation,

N is the number of interrogated atoms and τ is the measurement time. Equation (3.2) is derived from the observation that a measurement with a single atom with a duration τ produces an uncertainty in the Larmor precession angle on the order of one radian [46] [49]. With N atoms, this is improved by $\sqrt{N}$, and repeating the measurement multiple times gains another factor of $\sqrt{\frac{\tau}{T_2}}$ [46]. According to equation (3.2), the sensitivity is dependent on N, T_2 and τ. With this information, a number of potential strategies for improving sensitivity can be realised [15]. Such strategies will be discussed in section 3.3.4.

3.3.2 Photonic Shot Noise

The second factor which limits the fundamental sensitivity is related to the quantised nature of photons. Photonic shot noise arises as a consequence of the quantised nature of the probe beam photons, in which each individual photon event detected, is independent of all other events, thus the number of photons detected in equal time intervals vary randomly. In other words, their flux per unit time fluctuates over time around its mean value, $\overline{N_{flux}}$, with amplitude, $\sqrt{\overline{N_{flux}}}$. Consequently, the intensity and polarisation of light can be determined with a finite precision given by $\frac{1}{\sqrt{\overline{N_{pr}}\tau}}$ where N_{pr} is the number of probe photons. This sets a limit on the precision of spin-state determination and hence the sensitivity of magnetic-field measurements. One way to mitigate this problem is to operate with higher probe light intensities where the SNR increases, thereby increasing the sensitivity. However, using higher probe beam intensities can result in optical pumping by the probe. Hence, the probe beam should be detuned from the optical transition in order to reduce this effect.

In the balanced polarimetry technique which is used for detection in the experiments described in this thesis, there will be fluctuations in the number of photons collected in each photodiode. If N_{pr} photons pass through the atomic ensemble with negligible absorption, then each photodiode will record on average $N_{pr} = \frac{N_{pr}}{2}$, with shot noise uncertainty:

$$\sigma = \sqrt{\frac{N_{pr}}{2}}. \tag{3.3}$$

This leads to an uncertainty in the rotation angle of the plane of polarisation of the probe beam:

$$\sigma(\phi) = \frac{1}{2\sqrt{N_{pr}}}. \tag{3.4}$$

From the fluctuations in the rotation angle, one finds that the uncertainty in the measurement of the $< F_z >$ component of the collective atomic spin due to photonic shot noise is described by the following equation:

$$\delta Bshot = \frac{1}{g_F \mu_B \tau} \frac{1}{N\sqrt{N_{pr}}} \frac{\Delta}{\Gamma_{nat}} \frac{A}{\lambda^2}. \tag{3.5}$$

where g_F is the Landé g-factor, μ_B is the Bohr magneton, τ is the measurement time, N is the number of interrogated atoms, N_{pr} is the number of photons reaching the detector, Γ_{nat} is the natural transition width, A is the area of the cross section of the atomic medium, λ is the wavelength of the probe beam and Δ is the detuning of the probe beam from the resonant transition.

3.3.3 Quantum Back-action

The final contribution which limits the magnetic field sensitivity arises from the quantum back-action of the probe light onto the atoms. It arises from the AC Stark shift, mentioned in chapter 2 section 2.5.2.1, in which the electric field of the probe light modifies the Zeeman sublevel energies [15].

Even though the probe beam is linearly polarised, there will be quantum fluctuations in the degree of circular polarisation which produces a fictitious magnetic field along the direction of light propagation. As a result, the precessional frequency of the atomic spins change, mimicking the change of the static magnetic field [15]. Thereby, the fundamental fluctuations in light intensity may contribute to the uncertainty in the spin-state determination [15].

Other instances when the quantum back-action noise is pronounced are when the pump beam is off-resonance, and the magnetic field to be detected is not orthogonal to both laser beams. When the laser beams are orthogonal to the magnetic field to be measured, then any light shift fluctuations add quadratically to the field and only contributes in second order to the absolute value of the magnetic field to be

measured. In the setup described in this thesis, quantum back-action is a problem because the transverse spin polarisation component is in the same direction as the propagating probe beam.

3.3.3.1 Electronic Noise

Though not one of the fundamental noise sources, electronic noise inherent in all electrical devices is present in all measurements, therefore it warrants discussion. The sources of electronic noise originate from the electronic equipment used for locking the pump and probe beams, the electrical components of the photodiode detector used for converting the optical signal into an electrical signal, and the electrical components of the lock-in amplifier used to demodulate the electrical signal. The basic types of noise are:

- **Johnson noise**: arises from fluctuations in voltage across a resistor and exists in all electrical conductors. It was observed by J.B Johnson in 1927 and takes the form [119, 120]:

$$\Delta V = \sqrt{4k_B T R \Delta f}. \tag{3.6}$$

  where k_B is the Boltzmaan constant, T is the temperature in Kelvin, R is the resistance of the resistor and Δf is the bandwidth in Hz. The Johnson noise for a resistor at room temperature is $0.13\sqrt{R}$ nV$/\sqrt{\text{Hz}}$. The magnitude of this type of noise is flat as a function of frequency and is referred to as "white noise".

- **1/f** noise: also known as "pink noise" arises from fluctuations in the value of the resistance itself, due probably to motion of impurities [121]. This type of noise is the same for each decade of frequency.

- **Shot noise**: arises from the quantisation of electric charge.

3.3.4 Improving Sensitivity

The sensitivity, ΔB, depends on the SNR, as well as the linewidth of the resonance signal. The lifetime of the transverse magnetisation, that is, the coherence

lifetime, T_2, determines the width of the resonance in the frequency domain [2]:

$$\Delta B = \frac{\Delta\omega_L}{\gamma} = \frac{1}{\gamma T_2}. \tag{3.7}$$

A narrow linewidth means that the transverse spin relaxation rate, γ_{rel}, is small (γ_{rel} is the inverse of T_2). A long polarisation lifetime is essential for obtaining a sensitive magnetometer. There are several ways to improve sensitivity.

One such way is by pumping atoms into the stretched state, thereby having a high degree of orientation. A second improvement is to increase the number of alkali atoms in the cell. This can be achieved by using a larger cell or by increasing the alkali vapour density by increasing the temperature of the cell. It was stated in chapter 2, section 2 that Cs was used because it has a relatively high vapour pressure at room temperature compared to Rb and K. This is advantageous because a sensitive magnetometer which can be used in real world conditions is feasible to produce. In addition, pump and probe intensities need not be too high as the atomic vapour at room temperature is not optically thick. High intensity pump and probe beams will lead to power broadening of the resonant transition. A third improvement is to detune the resonant frequency of the probe beam from that of the pump beam so that it does not destroy the macroscopic polarisation created by the pump beam.

3.3.5 Relaxation Mechanisms

The optimum magnetometer sensitivity depends on the lifetime of the macroscopic spin polarisation produced by optical pumping. The lifetime of the spin polarisation depends on the lifetimes of the longitudinal (T_1) and transverse (T_2) components. In all media, there are relaxation mechanisms which oppose optical pumping and try to re-establish thermal population distributions. Here, the relaxation mechanisms pertinent to the experiments described in this thesis which were performed at room temperature, are discussed.

3.3.5.1 Spin-Exchange Collisions (SEC)

SEC are the dominant type of interaction between atoms in an alkali metal vapour at room temperature. When two atoms with electrons having opposite spins collide, the total atomic spin can be conserved but the individual electron spins are reversed. Symbolically, this is represented as:

$$A(\uparrow) + B(\downarrow) \rightarrow A(\downarrow) + B(\uparrow). \tag{3.8}$$

where $(\uparrow)$ refers to spin-up and $(\downarrow)$ refers to spin-down.

These collisions happen so quickly that only electron spins are affected; nuclear spins are largely unaffected.

The physical basis of this is the electrostatic "exchange potentials", which are different for symmetric and anti-symmetric combinations of the atomic orbitals. The two atom complex is described by mixtures of the two combinations, and under the effect of the exchange potentials, one component advances in phase over the other, leading to an interchange in the electron spin components [122].

Even though the total atomic spin is conserved, such collisions can result in a loss of spin coherence [46]. The direction of magnetic precession, determined by the relative orientation of the electron spin with respect to the total atomic spin, is opposite for the two hyperfine states. So, atoms in the two ground state hyperfine levels precess with approximately the same frequency but in opposite directions [2, 46]. Thus, in the presence of a magnetic field, SEC can randomly transfer atoms between the two hyperfine ground states, causing a redistribution of the atoms among the m_F sublevels [2]. Atoms exchanging ground states means that the populations of the two hyperfine levels no longer precess in phase with each other because the atoms' angular momenta are all at random angles with respect to each other [2, 46]. This leads to destruction of the transverse polarisation component.

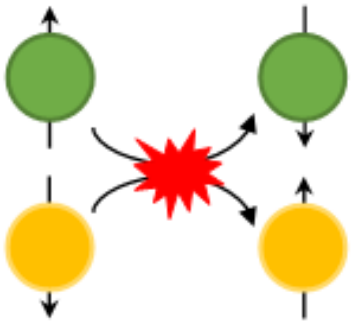

Figure 3.4: Diagram illustrating the concept of a spin exchange collision (SEC). When two atoms with electrons having opposite spins collide, the total atomic is conserved but the individual electron spins are reversed.

3.3.5.2 Spin-destruction Collisions

The second most important mechanism for spin relaxation is spin-destruction collisions in which the total atomic spin of the atomic ensemble is not preserved. In collisions of this type which involve only alkali atoms, spin angular momentum is transferred to the orbital angular momentum of the colliding pair. The transfer of angular momentum is thought to be due to a magnetic dipole spin-spin interaction of the form:

$$H_{SS} = \frac{2}{3}\lambda \boldsymbol{S}_{ab}.(3\hat{\boldsymbol{R}}\hat{\boldsymbol{R}} - 1).\boldsymbol{S}_{ab}. \tag{3.9}$$

where $\boldsymbol{S}_{ab} = \boldsymbol{S}_a + \boldsymbol{S}_b$ is the total electronic spin of the colliding atoms, $\hat{\boldsymbol{R}}$ is the direction of the internuclear axis of the colliding pair and λ is the interaction constant [123]. The spin-destruction rates are about 1% of the spin-exchange rates [123]. Like equation (3.8), spin-destruction collisions can be represented symbolically as:

$$A(\uparrow) + B(\downarrow) \rightarrow A(\downarrow) + B(\downarrow). \tag{3.10}$$

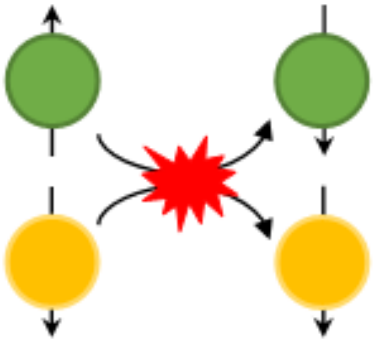

Figure 3.5: Diagram illustrating a spin-destruction collision. The total atomic spin of the atomic ensemble is not conserved. In collisions of this type, there is a transfer of spin angular momentum to the orbital angular momentum of the colliding pair.

3.3.5.3 Wall Collisions

When an atom collides with the bare glass surface of the cell, it becomes stuck to the surface for a finite amount of time. During this period, the local electric and magnetic fields of the glass ions and molecules rapidly depolarise the atomic spin. This is very undesirable, so efforts have to be made to eliminate this effect as much as possible. Two such elimination methods are the addition of buffer gas atoms to the cell or the use of anti-relaxation wall coatings.

Buffer gas atoms reduce wall-induced relaxation by slowing down the diffusion of the alkali atoms from the centre of the cell to the glass walls. Therefore, they collide with the walls less often. The more buffer gas atoms there are, the longer the alkali atoms take to diffuse toward the walls. The relaxation rate is a balance between the diffusion-mediated wall collisions and collisions between the buffer gas atoms and the alkali atoms. Bernheim et al. [124] showed that disorientation of the alkali atom due to collisions between the buffer gas atoms and alkali atoms arise from a spin-orbit coupling between the alkali valence electron spin and the relative orbital angular momentum of the two particles in the alkali atom-buffer gas collision, which randomises the electron spin. Helium is the most commonly used buffer gas because it has a low probability of spin-destruction collisions due to the small amount of spin-orbit interaction between the alkali atom and helium atom

[124]. Hence, it has a small disorientation cross section compared to other gases [124]. The disorientation cross section which characterises the alkali atom-buffer gas collision is roughly proportional to the cube of the atomic number, and helium has the lowest atomic number of the noble gases [125].

In the experiments described here, anti-relaxation wall coatings were chosen over buffer gas atoms for reasons which will become apparent later in this section. Essentially, wall coatings are molecules which cover the surface and prevent the alkali atoms from touching the bare glass surface. They are chemically inert and allow the atoms to bounce off the walls numerous times without depolarisation. For magnetometers operating at room temperature such as the one described in this thesis, paraffin is used to coat the glass walls. Paraffin has a very low polarisability. Using paraffin-coated glass cells to contain atoms was first proposed in the 1950's by Ramsey [126], and in 1958, Dehmelt, Robinson, and Ensberg experimentally observed that the polarisation of the atomic spins were preserved in a paraffin-coated glass cell [127]. Since then, numerous experiments into paraffin have resulted in the development of an extremely high quality coating capable of allowing atoms to bounce off the walls at least one thousand times without losing its orientation [2]. Paraffin melts and loses its effectiveness above temperatures of about $60-80$ °C [2], hence it is the preferred choice for magnetometers operating at room temperature.

Using paraffin-coated cells offers several advantages over buffer gas atoms. Spin-destruction collisions between alkali atoms and buffer gas atoms cause broadening of the signal linewidth which limits the magnetometer performance especially in high pressure cells. On the other hand, a superior quality paraffin-coated cell results in very minimal depolarisation. The smaller the cell, the higher the buffer gas pressure needs to be in order to maintain the same diffusion time. Hence, the linewidth improvement using paraffin-coated cells over buffer gas atoms is more pronounced for smaller cells.

The presence of magnetic field gradients results in atoms in different parts of the cell experiencing different local fields thus they precess at different frequencies. Because they take a long time to diffuse to the walls, most of the alkali atoms in

a high pressure glass cell spend most of their time in the centre of the cell. These atoms will feel their own local field while atoms nearer to the walls will experience a different field. Consequently, the precession at different frequencies will lead to a broadening of the linewidth of the recorded signal. In contrast, the atoms in a paraffin-coated cell are free to move all over, thus they effectively average the field over the entire cell volume. This also means that it is not necessary to expand the diameter of the probe beam to the same size as the cell in order to measure the atoms' Larmor precession; a small diameter can suffice. In a similar fashion, when creating the collective atomic spin, the pump beam can also remain small because paraffin preserves the polarisation of the atomic spins in the parts of the cell not actively pumped.

Chapter 4

Experimental Setup

4.1 Introduction

This chapter will provide the technical details of the rf magnetometer used in the work described in this thesis. A schematic of the setup is shown in Figure 4.1.

The cell is placed in a uniform static magnetic field, $\boldsymbol{B}_0$, created by a solenoid. $\boldsymbol{B}_0$ is directed along the x-axis. The weak oscillating rf magnetic field, $\boldsymbol{B}_{rf}$, oriented orthogonally to $\boldsymbol{B}_0$, in the y-direction, is produced by the rf coils. $\boldsymbol{B}_{rf}$ generates the transverse spin polarisation component. Sweeping the rf field allows an rf spectrum to be recorded. Surrounding the solenoid are three cylindrical layers of mu-metal shields with end caps which cancel the ambient magnetic field and any stray inhomogeneities.

The master laser, frequency locked to the $6^2S_{\frac{1}{2}}F = 3 \rightarrow 6^2P_{\frac{3}{2}}F' = 3,4$ Cs crossover transition and then frequency shifted by 160 MHz to the red by an acousto-optic modulator (AOM) in a double pass configuration, produces the 8 mm diameter circularly polarised pump beam which optically pumps the atoms. Pumping is achieved using indirect optical pumping, described in chapter 2 section 2.5.1.1, in which off-resonant optical pumping combined with SEC is used to transfer the orientation created in the $F = 3$ ground state to the $F = 4$ ground state.

The probe beam is produced by another laser, called the slave, which is offset locked to the master. It propagates along the z-axis with polarisation parallel to $\boldsymbol{B}_0$ and has a diameter of 8 mm. After traversing the cell, the probe beam is analysed by

a polarimeter consisting of a polarising beam splitter (PBS) and two photodiodes. The two orthogonally polarised output components from the PBS are sent to two photodiodes of a Thorlabs balanced photodetector. The signal representing the difference between the photocurrents of the photodiodes is then processed by a lock-in amplifier or a spectrum analyser. Each of these setup components, along with the process of offset locking, will be described in detail in this chapter.

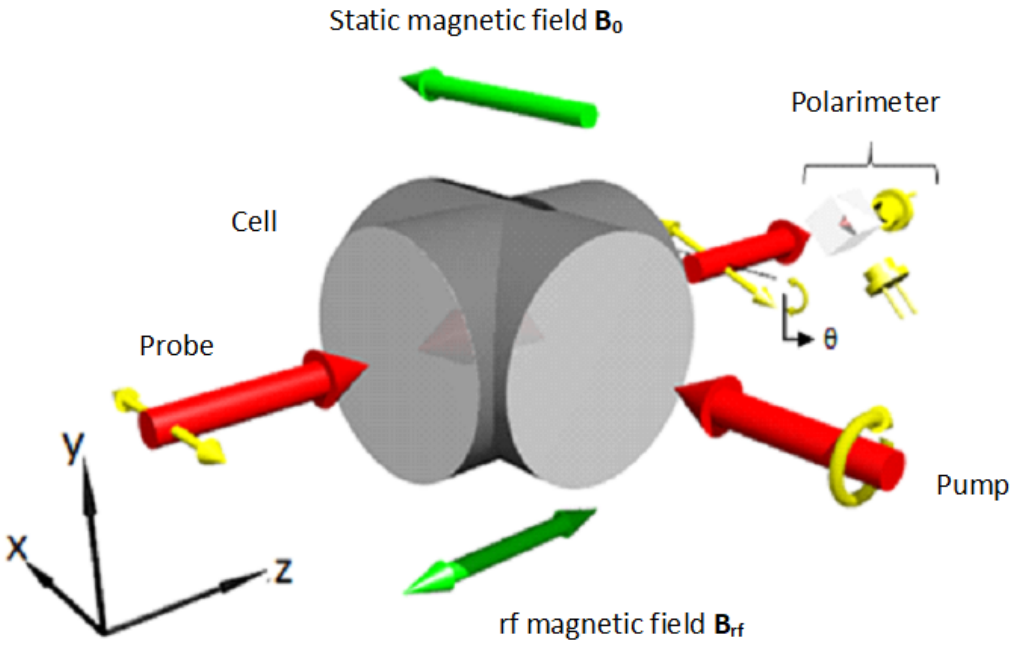

Figure 4.1: Geometry of the experiment. Cs atoms are contained in a cross-shaped glass cell with paraffin coated walls. An 8 mm diameter circularly polarised pump beam tuned to the $6^2S_{\frac{1}{2}}F = 3 \rightarrow 6^2P_{\frac{3}{2}}F' = 3,4$ crossover transition pumps atoms along the static magnetic field, $\boldsymbol{B}_0$. The oscillating rf field along the y-direction, $\boldsymbol{B}_{rf}$, induces a transverse spin component which precesses about $\boldsymbol{B}_0$. An 8 mm diameter probe beam propagating along the z-direction and linearly polarised along the x-direction is used to detect the transverse spin component by using a balanced polarimeter consisting of a polarising beam splitter (PBS) and commercial balanced photodiodes.

One of the main objectives of this thesis was to develop a sensitive, compact magnetometer able to be easily transportable. With this criterion in mind, the setup that was developed is divided into sections to aid easy assembly and disassembly. This is achieved by using four breadboards. The laser modules are housed on one

breadboard, the components required to produce the appropriate pump and probe beams are placed on their own individual breadboards, and the fourth breadboard houses the detection components. The laser modules are linked to the pump and probe beam systems using optical fibres. The advantages of such a setup will be discussed.

4.2 Optical System

The purpose of the optical system is to produce two beams (a pump and a probe) with fixed polarisation and frequency but adjustable intensity. It consists of a Thorlabs $300 \times 300 \times 25$ mm breadboard attached to a Thorlabs $600 \times 600 \times 50$ mm breadboard. The $300 \times 300 \times 25$ mm breadboard holds the lasers and optical modules produced by Vescent Photonics, while the Thorlabs $600 \times 600 \times 50$ mm breadboard accommodates the components required to produce intensity modulated pump and probe beams.

4.2.1 Optical Units Breadboard

The $300 \times 300 \times 25$ mm breadboard houses the two laser modules, along with the optical units which enable offset locking of the slave to the master. This section will look at the role of each module and the process of offset locking.

4.2.1.1 Vescent Optical Modules

Two D2-100 distributed Bragg reflector (DBR) lasers are used to provide the pump and probe beams. A DBR laser consists of a gain region and a separate DBR grating region, monolithically fabricated over a continuous waveguide [128]. The DBR grating region is a Bragg mirror, that is, a light-reflecting device (a mirror) based on Bragg reflection at a periodic structure [129]. This provides wavelength-dependent feedback to define the emission wavelength of the beam. The two DBR laser modules operate on the Cs D2 line at a wavelength of 852 nm with a maximum current of 150 mA and maximum output power of 80 mW [130].

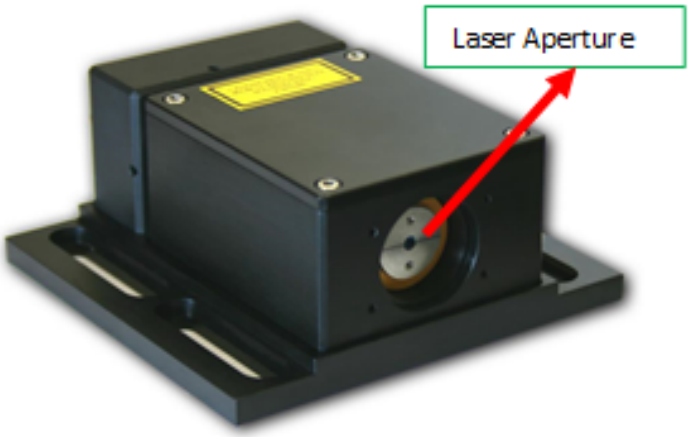

Figure 4.2: Picture of Vescent D2-100 distributed Bragg reflector (DBR) laser used in the experiments described in this thesis. The laser operates on the Cs D2 line at a wavelength of 852 nm with a maximum current of 150 mA and maximum output power of 80 mW. Image taken from [130].

4.2.1.2 Saturated Absorption Spectroscopy Module

The beam from the master laser module enters the D2-210 saturated absorption spectroscopy module. This module provides the error signal, derived from the saturated absorption spectroscopy of atomic Cs, to stablilise (lock) the frequency of the master laser to a particular Cs D2 hyperfine transition, by removing Doppler broadening [131].

As stated in chapter 2 section 2.3.3, Doppler broadening is due to the motion of the Cs atoms. An atom moving towards the laser and seeing blue shifted radiation, will only be able to absorb radiation at a frequency less than the resonant frequency, ν_0, of a transition from an F to F' level when the atom is stationary in the rest frame of the laser [62]. Similarly, an atom receding from the laser will only absorb radiation greater than ν_0. Mathematically, this is given as [62]:

$$\nu_{laser} = \nu_0(1 \pm \frac{v_z}{c}). \tag{4.1}$$

where ν_{laser} is the laser frequency absorbed by the atom, v_z is the velocity of the atom moving in the z-direction which is along the line of sight of the laser, and c is the speed of light. Therefore, there will be an ensemble of atoms at different

velocities absorbing a range of laser frequencies.

The saturated absorption spectroscopy module, containing two Cs vapour cells, picks off a tiny portion of the main beam and splits it into three beams: two less intense probe beams and one intense pump beam. One probe beam, propagating in the z-direction, passes through the reference vapour cell to the reference photodiode. This signal is a Doppler broadened absorption spectroscopy signal. The other probe beam, together with the pump beam, are oriented using optics (PBSs, mirrors, half-waveplate) so that they counter-propagate, in the z-direction, through the second vapour cell. The signal from the probe beam after it passes through the cell is detected on another photodiode while the exiting pump beam is blocked [131]. The two beams interact with the atoms' z-component of velocity, v_z, in the cell. The pump beam, propagating in the left direction, will interact with atoms moving to the right towards the pump beam. These atoms will see the laser frequency, ν_{laser}, blue shifted, that is, it will be at a higher frequency. When the atoms are at the appropriate velocity, v_z, given by equation (4.1), the laser frequency will be shifted to ν_0 in the rest frame of the atom, hence the atoms will be able to absorb the pump beam. Similarly, by the same logic, those atoms moving toward the right-propagating probe beam will be able to absorb its light when they are at the same v_z as the atoms that absorbed the pump light. Conversely, atoms moving away from both beams will see the laser frequencies red-shifted, that is, at a lower frequency. When they are at the correct v_z, they will be able to absorb the light. It is important to note that the pump and probe beams interact with different groups of atoms [62].

Now, atoms with $v_z = 0$ in the region overlapping the two beams can absorb light from both of them. The stronger pump beam depletes the populations by optical pumping causing most atoms to occupy a dark state. These atoms will absorb fewer photons from the probe beam which will pass on with reduced absorption, and the intensity reaching the signal photodiode will increase [132]. This only happens because the pump and probe beams are interacting with the same atoms. The signal will contain Doppler free dips "riding" on a Doppler broadened profile [62]. These dips correspond to the three hyperfine transitions from one of the ground states to

the excited states. The reference probe beam interacts with a different set of atoms so does not feel the effect of the pump beam, therefore the intensity recorded on the reference photodiode will be less than the signal photodiode. Subtraction of the two beams will reveal the hyperfine transitions because Doppler broadening from both beams has been eliminated.

In addition to the hyperfine transitions, there are three "crossover" absorption peaks of similar width, but larger amplitude, located exactly midway between each pair of hyperfine transitions [63, 132]. The crossover peaks occur when the laser frequency is halfway between two transitions that share a common ground state, for example, the $6^2S_{\frac{1}{2}}F = 3 \rightarrow 6^2S_{\frac{3}{2}}F' = 2$ transition and the $6^2S_{\frac{1}{2}}F = 3 \rightarrow 6^2S_{\frac{3}{2}}F' = 3$ transition. When the laser frequency is at the midpoint of the two transition frequencies, a group of atoms at the appropriate velocity will see the probe beam blue-shifted to the $6^2S_{\frac{1}{2}}F = 3 \rightarrow 6^2S_{\frac{3}{2}}F' = 2$ transition and the pump beam red-shifted to the $6^2S_{\frac{1}{2}}F = 3 \rightarrow 6^2S_{\frac{3}{2}}F' = 3$ transition. Additionally, another group of atoms will see the opposite Doppler shifts of the probe and pump beams that results in a crossover resonance at the same frequency. For each crossover resonance, the absorption is saturated, not by stationary atoms but by two classes of moving ones [62].

This signal from the saturated absorption spectroscopy module is sent to the D2-125 laser servo which allows the master to be locked to any of the transitions from either the $F = 3$ or $F = 4$ ground states to the excited states.

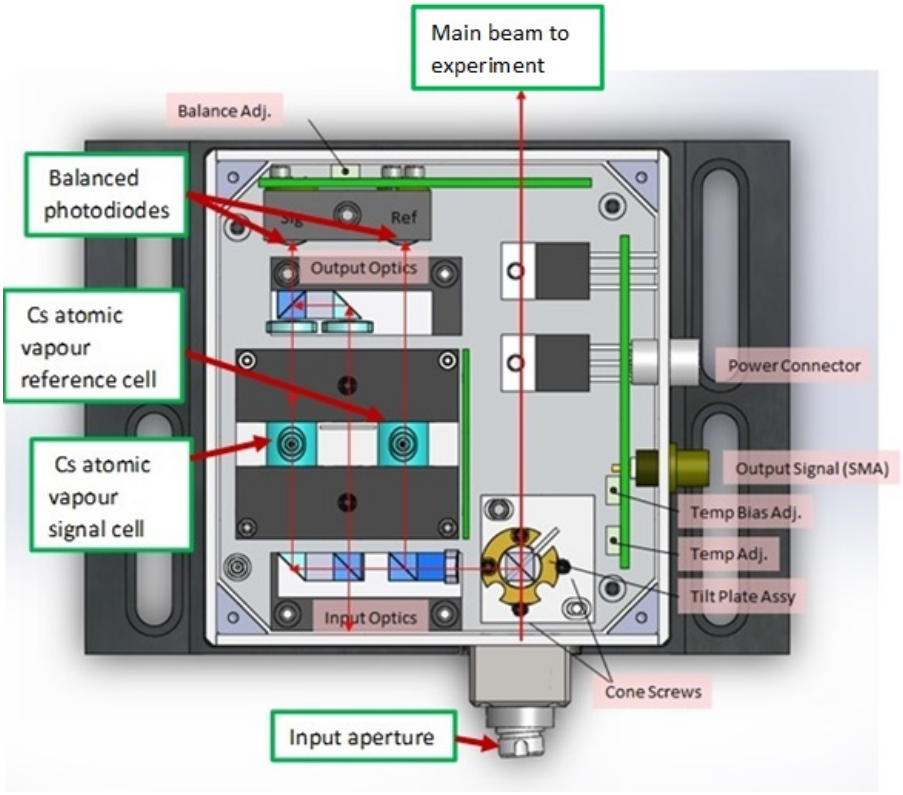

Figure 4.3: Diagram illustrating the components inside the D2-210 spectroscopy module [131]. This module uses the principle of saturated absorption spectroscopy to reveal the Cs D2 hyperfine transitions by eliminating Doppler broadening caused by atomic motion. In one cell, known as the signal cell, atoms with a velocity component, $v_z = 0$ in the region overlapping the counter propagating pump and probe beams in the z-direction will be able to absorb photons from both beams. The stronger pump beam depletes the population of the ground state which means fewer photons are absorbed from the probe beam so it passes through the cell with reduced absorption, to the signal photodiode. The resulting signal consists of saturated absorption dips "riding" on a Doppler broadened signal. This signal is subtracted from the Doppler broadened reference signal, obtained from the second vapour cell in which a second probe beam passes through to the reference photodiode. The resulting signal shows the Doppler-free hyperfine transitions. Image taken from [131]

4.2.2 Offset Locking

Offset locking is made possible through the use of the D2-150 heterodyne module and the D2-135 Offset Phase Lock Servo (OPLS) [133].

The OPLS is used to offset lock the slave laser to the master by locking the frequency and phase of the input beatnote to a (multiple of the) reference frequency [134]. A beatnote is a measurement of the frequency difference (or offset) between

the two lasers when they interfere with each other. The beatnote is produced using the heterodyne module in which the master and slave laser beams enter the module, such that they are oriented 90° relative to each other [135]. A tiny portion from each beam is picked off using adjustable PBSs and made to overlap, producing the beatnote signal [135]. The beatnote to the OPLS is divided by the user controlled parameter, N, which can be 8, 16, 32 or 64, before its frequency and phase is compared to the reference frequency [134]. The reference frequency is obtained either internally from a voltage controlled oscillator (VCO), or provided externally by the user. A VCO is an electronic oscillator where the input tuning voltage is used to set the oscillation frequency [136]. For the experiments described in this thesis, the VCO was used to provide the reference frequency.

The comparison of the phase and frequency of the divided-by-N beatnote with the reference frequency is performed by the phase sensitive detector (PFD) of the OPLS. When no phase slips exist between the two signal input frequencies, the PFD outputs a signal proportional to the phase difference between the two frequencies. This output signal is a true phase-lock error signal. When phase slips occur, the PFD acts as a frequency comparator, aiding the initial lock and enabling the OPLS to function as a frequency offset lock for lasers which have significant phase noise such as the DBR and distributed feedback (DFB) lasers [134].

The output of the OPLS adjusts the frequency of the slave laser to lock the frequency offset between the two lasers. The locked frequency offset is given by the formula [134]:

$$Offset = N \times Reference\ Frequency. \tag{4.2}$$

By adjusting either the reference frequency or N, the desired offset frequency can be set.

The offset frequency can be anywhere from 250 MHz up to 10 GHz [134]. To enable successful offset locking at a particular frequency, the OPLS has to be in the correct operating mode. The operating mode is determined by the divide-by-N settings and the reference frequency settings. Table 4.1 shows the offset frequency

ranges for the twelve different modes [134].

Reference Frequency Setting	Divide-by-N Settings			
	N=8	N=16	N=32	N=64
External	250-1920	480-3840	960-7680	1920-10000
External Reference Input Frequency	30-240			
VCO Low	385-850	770-1700	1540-3400	3080-6800
VCO High	770-1700	1540-3400	3080-6800	6160-10000

Table 4.1: Table showing the offset frequency ranges for the twelve modes of the D2-135 Offset Lock Servo [134]. All frequencies are in MHz.

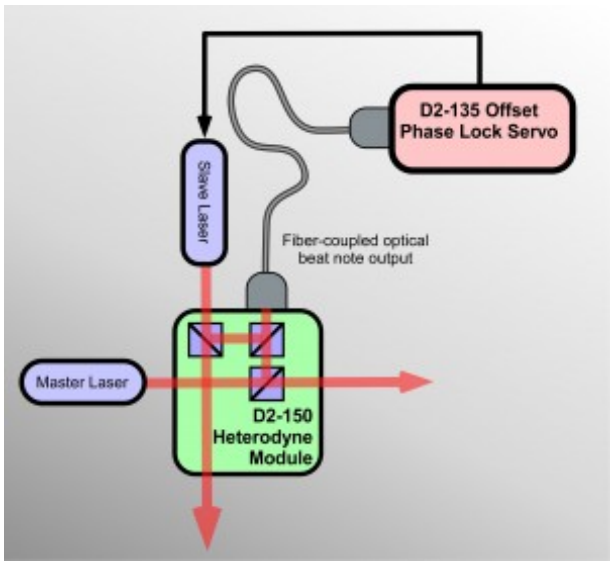

Figure 4.4: Diagram showing the setup used for offset locking the slave laser to the master. The D2-150 heterodyne module produces a beatnote which is the frequency difference between the master and slave. The beatnote is sent to the D2-135 Offset Lock Servo (OPLS) which compares its frequency and phase to the reference frequency of the voltage controlled oscillator (VCO). The output of the OPLS adjusts the frequency of the slave laser to lock the frequency offset between the two lasers. The offset frequency range is from 250 MHz up to ± 10 GHz. Image taken from [135].

The unused portion of each beam exits the heterodyne module through its respective aperture, to be used for experimental purposes.

4.2.2.1 Dependence of the Offset Frequency (Beatnote) on the Slave Laser Current

Section 4.2.2 described how the process of locking at a particular offset frequency is performed. Now, to find the desired offset frequency, the slave laser

current is used to adjust the frequency difference between the two lasers before locking is done. In addition, the current indicates on which side of the fixed master frequency, lies the slave. If an increase in current leads to a decrease in the offset frequency, the slave is blue to master (higher frequency). Conversely, if the increase in current leads to an increase in the offset frequency, the slave is red to master (lower frequency).

To investigate the relationship between the offset frequency lock-point of the slave and its diode laser current, the master was locked to the $6^2S_{\frac{1}{2}}F = 3 \rightarrow 6^2P_{\frac{3}{2}}F' = 3$ transition. Then, for every offset frequency within the range 250 MHz to 10 GHz, the slave current was recorded. Figure 4.5 displays these results.

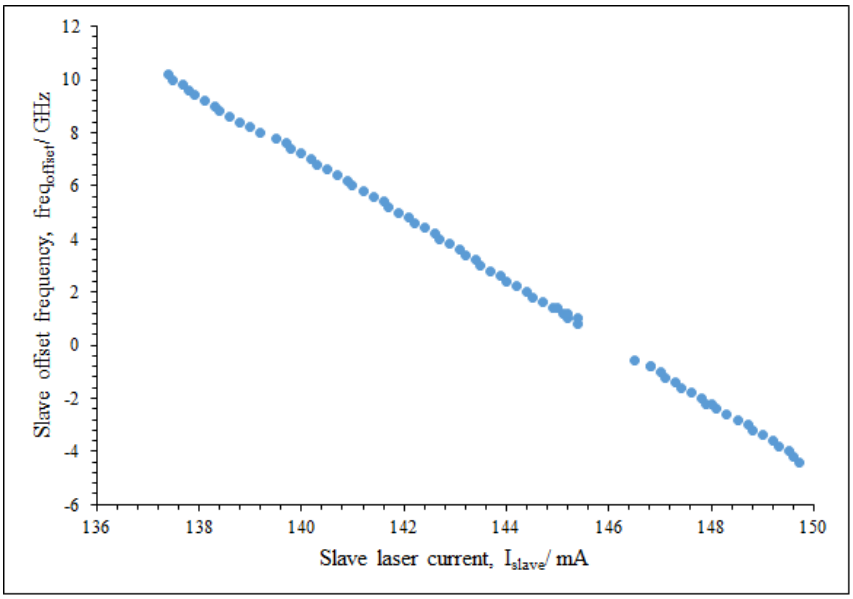

Figure 4.5: Dependence of the offset frequency lock-point of the slave on its laser current. Lock point frequency expressed in terms of how far the slave frequency is from the $6^2S_{\frac{1}{2}}F = 3 \rightarrow 6^2P_{\frac{3}{2}}F' = 3$ transition (lock-point of the master). Positive offset values indicate the slave is at a higher frequency than the master while negative offset values signify the slave is at a lower frequency.

The results indicate a linear dependence between the slave lock-point offset frequency, $\text{Freq}_{\text{Offset}}$, and its laser diode current, I_{slave}. According to Figure 4.5, positive offset frequencies indicate that the slave is at a higher frequency than the master, while negative offsets signify that the slave is at a lower frequency. Gaps in the data close to 0 GHz offset frequency reveal that it is not possible to perform

offset locking because a beatnote cannot be produced.

4.2.3 Optical Elements Breadboard

The $600 \times 600 \times 50$ mm breadboard contains the optical elements necessary to produce two pump and two probe beams of adjustable intensities. Figure 4.6 shows the arrangement of the elements used to produce the four beams. All elements used were manufactured by Thorlabs except the AOMs. Two important elements in the setup will be the topics of discussion in this section.

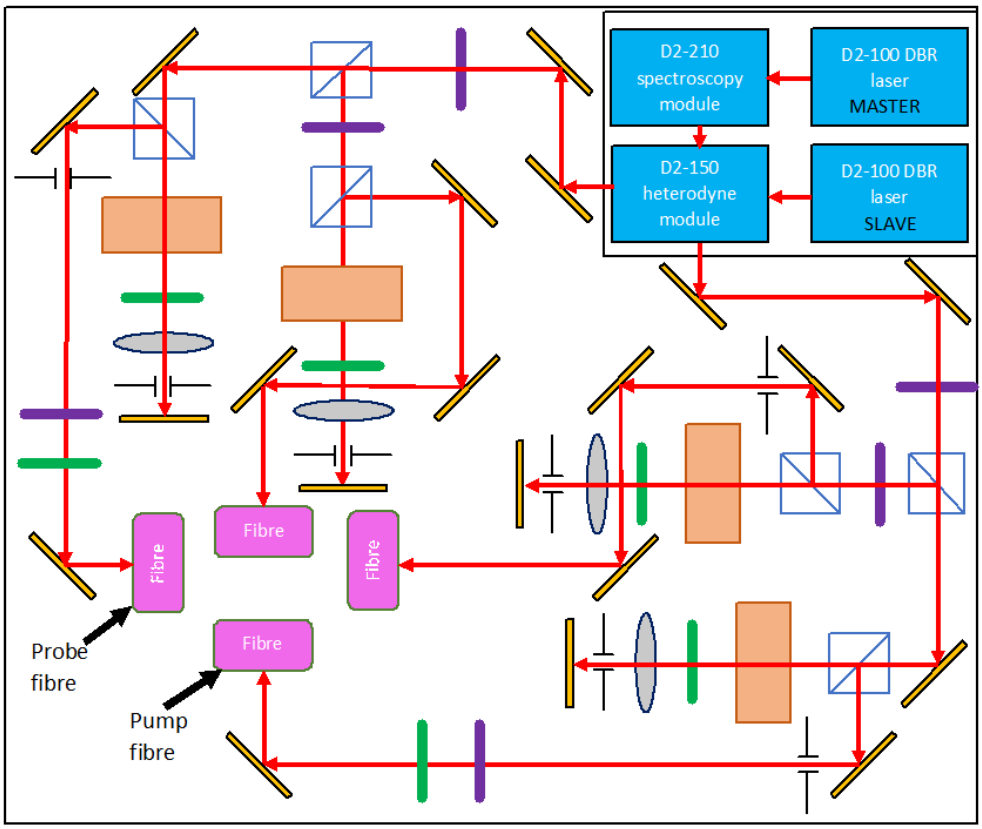

Key

Element	Description	Identifying Code
	Thorlabs ½" diameter broadband dielectric mirror, 750-1100 nm- BB05-E03	BB05-E03
	Thorlabs 1/2" diameter mounted Zero-Order Half-Wave Plate, Ø1" Mount, 850 nm	WPH05M-850
	Thorlabs 1/2" diameter Polarizing Beamsplitter (PBS) Cube, 620 - 1000 nm	PBS122
	Crystal Technologies Gooch and Housego AOM	3080-122
	Thorlabs 1/2" diameter mounted Zero-Order Quarter-Wave Plate, Ø1" Mount, 850 nm	WPQ05M-850
	Thorlabs N-BK7 Plano-Convex Lens, Ø1", f = 100.0 mm, AR Coating: 650-1050 nm	LA1509-B
	Thorlabs SM1 Lever-Actuated Iris Diaphragm (0.8 - 12 mm diameter)	SM1D12
Fibre	Thorlabs FiberPort, FC/PC, f=11.0 mm, 600 - 1050 nm; Ø2.38 mm Waist. Thorlabs Patch Cable, PM, FC/APC,780 nm, Panda style, 5m	PAF-X-18-PC-B P3-780PM-FC-5

Figure 4.6: Schematic of the optical system. A $300 \times 300 \times 25$ mm breadboard houses the lasers and optical modules to allow offset locking of the slave to the master. This breadboard sits on a $600 \times 600 \times 50$ mm which contains the components able to produce pump and probe beams of adjustable intensities.

The first key element is the AOM. There are four Crystal Technology 3080-120 80 MHz AOMs [137], set in a double pass configuration for the purpose of shifting the frequencies of the four beams, and providing a means with which to control the beam intensities. An AOM is a device which is used to modulate the intensity, frequency and direction of a laser beam [136]. It uses the acousto-optic effect which is the interaction of sound (most often in the rf range) and light in a crystalline material to diffract and shift the frequency of the light. An rf signal applied to a piezo-electric transducer causes it to vibrate, generating acoustic waves in the crystalline material, attached to the transducer. Areas of compression and rarefaction are created in the crystal, resulting in periodic changes in the refractive index. When light is input on the device, it is diffracted into different orders. The beam diffraction angle is a function of the modulation frequency. This can cause alignment problems in any setup when the AOM is frequency scanned. Therefore, to eliminate such issues in experiments, the AOM is used in a double pass configuration that focuses on the first order diffracted beam [138]. The components required for the double pass are a quarter waveplate, a plano-convex lens and a mirror set in a cat's eye configuration with an iris between the lens and mirror. In a standard cat's eye configuration, the distance between the AOM and lens, and the lens and mirror is equal to the focal length of the lens. The advantage of the cat's eye is that regardless of the beam diffraction angle, all the rays emanate from the focal point of the lens, hence the zeroth and first order beams are parallel, so changing the frequency only changes the spacing between the beams [138]. The quarter waveplate circularises the polarisation of the output beam from the AOM. The iris blocks the undiffracted zeroth order before the mirror, so only the first order, shifted by 80 MHz, is retroreflected from the cat's eye, and passes through the quarter waveplate, where its circular polarisation is converted back to linear polarisation such that the polarisation vector is perpendicular to the polarisation vector of the original incident beam. On its second pass through the AOM, it is again diffracted, resulting in the new first order overlapping the original incident beam. This new first order beam is again shifted by 80 MHz, making the total frequency shift 160 MHz. This

beam can be separated from the original incident beam with a PBS. Figure 4.7 illustrates the double pass configuration. The two pump beams are diffracted to the -1 order, therefore, their frequencies are shifted 160 MHz to the red while the two probe beams are diffracted to the $+1$ order, thus, they are shifted 160 MHz to the blue. The amount of light diffracted into the first order depends on the intensity of the acoustic waves in the material. Therefore, the beam intensity is controlled by modulating the intensity of the acoustic waves.

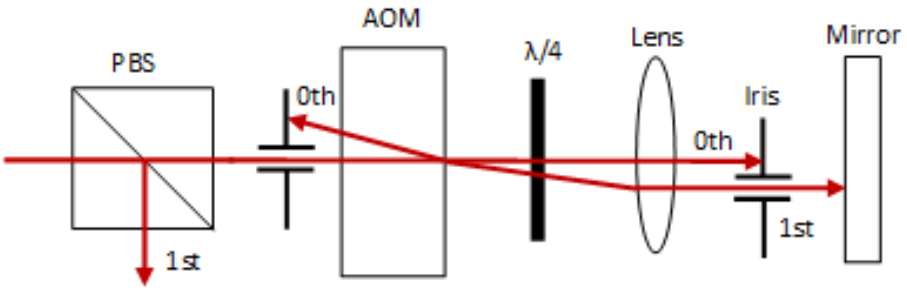

Figure 4.7: Diagram showing the double pass AOM setup. On the first pass, the quarter waveplate ($\lambda/4$) circularises the output polarisation beam. The undiffracted zeroth order is blocked whilst the first order is reflected back through $\lambda/4$, which converts the polarisation back to linearly polarised light, such that the polarisation vector is perpendicular to the polarisation vector of the original incident beam. The AOM diffracts the beam a second time, resulting in the new first order overlapping the original input beam. The PBS separates the two beams. The beam after the PBS has been shifted a total of 160 MHz (80 MHz on both passes).

The second key element is the single-mode polarisation maintaining fibre patch cable (P3-780PM-FC-10), of which there are four. The Fibreport collimator (PAF-X-18-PC-B) with an 18.4 mm coupling lens allows injection of the beam into the fibre patch cable. A polarisation maintaining fibre is a specially designed fibre with a strong built-in birefringence [139]. If the light injected into the fibre is aligned with one of the birefringent axes, the polarisation state will be maintained throughout the fibre, even if the fibre is bent. Stress rods run parallel to the fibre's core and apply stress, creating birefringence within the core. The style of fibre which is used in the experiments described in this thesis is the panda style which has cylindrical stress rods. Historically, they have been used in telecom applications because it is easier to maintain uniformity in the cylindrical stress rods, over very long lengths

when manufacturing [140]. This feature is advantageous because it means that the polarisation maintaining capability is not restricted by the length of fibre [140]. On both ends of the patch cable are fibre connectors with angled physical contact (FC/APC). These connectors are made by polishing the fibre at an 8° angle to ensure that reflections at the fibre-air interface are not sent back to the core, thereby reducing back reflections and feedback problems, hence improving stability.

In order to minimise the polarisation fluctuations at the output of the fibre, quarter- and half-wave plates were used to match the polarisation of the light, coupled into the fibre, with the fibre axis.

The fibre patch cables allow flexibility in the distance of the pump and probe beams from the lasers, and how and where the rf magnetometer is set up. In addition, the fibres allow the lasers to be used in other setups.

Though the optical elements breadboard provides two pump and two probe beams, only one pump and one probe beam were required for the experiments described in this thesis.

4.2.4 The Pump Beam System

A $300 \times 300 \times 25$ mm breadboard holds the elements necessary to produce a circularly polarised collimated beam appropriate for indirect optical pumping. All elements used, including the breadboard, were manufactured by Thorlabs.

A f = 100 mm 25.4 mm diameter plano-convex lens (LA1309-B) was necessary to collimate the divergent output beam from the fibre. When the light was coupled into the fibre, it was ensured that the polarisation of the light was aligned with the fibre axis using quarter- and half-waveplates. However, small oscillations in the polarisation of the light at the fibre output were observed. This is most likely due to the birefringence introduced by the connectors which reduce the polarisation level at the output. In chapter 3 section 3.3, it was stated that the sensitivity of the magnetometer depends on producing a long polarisation lifetime. Thus, it is critical for the pump beam to have a very stable polarisation. To reduce these fluctuations, a 10×10 mm clear aperture Glan Thompson polariser (GTH10M-A) was used. This polariser consists of two right angled prisms cemented together by their long

faces so no air gap exists. It has an extinction ratio of 100000 : 1 [141]. This was necessary to ensure that only one polarisation state was transmitted. The iris (SM1D12) sets a beam diameter of 8 mm so that the beam passes unattenuated through the 12.5 mm diameter quarter waveplate (WPQ05M-850) which circularly polarises the light.

A very important benefit of the breadboard design is that after the beam is circularly polarised it encounters two mirrors arranged in a periscope setup before entering the cell. This allows maximum flexibility as the beam can be adjusted to any desired height.

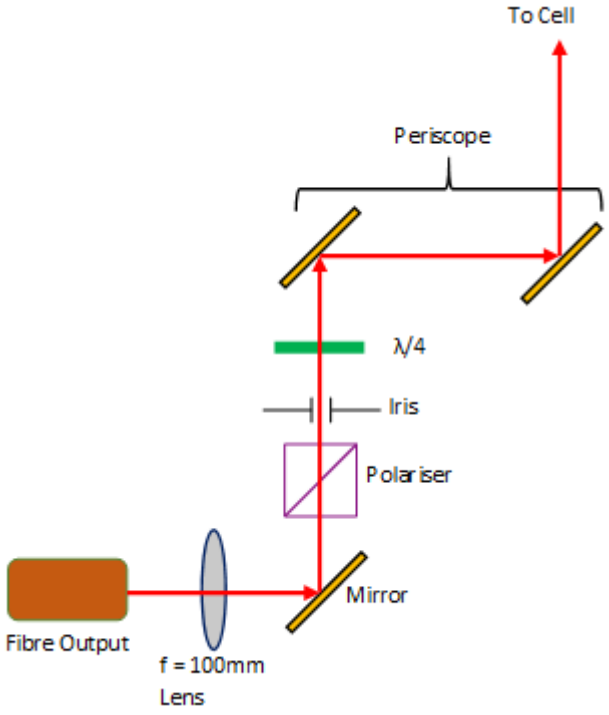

Figure 4.8: The Thorlabs optical elements used to produce the circularly polarised pump beam. The divergent beam from the fibre is collimated with a f = 100 mm plano-convex lens before passing through the Glan Thompson polariser which ensures only one polarisation state is transmitted. The iris sets a beam diameter of 8 mm and the quarter waveplate ($\lambda/4$) circularises the beam before it enters the cell.

4.2.5 The Probe Beam System

The $300 \times 300 \times 25$ mm probe beam breadboard is used to accommodate the components used to produce a horizontally linearly polarised probe beam. All com-

ponents used, including the breadboard, were manufactured by Thorlabs.

Like the pump beam breadboard, the output beam from the probe fibre is collimated with a 25.4 mm diameter plano-convex lens with focal length, f = 100 mm. To ensure that only horizontal linearly polarised light is produced, a 12.5 mm diameter half waveplate (WPH05M-850) placed immediately after the fibre output before it diverges greatly, together with a 10 mm x 10 mm clear aperture Glan Thompson polariser (GTH10M-A) after the lens ensures that only horizontally linearly polarised light is produced. This is essential for balanced polarimetry, as discussed in section 4.2.8. The diameter of the beam was reduced using two 25.4 mm diameter lenses of focal lengths, f = 100 mm and f = 50 mm, to a diameter of 8 mm marked by an iris (SM1D12) so that it is small enough to enter and exit the cell. Like the pump beam, the probe beam encounters two mirrors arranged in a periscope setup before entering the cell.

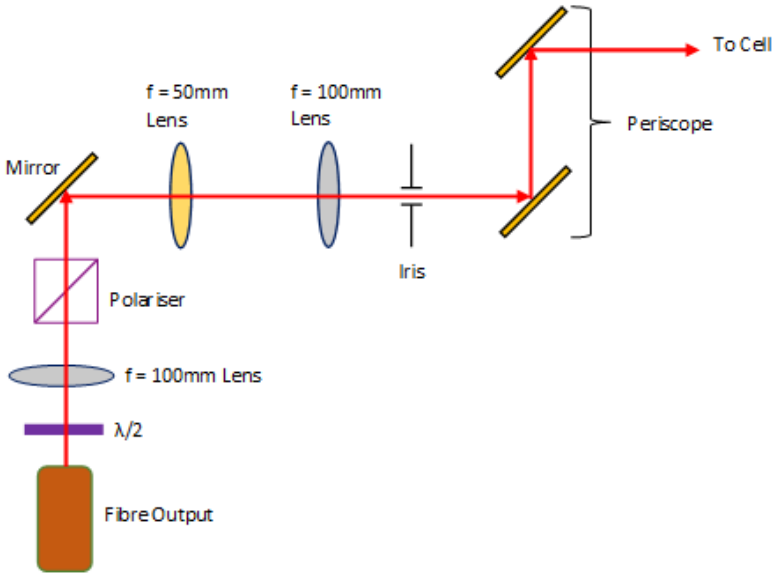

Figure 4.9: The Thorlabs optical elements used to produce the linearly polarised probe beam. The divergent beam from the fibre is collimated with a f = 100 mm plano-convex lens. The half waveplate ($\lambda/2$) and the Glan Thompson polariser ensure that horizontal linearly polarised light is produced. The f = 100 mm and f = 50 mm plano-convex lenses reduce the size of the beam before it passes through an iris which sets a beam diameter of 8 mm into the cell.

4.2.6 Non-Optical Setup

4.2.6.1 Atomic Vapour Cell

The cell containing the Cs alkali atoms in a vapour is the heart of the magnetometer. The cell is a cross-shaped glass cell which can be thought of as two intersecting cylinders of length 22 mm, with four windows of diameter 22 mm. The volume of the overlap of the two cylinders, known as the bicylinder, can be calculated from the following formula [142]:

$$V = \frac{16}{3}r^3 = \frac{16}{3}11^3 \approx 71 \text{ mm}^3. \tag{4.3}$$

where the radius, $r = 11$ mm. The cross-shape ensures that the pump and probe beams are at right angles to each other. The walls are coated with paraffin to prevent relaxation of the spins' polarisation when the atomic spins collide with the walls, as discussed in chapter 3, section 3.3.5.3.

A stem attached to the top of the centre of the cell contains droplets of solid Cs. The amount of Cs vapour in the cell is governed by the temperature of the cell, which is room temperature for the experiments described in this thesis. This means that the atoms are moving with average velocity [80]:

$$v_{rms} = \sqrt{\frac{3k_BT}{m_{Cs}}} = 137 \text{ ms}^{-1}. \tag{4.4}$$

where v_{rms} is the root mean square velocity of the atoms in any single direction, k_B is the Boltzmaan constant, $T = 295.15$ K is the room temperature in Kelvin (22°C) and m_{Cs} is the Cs atomic mass. The atomic density is $n_{Cs} = 0.33 \times 10^{11}$ cm^{-3} [50]. The cell is placed in an oven for protection and stability.

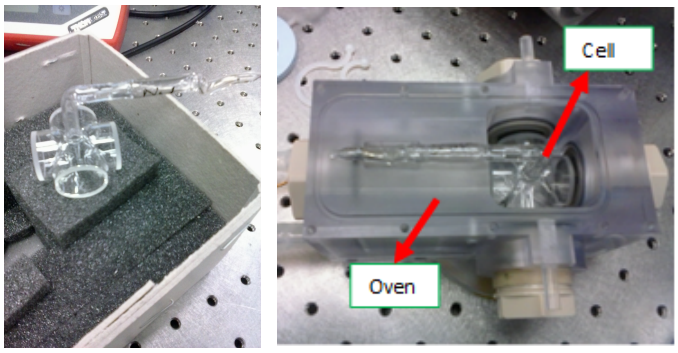

(a) **(b)**

Figure 4.10: (a) The cross-shaped glass cell containing Cs atomic vapour at room temperature. There are four windows of diameter 22 mm and the distance between two opposite windows is 22 mm. (b) The cell placed in the oven.

4.2.6.2 The Bias Solenoid

The uniform static magnetic field, $\boldsymbol{B}_0$, is created by a solenoid consisting of two axial coils placed next to each other but separated by a distance of 6 mm to allow the probe beam to enter and exit [100]. The length of the solenoid is 350 mm with a diameter of 160 mm. Each coil has one hundred turns. $\boldsymbol{B}_0$ is directed along the x-axis.

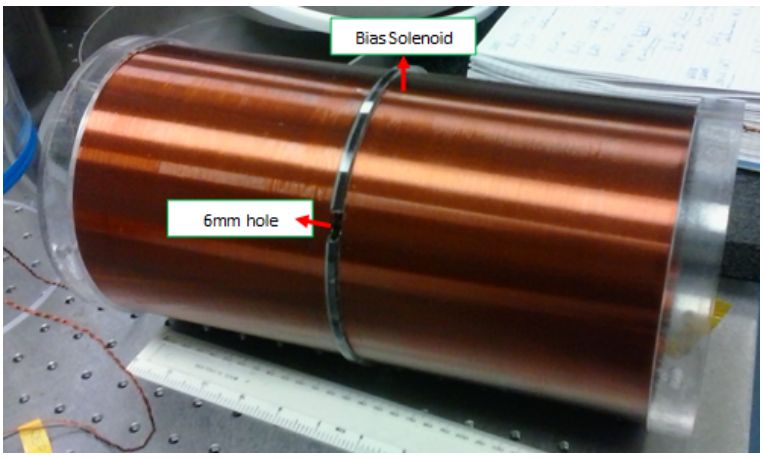

Figure 4.11: The solenoid used to produce the static magnetic field, $\boldsymbol{B}_0$. It consists of two axial coils separated by 6 mm to allow the probe beam to enter and exit. Each coil has one hundred turns and the length of the solenoid is 350 mm with a diameter of 160 mm.

4.2.6.3 Magnetic Shielding

To remove ambient magnetic field noise, three layers of mu-metal cylindrical shields were used (Figure 4.12a). Mu-metal is an alloy of 75% nickel, 15% iron, with copper and molybedenum added for ductility [49]. It has a high magnetic permeability which creates an easier path for magnetic fields to follow, guiding the magnetic field to follow outside of the shielding. The static shielding factor is defined as:

$$T_{shield} = \frac{B_{in}}{B_{out}}. \tag{4.5}$$

where B_{in} and B_{out} are the magnitudes of the magnetic fields at a point with and without the shields in place.

It has been demonstrated both experimentally and theoretically that using multilayer shielding is more beneficial that using a thick single shield [3]. The combination of ferromagnetic and air layers can reduce the magnetic fields inside the shields [143]. Thus, introducing air gaps between the shells can help maintain the same shielding efficiency despite removing a significant part of the shielding material.

The shielding efficiency of cylindrical shields is dependent on the direction of the magnetic field. The axial shielding factor of closed cylindrical shells decreases with shield length. Sumner et al. [144] showed that with a given length, shielding improves with larger radial spacing.

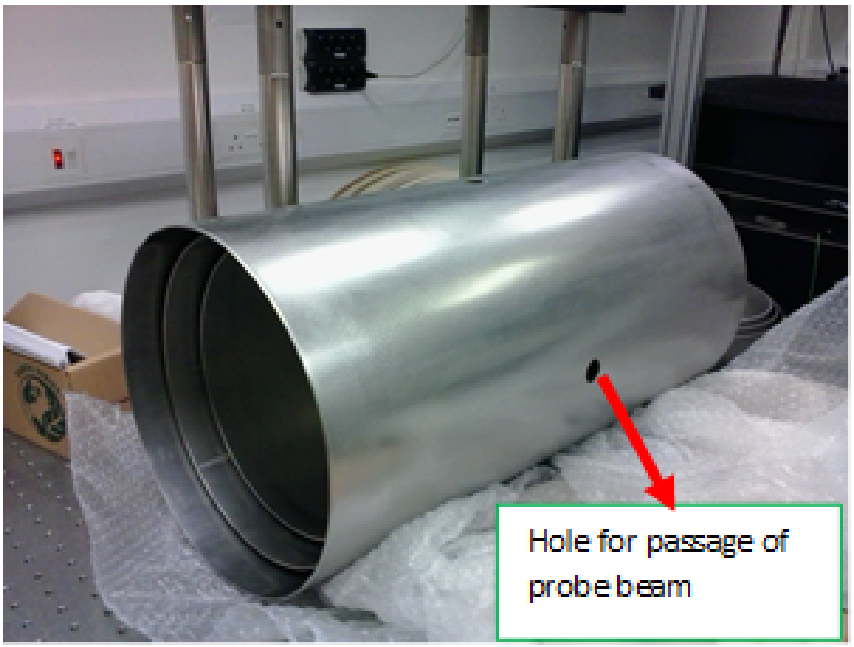

(a)

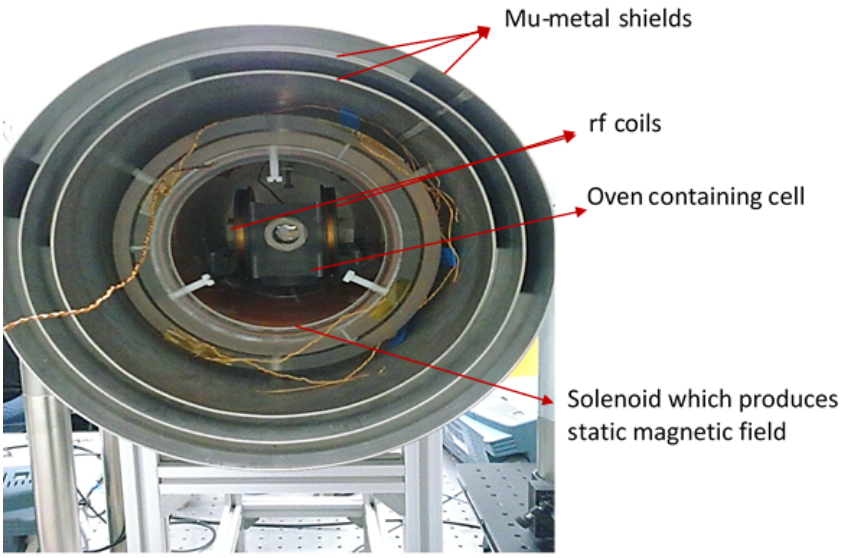

(b)

Figure 4.12: (a) The three layers of mu-metal shields used in the experimental setup. (b) The cell, rf coils and solenoid placed inside the mu-metal shields.

4.2.7 The rf Coils

Two rf coils in a Helmholtz configuration are used to produce the weak oscillating rf field in the y-direction. In such a configuration, a pair of thin, parallel and identical coils separated by a distance equal to their radius is used to generate the highly uniform magnetic field in the space between the coils [145]. These coils

surround the oven containing the cell. The diameter of the coils is 100 mm and each coil has 8 turns. The weak oscillating magnetic field is a 1 Vp – p sine wave produced by the Agilent 33220A 20 MHz waveform generator. Figure 4.14 shows that the uniformity of the magnetic field is maintained beyond the length of the cell which is 22 mm (0.022 m).

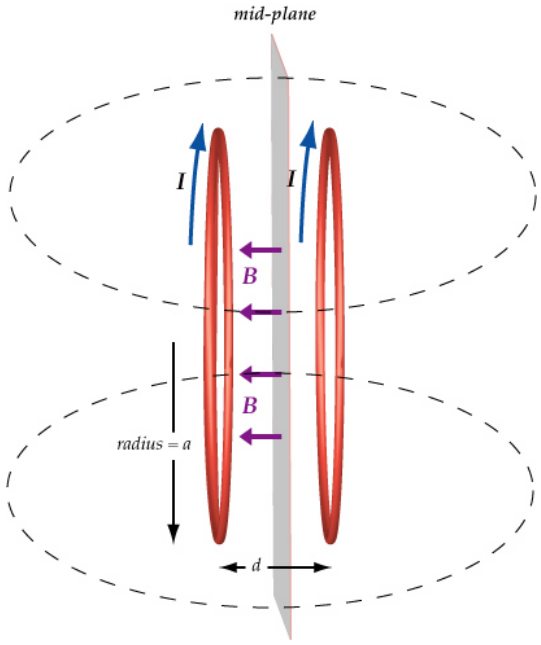

Figure 4.13: Configuration of a pair of Helmhotz coils. The radius, a, of the coils is equal to the distance, d, between the coils in order to produce a highly uniform field in the space between the coils. Image taken from [146].

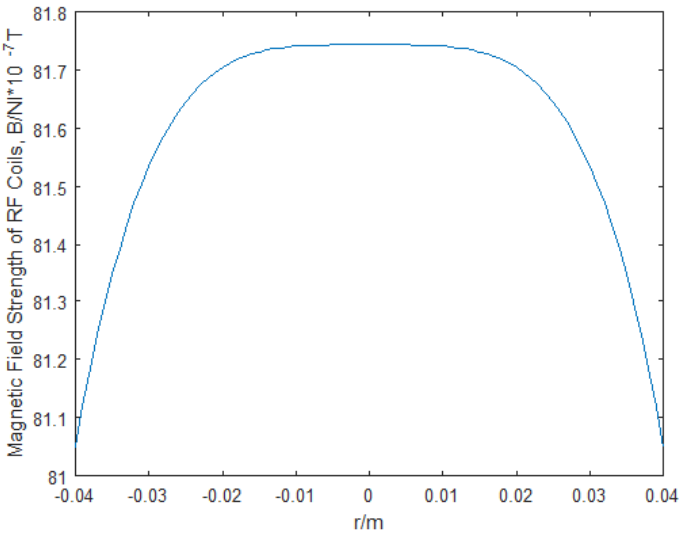

Figure 4.14: Graph showing how the magnetic field, $B/NI \times 10^{-7}$T produced by the rf coils varies as a function of the distance from the axis of symmetry passing between the centres of both coils, r.

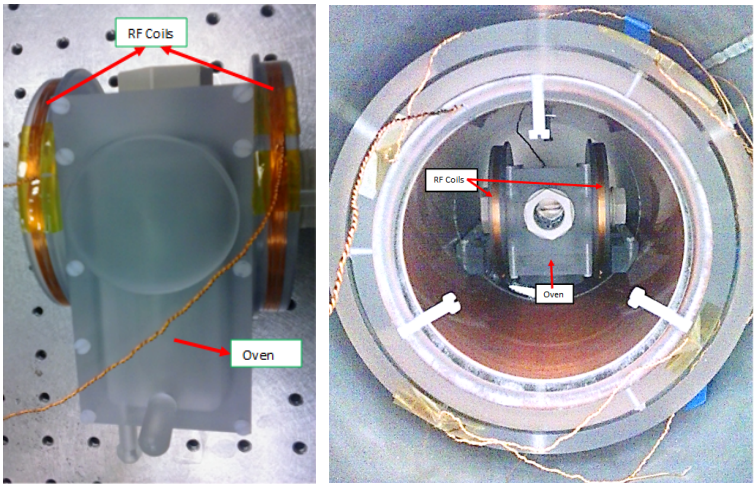

(a) **(b)**

Figure 4.15: (a) The rf coils in a Helmholtz configuration, surrounding the oven containing the Cs cell. (b) The oven and rf coils inside the solenoid.

4.2.8 Detection

There are many methods for detecting the polarisation of the plane of the probe beam but the method used in the experiments discussed in this thesis is the balanced polarimetry technique [147]. Balanced polarimetry measures the orientation of linearly polarised light by splitting the beam into orthogonal polarisation components

and detecting each separately [148]. The advantages of balanced polarimetry are discussed by Bouchiat et al. [149].

In this technique, the cell of alkali atoms is placed between a polariser and PBS (analyser) such that the angle between the incident polarisation and the PBS transmission axis is 45°. Therefore, the intensities of the transmitted and reflected components are equal [150]. In the absence of optical rotation, the intensities of the two components remain the same. Interaction of the probe beam with the alkali atoms by the Faraday effect will rotate the the polarisation by some angle, resulting in non-equal intensities in the two components. The two non-equal intensities will reveal how much the polarisation has rotated.
Mathematically, the two beam intensities are given by:

$$I_1 = I_0 \sin^2(\theta - \frac{\pi}{4}), \tag{4.6}$$

$$I_2 = I_0 \cos^2(\theta - \frac{\pi}{4}). \tag{4.7}$$

whereby the incident intensity, I_0, is given by $I_0 = I_1 + I_2$, I_1 is the intensity of the light hitting the first photodiode, I_2 is the intensity of the light striking the second photodiode and θ is the rotation angle. When $\theta = 0$, the intensities are balanced; when $\theta \neq 0$, the intensities are imbalanced. For rotation angles in which $\theta << 1$, the following equation is used [150]:

$$\theta \approx \frac{I_1 - I2}{2(I_1 + I_2)} \tag{4.8}$$

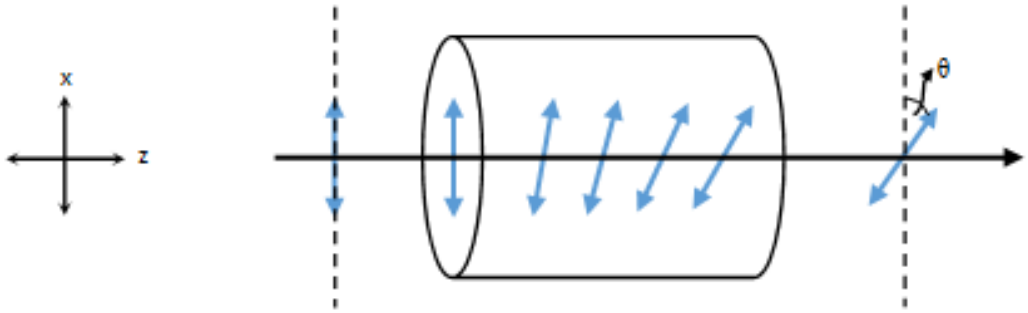

Figure 4.16: Diagram illustrating how the plane of polarisation of linearly polarised light polarised in the x-direction (blue arrows) is rotated as the light propagates in the z-direction through a medium of polarised atomic spins.

For the experiments described in this thesis, the polarimeter consisted of a Thorlabs 12.5 mm diameter PBS with its transmission axis set at 45° to the initial polarisation of the probe beam and, a balanced photodetector. The balanced photodetector is manufactured by Thorlabs (PDB150A Switchable Gain Balanced Amplified Photodetector, Si) and has a maximum input power of 20 mW and operating wavelength range of $320 - 1000$ nm. It has a variable gain, is relatively quiet and has two inputs for monitoring the transmitted and reflected intensity components of the probe beam, along with an output which delivers a voltage proportional to the difference between the two optical input signals. This output signal is sent to the Stanford Research Systems SR844 lock-in amplifier or the Agilent N9010A spectrum analyser.

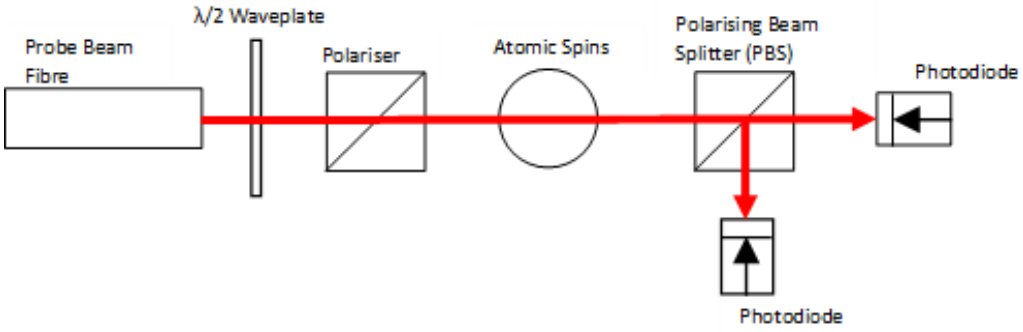

Figure 4.17: The setup for measuring the polarisation rotation of the probe beam. The half waveplate ($\lambda/2$) and polariser sets the polarisation state of the linearly polarised light so that it is horizontally polarised. This means that the angle between the incident polarisation and the PBS transmission axis is 45°. When the polarisation plane is rotated, the two photodiodes will record non-equal light intensities which are dependent on the rotation angle.

Chapter 5

The Role of the Probe Beam in rf Spectroscopy

5.1 Introduction

In this chapter, the role of the probe beam in rf spectroscopy will be investigated. The studies presented here have been performed in the context of optimisation of the rf atomic magnetometer with respect to the probe beam parameter, laser frequency. So far, the studies of the probe laser frequency have been performed in the context of the self-oscillation magnetometer using a modulated pump frequency [151]. The focus in this chapter is on modifications of the magnetometer signal amplitude, linewidth and shape as a function of the probe beam frequency. This is done by exploring the configuration in which indirect optical pumping creates a longitudinal macroscopic polarisation along a static magnetic field, $\boldsymbol{B}_0$, in the ground state of Cs. $\boldsymbol{B}_0$ defines the quantisation axis and the spin component along this axis (x-axis) is represented by the population imbalance within the Zeeman sublevels of the $F = 3$ and $F = 4$ ground state levels. A weak oscillating rf magnetic field, $\boldsymbol{B}_{rf}$, orthogonal to $\boldsymbol{B}_0$ (y-axis) produces a magnetisation component transverse to the field by creating coherences between adjacent Zeeman sublevels. The atomic coherence evolution in the presence of $\boldsymbol{B}_0$ is monitored by the linearly polarised probe beam propagating orthogonally to $\boldsymbol{B}_0$. This is achieved by utilising the Faraday effect in which the evolution of the atomic spin is mapped onto the probe beam.

This mapping results from the circular birefringence of the medium which causes a difference in refractive indices of the two circular components of the linearly polarised probe beam. Consequently, the plane of polarisation of the probe beam is rotated.

Optical probing of the atomic spin with a frequency tuned near and far from resonance can be divided into two categories. The first category is known as the off-resonant regime. In this regime, an effective Hamiltonian is used to describe the interaction between the probe beam and the atomic spins (equation (2.27) of chapter 2, section 2.5.3). This Hamiltonian contains two terms which are of relevance. The first term gives rise to the Faraday effect and represents a QND measurement. This means that the atomic spins' precession is unaffected by the probe beam and subsequent interrogations will give the same result. The second term contains an alignment tensor which disturbs the atomic state. The strength of the coupling between the probe beam and the atoms determines the relative magnitude between the two terms: (1) probing in the limit where the tensor term is negligible, for example, at lower intensities or probe detunings far greater then the hyperfine frequency separation of the excited state or (2) probing in the limit where the tensor term is magnified, for example, at lower detunings or higher intensities. The effect that the detuning has on this relative magnitude will be examined.

The second category is called the absorptive regime. Here, photons from the probe beam resonantly excite the Zeeman coherences of the ground state, destroying the atoms' precessional frequency. This results in quantum demolitional probing where the probe influences the recorded measurement, and in this chapter, this behaviour will be explored.

5.2 The rf Spectrum

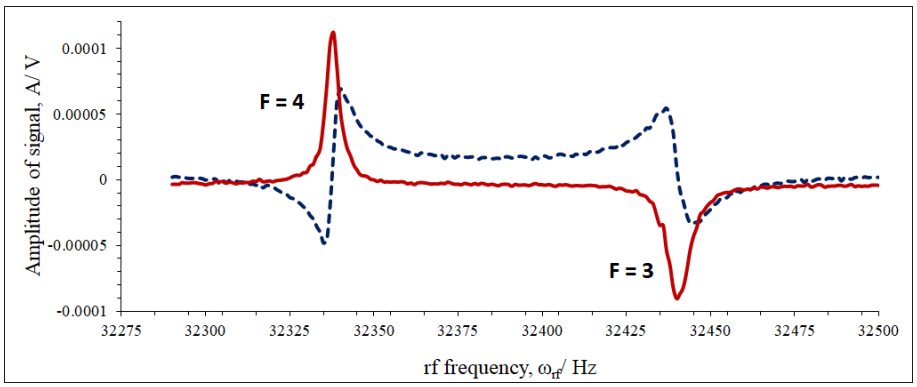

Figure 5.1: rf spectrum showing the magnetometer signals of the $F = 4$ and $F = 3$ ground states in the presence of a small magnetic field. The linear Zeeman effect results in the observation of one transition frequency in a particular ground state because the energy difference between sublevels is equal. The red solid line shows the in-phase component while the blue dashed line shows the out-of-phase component. The spectrum was recorded with $\boldsymbol{B}_0 = 9.3\ \mu$T which results in a 104 Hz difference between the two signals. The measurement was recorded with a probe beam power of 500 μW and a pump beam power of 30 μW.

Figure 5.1 shows the typical polarisation rotation signals of the $F = 4$ and $F = 3$ ground states measured as a function of the rf field frequency. The spectrum was obtained by following the method described in chapter 4, section 4.1. Solid red and dashed blue lines represent the in-phase and out-of-phase signal components recorded by the lock-in amplifier, respectively. The two components differ in phase by 90°. The polarisation rotation resonances are observed because the rf field frequency matches the splitting of the Zeeman sublevels introduced by $\boldsymbol{B}_0$. To be able to monitor the signals created by the coherences of both the $F = 3$ and $F = 4$ ground state levels, a relatively low pump power of 30 μW was used. This power ensures that orientation is produced in both ground state levels, but prevents excessive transfer between them. The amplitudes of the resonances depend on the strength of the coherences created by $\boldsymbol{B}_{rf}$. The linewidths of the rf spectrum profiles are governed by the lifetime of the coherences between ground state magnetic sublevels.

A low $\boldsymbol{B}_0$ was chosen because:

1. The position of the resonance is characterised by the energy difference be-

tween magnetic sublevels. At magnetic fields higher than 70 μT ($\nu_L \approx 245$ kHz), the signal is split into several components due to the non-linear Zeeman effect. Each component corresponds to the coherence amplitude between two adjacent sublevels. For the work described in this chapter, it is sufficient to only consider the total coherence amplitude of a ground state level; what happens between sublevels is of no interest. Therefore, in the presence of the low $\boldsymbol{B}_0$ value (9.3 μT), the linear Zeeman effect is observed and the frequency of all the transitions in a particular manifold are equal, hence, only one resonance peak is observed.

2. As already mentioned in Chapter 2 section 2.2, the hyperfine interaction arises from the coupling between I and J to give the total atomic spin as $F = I \pm J$. Thus, the ground state is split into two levels, $F = 3$ and $F = 4$. The Landé g-factors, g_F, corresponding to these two ground state hyperfine components differ only by the nuclear moments, μ_I:

$$g_{F=I\pm\frac{1}{2}} = \frac{1}{\mu_B}\left(-\frac{\mu_I}{I} \pm \frac{-\frac{\mu_J}{J} + -\frac{\mu_I}{I}}{2I+1}\right). \tag{5.1}$$

$g_{F=4} = 0.250390$ for $F = 4$ and $g_{F=3} = -0.251194$ for $F = 3$ [50, 59], where the measured nuclear moment is $\mu_I = -2.582025(4)\mu_B$ [55] and the magnetic moment of an s-electron ($L = 0$) is $\mu_J = 1.001159652(41)\mu_B$ [56]. The difference in g-factors of these two levels results in the resonances of the ground states being detected at different rf frequencies. For $\boldsymbol{B}_0 = 9.3\ \mu T$, the difference in resonance frequencies between the $F = 4$ and $F = 3$ ground states is 104 Hz.

5.3 Results and Discussion

At every probe beam detuning, the rf field was swept and the spectrum was recorded by the lock-in amplifier at two probe powers: 500 μW and 1140 μW. Each recorded rf spectrum then went through a LabVIEW fitting procedure in which each resonance peak was fitted with a Lorentzian profile. This was done to extract

the amplitude and linewidth of the peaks. Figure 5.2 shows the dependence of the magnetometer signal amplitude on the probe beam detuning from the $6^2S_{\frac{1}{2}}F = 3 \rightarrow 6^2P_{\frac{3}{2}}F' = 2$ transition while Figure 5.3 shows the dependence of the linewidth of the signal on the probe beam detuning from the $6^2S_{\frac{1}{2}}F = 3 \rightarrow 6^2P_{\frac{3}{2}}F' = 2$ transition.

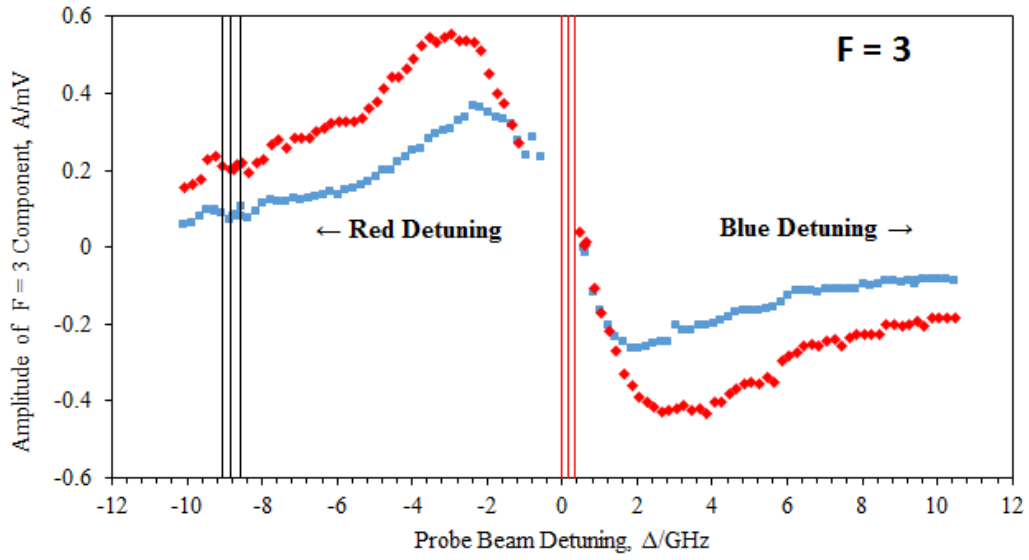

(a)

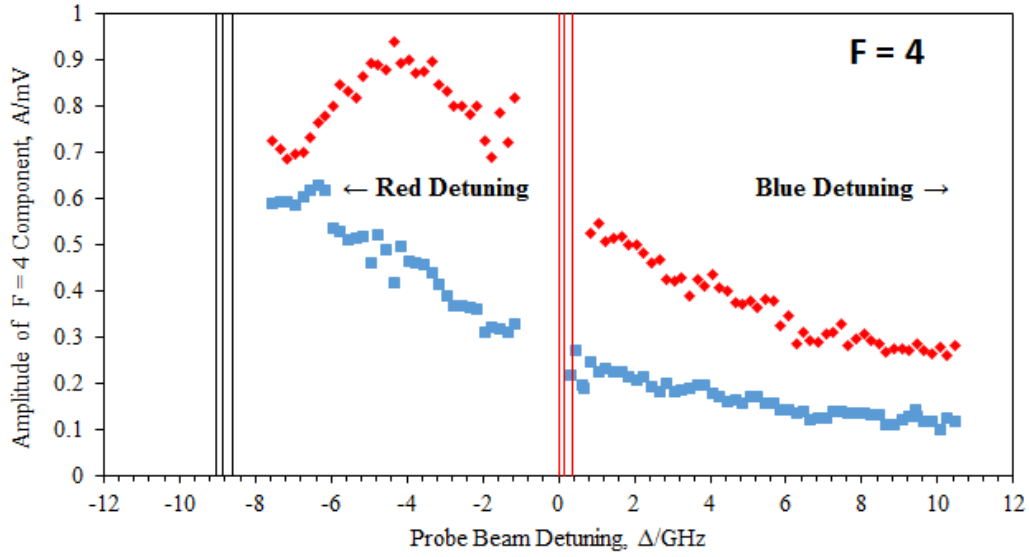

(b)

Figure 5.2: Dependence of the polarisation rotation signal amplitude on the probe beam detuning from the $6^2S_{\frac{1}{2}}F=3 \rightarrow 6^2P_{\frac{3}{2}}F'=2$ transition for the $F=3$ (a) and $F=4$ (b) components. On the graphs, the $6^2S_{\frac{1}{2}}F=3 \rightarrow 6^2P_{\frac{3}{2}}F'=2$ transition serves as the reference point and is represented by a detuning of 0 GHz. Measurements were done at two probe beam powers: 500 μW (blue squares) and 1140 μW (red diamonds), and pump power of 30 μW. The red vertical lines denote the separation between the $6^2S_{\frac{1}{2}}F=3 \rightarrow 6^2P_{\frac{3}{2}}F'=2,3,4$ transitions. The black vertical lines denote the separation between the $6^2S_{\frac{1}{2}}F=4 \rightarrow 6^2P_{\frac{3}{2}}F'=3,4,5$ transitions. The results show the presence of three detuning regimes: an off-resonant and 2 absorptive regimes. The off-resonant regime is characterised by the dispersive dependence of the $F=3$ and $F=4$ signal amplitudes on the probe beam detuning. The two absorptive regimes occur in the regions near 0 GHz and 9 GHz, as a result of vanishing dispersion.

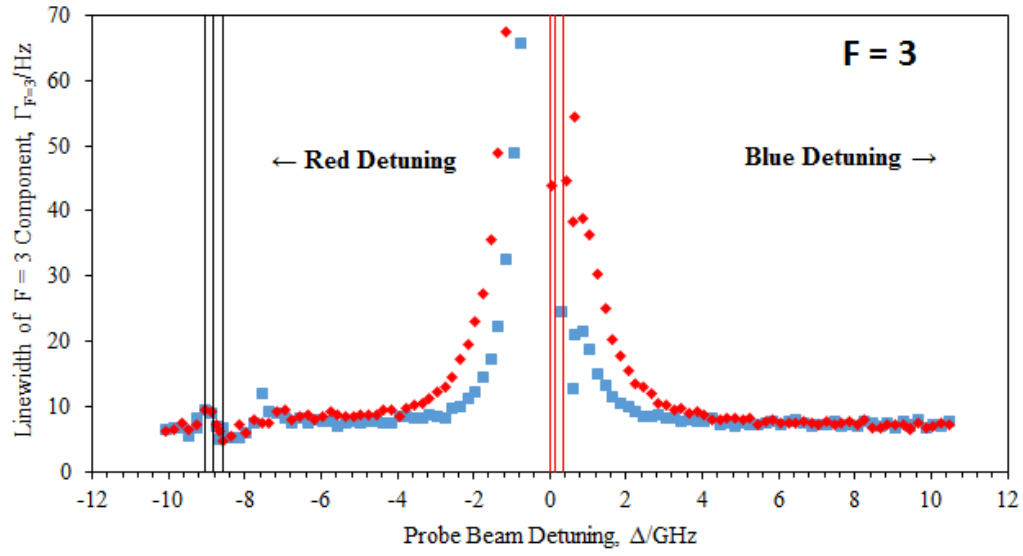

(a)

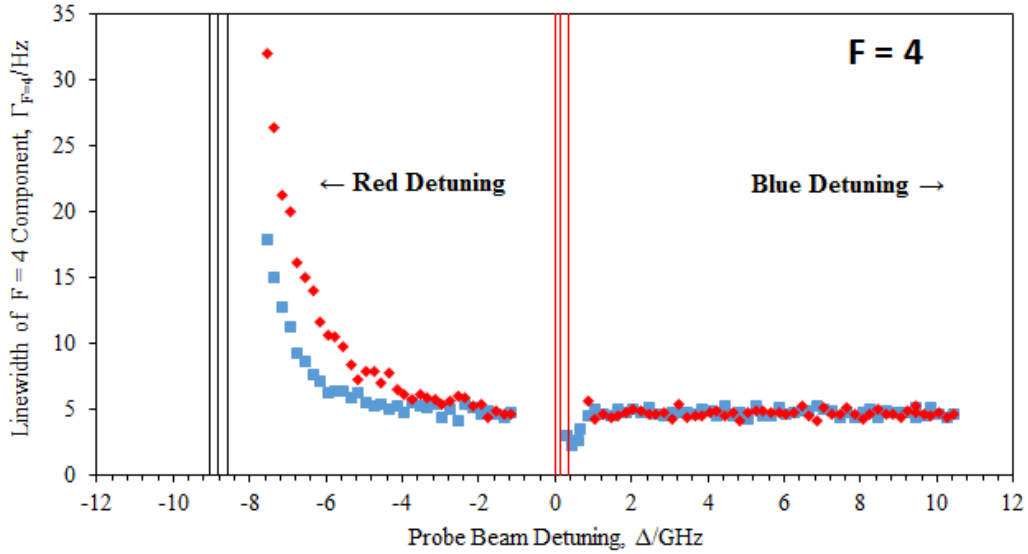

(b)

Figure 5.3: Dependence of the magnetometer signal linewidth on the probe beam detuning from the $6^2S_{\frac{1}{2}}F = 3 \rightarrow 6^2P_{\frac{3}{2}}F' = 2$ transition for the (a) $F = 3$ and (b) $F = 4$ components. On the graph, the $6^2S_{\frac{1}{2}}F = 3 \rightarrow 6^2P_{\frac{3}{2}}F' = 2$ transition serves as the reference point and is represented by a detuning of 0 GHz. Measurements were done at two probe beam powers: 500 μW (blue squares) and 1140 μW (red diamonds), and pump power of 30 μW. The red vertical lines denote the separation between the $6^2S_{\frac{1}{2}}F = 3 \rightarrow 6^2P_{\frac{3}{2}}F' = 2,3,4$ transitions. The black vertical lines denote the separation between the $6^2S_{\frac{1}{2}}F = 4 \rightarrow 6^2P_{\frac{3}{2}}F' = 3,4,5$ transitions. Pure off-resonance frequency range of the probe beam is defined where the linewidth of the magnetometer signal does not change with detuning. It is observed that the linewidth does not change when the probe beam is red or blue detuned by an amount greater than 4000 MHz from the $6^2S_{\frac{1}{2}}F = 3 \rightarrow 6^2P_{\frac{3}{2}}F' = 2$ transition.

In Figure 5.2 (a), it is observed that for the detunings around 0 GHz, the $F = 3$ component significantly departs from a Lorentzian profile. Similarly, in Figure 5.2 (b), the $F = 4$ component at detunings 0 GHz and 9 GHz can no longer be described as Lorentzian. These observations reveal the presence of three detuning regimes: the off-resonant regime and two absorptive regimes.

5.3.1 Off-Resonant Regime

From Figure 5.2, it is observed that the off-resonant regime is characterised by the dispersive dependence of the $F = 3$ and $F = 4$ signal amplitudes on the probe beam detuning. The width of the dispersive frequency dependence on the signal amplitude increases with probe power.

Pure off-resonance frequency range of the probe beam is defined where the linewidth of the magnetometer signal does not change with detuning. From Figure 5.3, it is observed that the linewidth does not change when the probe beam is red or blue detuned by an amount greater than 4000 MHz from the $6^2S_{\frac{1}{2}}F = 3 \rightarrow 6^2P_{\frac{3}{2}}F' = 2$ transition. So, it is indicated that for detunings greater than 4000 MHz, the probe beam falls within the QND region and will not affect the measurement.

Now, for detunings smaller than 4000 MHz, one reason for the broadening of the $F = 3$ component is due to the tensor light shift which occurs for red detunings between 750 MHz to 1150 MHz from the $6^2S_{\frac{1}{2}}F = 3 \rightarrow 6^2P_{\frac{3}{2}}F' = 2$ transition. As the frequency of the probe beam is close to the frequency of transitions involving the $F = 3$ ground state, there is a strong coupling between the probe beam and atomic spins. This means that the second term in the effective Hamiltonian (equation (2.27) of chapter 2) dominates, leading to a splitting of the magnetic sublevels due to unequal energy differences between neighbouring sublevels. The rf spectra recorded for detunings between 750 MHz to 1150 MHz at both probe powers (500 μW and 1140μW), demonstrating the tensor light shift, are shown in Figure 5.4. It is observed that the tensor light shift is stronger at the higher probe powers because the electric field of the probe beam couples very strongly to the atoms. The other reason for the broadening is due to pumping by the probe beam which is discussed in detail in section 5.3.2

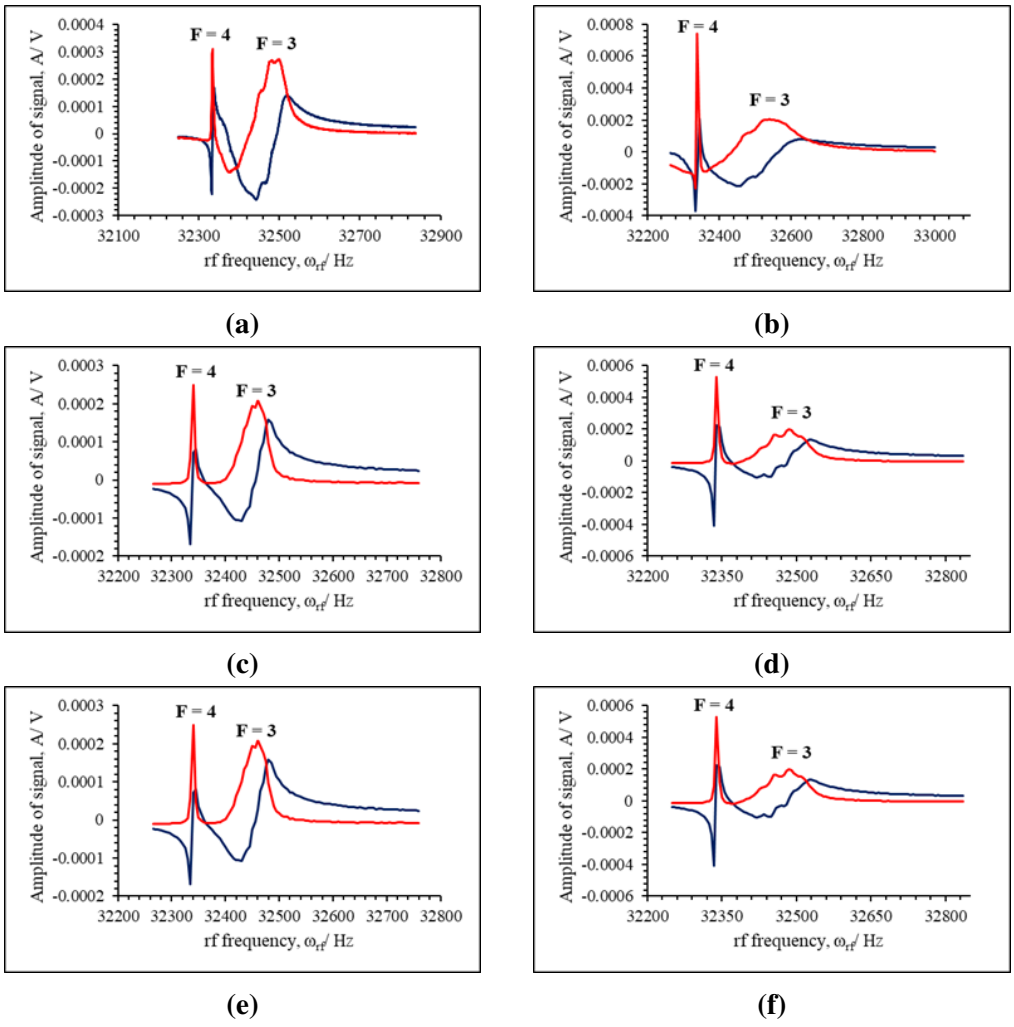

Figure 5.4: rf spectra showing the tensor light shift in the $F = 3$ ground state for red detunings between 750 MHz to 1150 MHz from the $6^2S_{\frac{1}{2}}F = 3 \rightarrow 6^2P_{\frac{3}{2}}F' = 2$ transition. Like Figure 5.1, the red solid line in each spectrum shows the in-phase component while the blue solid line shows the out-of-phase component. (a) and (b) correspond to a detuning of 750 MHz at probe powers 500 μW and 1140 μW, respectively. (c) and (d) correspond to a detuning of 950 MHz at probe powers 500 μW and 1140 μW, respectively. (e) and (f) correspond to a detuning of 1150 MHz at probe powers 500 μW and 1140 μW, respectively. It can be seen that the tensor light shift is most pronounced at the higher probe power (1140 μW) as the splitting in the $F = 3$ ground state is more pronounced in Figures (b), (d) and (f).

5.3.2 Absorptive Regimes

Here, the focus is on describing the interaction between the atomic spins and the probe beam which has a frequency tuned very close to the resonant atomic transitions. Absorptive effects can no longer be ignored as photons from the probe beam

will be absorbed by the atoms, destroying the Zeeman coherences of the ground states. These absorptive effects can be inferred through polarisation rotation of the probe beam because the polarisation rotation angle has a frequency dependence as shown by equation (2.40) in chapter 2, section 2.5.3.

Chapter 2, section 2.2.1, mentioned that the experiments are carried out with Cs atomic vapour at room temperature. The Doppler broadening width of atomic transitions due to the atoms moving at this temperature is:

$$\Delta\nu_D = 2\frac{\nu_0}{c}\sqrt{\frac{2k_BTln2}{m_{Cs}}} = 200\,\text{MHz}. \tag{5.2}$$

where ν_0 is the resonant frequency, k_B is the Boltzmann constant, m_{Cs} is the atomic mass of Cs and T is the room temperature which is taken to be 295.15 K (22°C). Because the Doppler width is 200 MHz, the hyperfine structure is partially resolved while the ground state is fully resolved due to the 9192 MHz detuning between the $F = 3$ and $F = 4$ states.

To gain an insight into what happens in this region, Skalla et al. [152] demonstrated that the complex Cs level scheme can be reduced to a six-level model system. This model is not perfect in describing the results presented in this section but it is included because it is useful in helping to understand the results. A more concrete model for describing the results is currently being devised.

In the six-level model system by Skalla et al. [152], each ground state multiplet ($F = 3$ and $F = 4$) is modelled by a spin-$\frac{1}{2}$ system with $m_J = \pm 1$, where m_J describes the projection of the total electron angular momentum onto the quantisation axis. They are connected to a single excited state doublet with $m'_J = \pm 1$ because the hyperfine splitting is not well resolved due to Doppler broadening. The model works with the assumptions that there is no spectral overlap between the two ground state hyperfine components and the intensity of the pump beam does not saturate the optical transitions so the transitions from the two ground states to the excited state multiplet may be treated separately, therefore, the six-level system is split into two four-level systems as depicted in Figure 5.5.

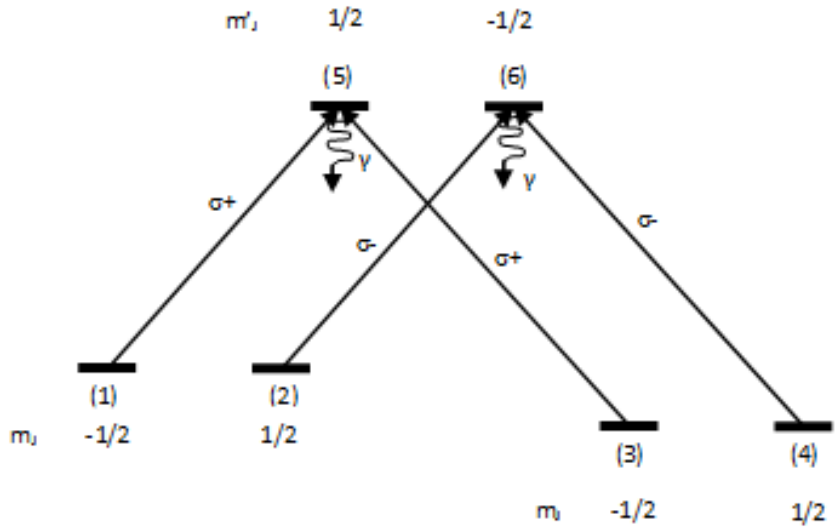

Figure 5.5: Simplified six-level scheme of Cs to explain what happens in the absorptive regime. Levels (1,2) and (3,4) represent the two ground state hyperfine multiplets, $F = 4$ and $F = 3$, respectively. The excited state is assumed to be unresolved due to Doppler broadening and is modelled as a single doublet (5,6). Optical excitation occurs from both ground states multiplets.

The Hamiltonian which describes the relevant interaction between the atom and the electrical field component of the probe beam, $\boldsymbol{E}$, propagating along the z-direction, and the static magnetic field, $\boldsymbol{B}_0$, oriented along the x-axis is given by:

$$\hat{H} = \hat{H}_0 - \boldsymbol{\mu}_E.\boldsymbol{E} - \boldsymbol{\mu}_m.\boldsymbol{B}_0. \tag{5.3}$$

where $\hat{H}_0$ is the Hamiltonian of the atomic system without external fields, $\boldsymbol{\mu}_E$ is the electric transition dipole moment of the atom and $\boldsymbol{\mu}_m$ is the magnetic dipole moment of the atom. The quantisation axis is the direction of propagation of the light beam, that is, the z-axis. $-\boldsymbol{\mu}_E.\boldsymbol{E}$ couples the levels 1 and 5, 3 and 5 (σ_+ light), and 2 and 6, 4 and 6 (σ_- light) to produce the the optical coherences, $\rho_{15}, \rho_{35}, \rho_{26}$ and ρ_{46}. $-\boldsymbol{\mu}_m.\boldsymbol{B}_0$ couples levels 1 and 2, 3 and 4, and 5 and 6 to give rise to the Zeeman coherences, ρ_{12}, ρ_{34} and ρ_{56}. The simultaneous presence of $\boldsymbol{E}$ and $\boldsymbol{B}_0$ creates coherences between levels 1 and 6, 2 and 5, 3 and 6, and 4 and 5.

The electric field, $\bar{\boldsymbol{E}}(z,t)$, propagating along the z-direction, can be written as

a monochromatic plane wave using the standard spherical basis:

$$\boldsymbol{E}(z,t) = \frac{1}{2}\sum_q (-1)^q E_q(z)\hat{e}_{-q}\exp(i\omega t) + c.c. \tag{5.4}$$

where $\hat{e}_\pm = \mp^{(\hat{e}_x + i\hat{e}_y)}/\sqrt{2}$ and $\hat{e}_0 = \hat{e}_z$, and $c.c$ represents the complex conjugate. Here, $E_+(E_-)$ is the electric field amplitude of the $\sigma_+(\sigma_-)$ polarised components of the probe beam and $E_0 = 0$.

The optical polarisation of the medium is given by:

$$\boldsymbol{P}(z,t) = \frac{1}{2}\sum_q (-1)^q P_q\hat{e}_{-q}\exp(i\omega t) + c.c = n_{atoms}Tr(\boldsymbol{\mu}_E\rho). \tag{5.5}$$

where n_{atoms} denotes the atomic number density. When equation (5.5) is compared with the expression, $P_\pm = \varepsilon_0\chi_\pm E_\pm$, it is seen that the macroscopic susceptibility of the medium is related to the microscopic density matrix of the system. The evolution of the density matrix is given by the Liouville equation:

$$\dot{\rho} = \frac{1}{i\hbar}[\hat{H},\rho] - \hat{\Gamma}\rho. \tag{5.6}$$

where $\hat{\Gamma}$ is a relaxation operator introduced phenomenologically to describe all relaxation processes [153]. For the decay of the optical coherences, a single decay rate, γ_d, will be assumed.

Several simplifying assumptions can be made in order to solve equation (5.6) [154]. The relaxation of the optical coherences ρ_{15}, ρ_{26}, ρ_{35}, ρ_{46}, ρ_{16}, ρ_{36}, ρ_{25}, and ρ_{45} is assumed to be fast with respect to all changes of field amplitudes, thus these quantities can be adiabatically eliminated. The procedure for adiabatic elimination is to set the time derivatives of the optical coherences to 0 in the Liouville equation because, though the optical coherences fluctuate, their mean values will be those of the steady state [72]. Thus, using the adiabatic approximation means that the equations are valid over timescales long enough that the fluctuations can be averaged [72]. The population of the excited state and the Zeeman coherence within this state are neglected. The ground state Larmor frequency, ω_L, is assumed to be small

compared to the optical linewidth, γ_d, that is, $\omega_L << \gamma_d$. The Zeeman coherence and the population densities in the ground state are assumed to decay with equal time constants to their equilibrium values. With these simplifications, the equations of motion for the density matrix can be found [154].

Consequently, the polarisation components, $P_{\pm}$, for the six-level scheme are given by:

$$P_+ = 2N(\frac{\Omega_{51}^+}{\Delta_{51}+i\gamma_d}\rho_{11} + \frac{\Omega_{53}^+}{\Delta_{53}+i\gamma_d}\rho_{33}), \tag{5.7}$$

$$P_- = 2N(\frac{\Omega_{62}^+}{\Delta_{62}+i\gamma_d}\rho_{22} + \frac{\Omega_{64}^+}{\Delta_{64}+i\gamma_d}\rho_{44}). \tag{5.8}$$

where $\Omega_{ij} = \mu_{E_{ij}}E_{\pm}/2\hbar$ is the electric dipole coupling strength and $\Delta_{ij} = \omega - \omega_{ij}$ is the detuning of the laser frequency, ω, from the transition frequency, ω_{ij}, of the $i \rightarrow j$ transition.

The population in the ground state levels ($i = 1,2,3,4$) in the laboratory frame are described by the density matrix elements, ρ_{ii}, whereby the quantisation axis is defined as being in the direction of the probe beam (z-axis), which is transverse to $\boldsymbol{B}_0$. The diagonal matrix elements, ρ_{11}, ρ_{22}, ρ_{33} and ρ_{44}, are obtained by determining the action of the rf pulse, in the y-direction, on the density matrix, $\rho^{(0)}$. $\rho^{(0)}$ describes the initial situation after optical pumping of the longitudinal magnetisation along the x-axis. These matrix elements are found to be:

$$\rho_{11} = \frac{1}{2}(\rho_{11}^{(0)} + \rho_{22}^{(0)}) + \frac{1}{2}(\rho_{22}^{(0)} - \rho_{11}^{(0)})cos(\omega_{L_1}t), \tag{5.9}$$

$$\rho_{22} = \frac{1}{2}(\rho_{11}^{(0)} + \rho_{22}^{(0)}) - \frac{1}{2}(\rho_{22}^{(0)} - \rho_{11}^{(0)})cos(\omega_{L_1}t), \tag{5.10}$$

$$\rho_{33} = \frac{1}{2}(\rho_{33}^{(0)} + \rho_{44}^{(0)}) + \frac{1}{2}(\rho_{44}^{(0)} - \rho_{33}^{(0)})cos(\omega_{L_2}t - \pi), \tag{5.11}$$

$$\rho_{44} = \frac{1}{2}(\rho_{33}^{(0)} + \rho_{44}^{(0)}) - \frac{1}{2}(\rho_{44}^{(0)} - \rho_{33}^{(0)})cos(\omega_{L_2}t - \pi). \tag{5.12}$$

where ω_{L_1} is the Larmor frequency for transition $i \rightarrow j$ of the (1,2) subsystem ($F = 4$ ground state) and ω_{L_2} is the Larmor frequency for transition $i \rightarrow j$ of the (3,4) subsystem ($F = 3$ ground state). The phase shift of π in equations (5.11) and (5.12) is due to the different sign of g_F of the $F = 3$ ground state.

For a dilute sample, the refractive index, n, is related to the susceptibility of the medium. Equation (2.36) in chapter 2 section 5.2.2 showed that due to circular birefringence of the medium, the two circular polarisations of the probe beam, $P_{\pm}$, experience a difference in refractive index, $n_{\pm}$. For a dilute sample, $n_{\pm}$, is related to the susceptibility, $\chi_{\pm}$, according to the following equation:

$$n_{\pm} \approx 1 + \frac{1}{2}\mathrm{Re}\chi_{\pm}. \tag{5.13}$$

Therefore, the angle that the polarisation plane of the linearly polarised light is rotated by is:

$$\begin{aligned} \Delta\theta &= \frac{2\pi}{\lambda}(\frac{n_+ - n_-}{2})L = \frac{\omega L}{2c}(n_+ - n_-) \\ &\propto E((\rho_{22}^{(0)} - \rho_{11}^{(0)})\frac{\Delta_{51}}{\Delta_{51}^2 + \gamma_d^2}cos(\omega_{L_1}t) \\ -(\rho_{44}^{(0)} - \rho_{33}^{(0)})&\frac{\Delta_{53}}{\Delta_{53}^2 + \gamma_d^2}cos(\omega_{L_2}t - \pi)). \end{aligned} \tag{5.14}$$

where E is a constant, L is the length of the medium and c is the speed of light.

It is observed that the polarisation rotation angle depends on the population differences, $\rho_{22}^{(0)} - \rho_{11}^{(0)}$ and $\rho_{44}^{(0)} - \rho_{33}^{(0)}$, within each ground state level, along with the optical dispersion parameter, $\frac{\Delta_{ij}}{\Delta_{ij}^2+\gamma_d^2}$. The two circular components of the probe beam excite the coherences of the Zeeman sublevels of the two ground states which changes the polarisation of the medium and give rise to the population difference within the two ground states.

If the probe laser is on resonance with one hyperfine transition, the splitting of the other hyperfine transition is detected. This occurs because the balanced polarimetry technique used relies on dispersive effects. So, on resonance, the dispersion sensitivity is 0 for one hyperfine transition because the dispersion of the medium is 0 at that wavelength, while the other hyperfine transition is detected with some sensitivity corresponding to the dispersion at that resonance offset given by the ground state hyperfine splitting.

Two regions were identified which fall under the absorptive regime. These

two regions are when the probe laser is in the vicinity of either the $6^2S_{\frac{1}{2}}F = 3 \rightarrow 6^2P_{\frac{3}{2}}F' = 2,3,4$ or the $6^2S_{\frac{1}{2}}F = 4 \rightarrow 6^2P_{\frac{3}{2}}F' = 3,4,5$ transitions. In these regions, the coherences between the Zeeman sublevels of the two ground states are resonantly excited by the probe beam.

In the vicinity of the $6^2S_{\frac{1}{2}}F = 3 \rightarrow 6^2P_{\frac{3}{2}}F' = 2,3,4$ transitions, that is, when the probe beam has a red detuning less than 750 MHz and a blue detuning less than 652 MHz from the $6^2S_{\frac{1}{2}}F = 3 \rightarrow 6^2P_{\frac{3}{2}}F' = 2$ transition, it is observed that the signal created by the $F = 3$ atoms vanishes in accordance to the model described earlier, while the amplitude and shape of the $F = 4$ signal profile changes as shown in Figures 5.6 and 5.7 for specific detuning cases.

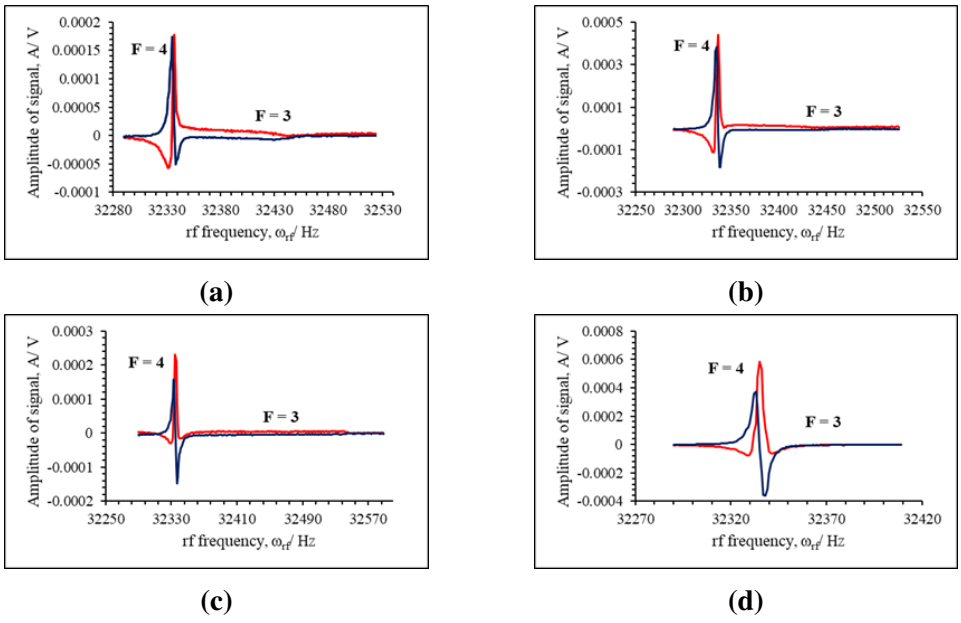

Figure 5.6: rf spectra showing absorption in the $F = 3$ ground state for different **blue** detunings from the $6^2S_{\frac{1}{2}}F = 3 \rightarrow 6^2P_{\frac{3}{2}}F' = 2$ transition. Like Figure 5.1, the red solid line in each spectrum shows the in-phase component while the blue solid line shows the out-of-phase component. (a) and (b) correspond to a detuning of 616 MHz at probe powers 500 μW and 1140 μW, respectively. (c) and (d) correspond to a detuning of 452 MHz at probe powers 500 μW and 1140 μW, respectively. The spectra demonstrate that for detunings less than 652 MHz from the $6^2S_{\frac{1}{2}}F = 3 \rightarrow 6^2P_{\frac{3}{2}}F' = 2$ transition, the signal created by the $F = 3$ atoms vanishes, while the amplitude and shape of the $F = 4$ signal profile changes.

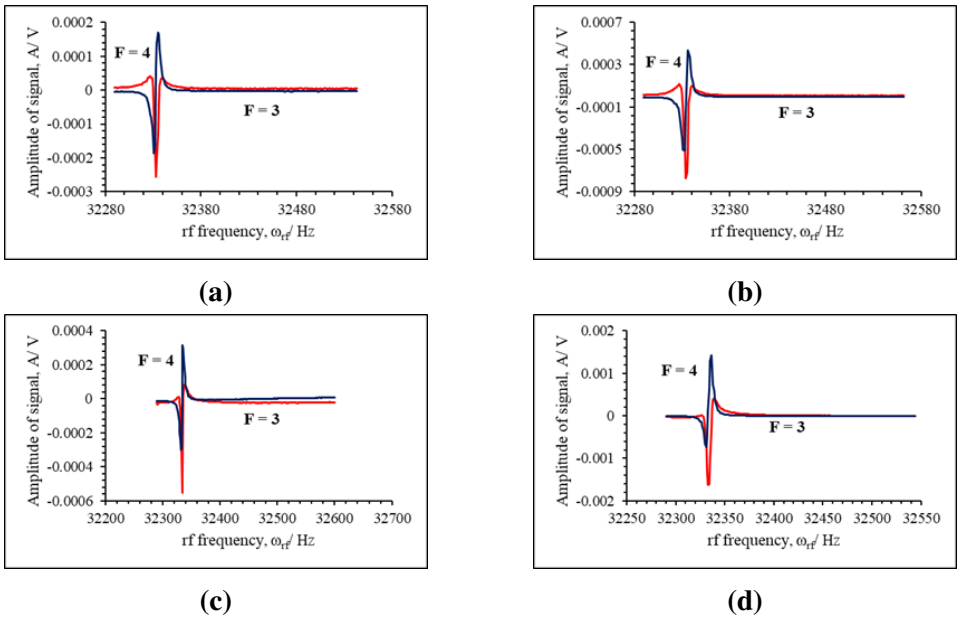

Figure 5.7: rf spectra showing absorption in the $F = 3$ ground state for different **red** detunings from the $6^2S_{\frac{1}{2}}F = 3 \rightarrow 6^2P_{\frac{3}{2}}F' = 2$ transition. Like Figure 5.1, the red solid line in each spectrum shows the in-phase component while the blue solid line shows the out-of-phase component. (a) and (b) correspond to a detuning of 113 MHz at probe powers 500 μW and 1140 μW, respectively. (c) and (d) correspond to a detuning of 349 MHz at probe powers 500 μW and 1140 μW, respectively. The spectra demonstrate that for red detunings less than 750 MHz from the $6^2S_{\frac{1}{2}}F = 3 \rightarrow 6^2P_{\frac{3}{2}}F' = 2$ transition, the signal created by the $F = 3$ atoms vanishes, while the amplitude and shape of the $F = 4$ signal profile changes.

Strong saturation and power broadening of the $F = 3$ ground state by the resonant probe beam causes depletion of the atomic population in this state. The population is transferred to the $F = 4$ ground state by optical pumping. What this means is that the linearly polarised probe beam becomes the leading pumping mechanism because the circularly polarised pump beam is too weak, hence, the probe beam creates its own population imbalance. The change in the sign of the detuning with respect to the $6^2S_{\frac{1}{2}}F = 3 \rightarrow 6^2P_{\frac{3}{2}}F' = 2$ transitions leads to the $F = 4$ signal having opposite sign. Chalupczak et al. [155] observed similar pumping behaviour between ground state manifolds in the rf spectra generated by linearly polarised light tuned to the D1 transition. When the probe beam is detuned slightly from the resonant transitions but still within the absorptive region, the atomic population builds up in both ground states. This is because atoms excited to the $F' = 3$ or $F' = 4$

states can spontaneously decay to either ground state. This behaviour is confirmed by the line strengths of the Cs D2 transitions (Figure 5.8) in which the line strengths of the $F' = 3,4$ states are interconnected with the $F = 3,4$ ground states.

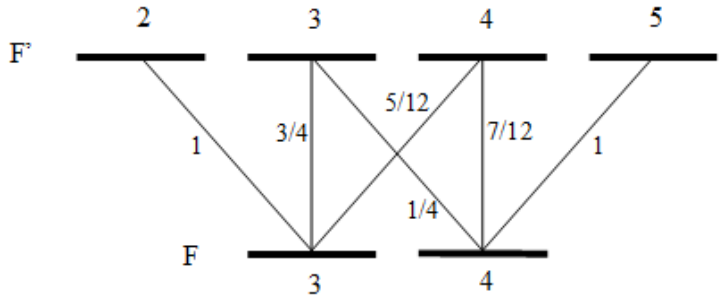

Figure 5.8: Cs D2 line strengths showing the interconnected $F' = 3,4$ and $F = 3,4$ ground states.

Figure 5.9 shows a continuous 3D graph of how the $F = 3$ and $F = 4$ component changes when the probe beam is in the vicinity of the $6^2S_{\frac{1}{2}}F = 3 \rightarrow 6^2P_{\frac{3}{2}}F' = 2,3,4$ transitions.

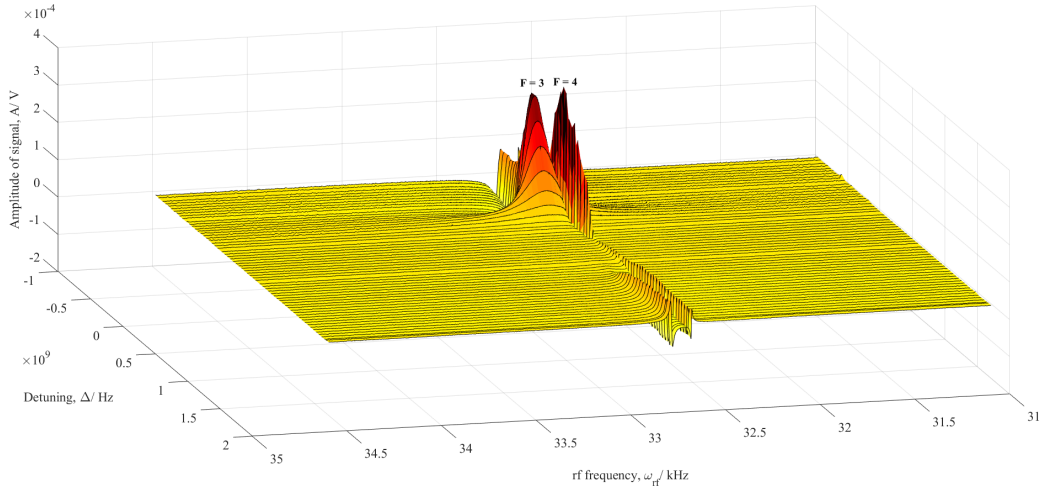

(a)

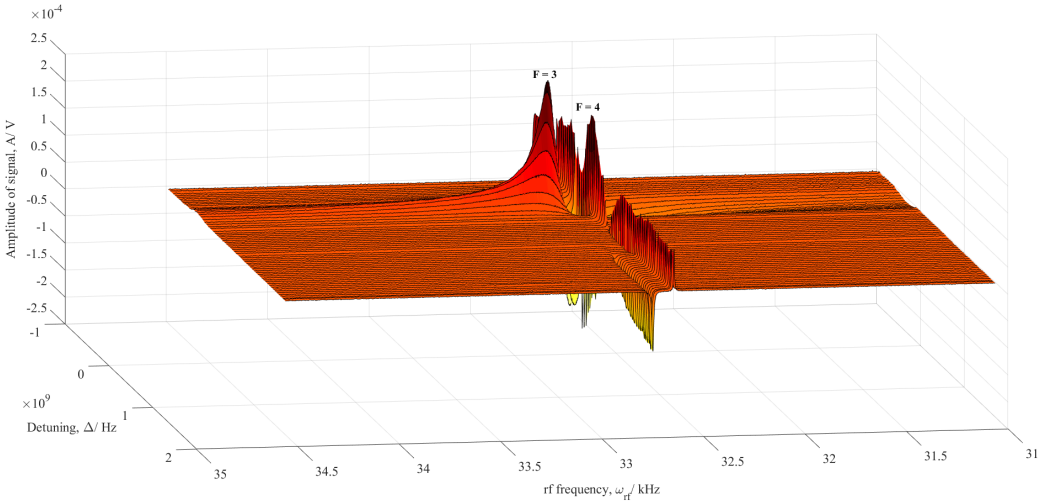

(b)

Figure 5.9: Dependence of the magneto-optical rotation signal amplitude on the probe beam detuning from the $6^2S_{\frac{1}{2}}F = 3 \rightarrow 6^2P_{\frac{3}{2}}F' = 2$ transition (**vicinity of the** $F = 3$ **lines**). Measurements have been done with probe beam power = 500 μW and pump power = 30 μW.

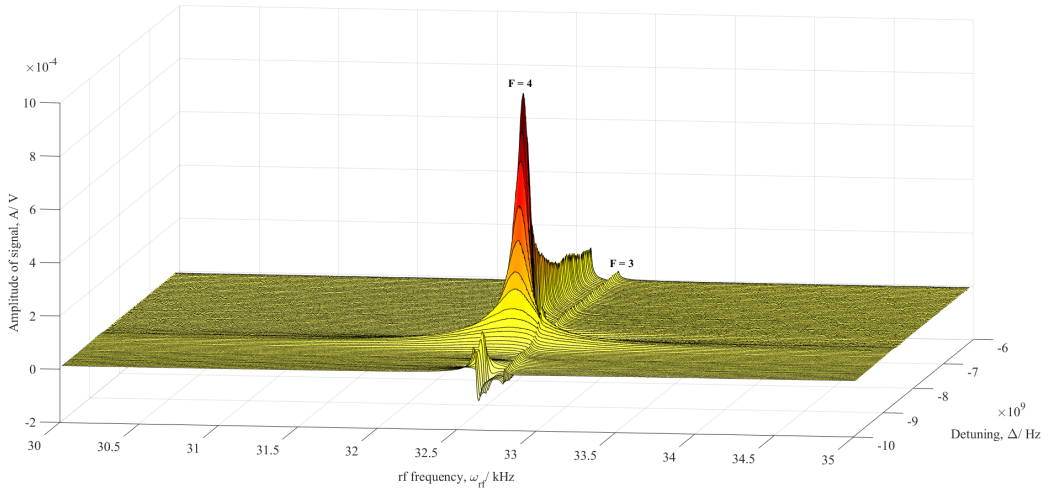

(a)

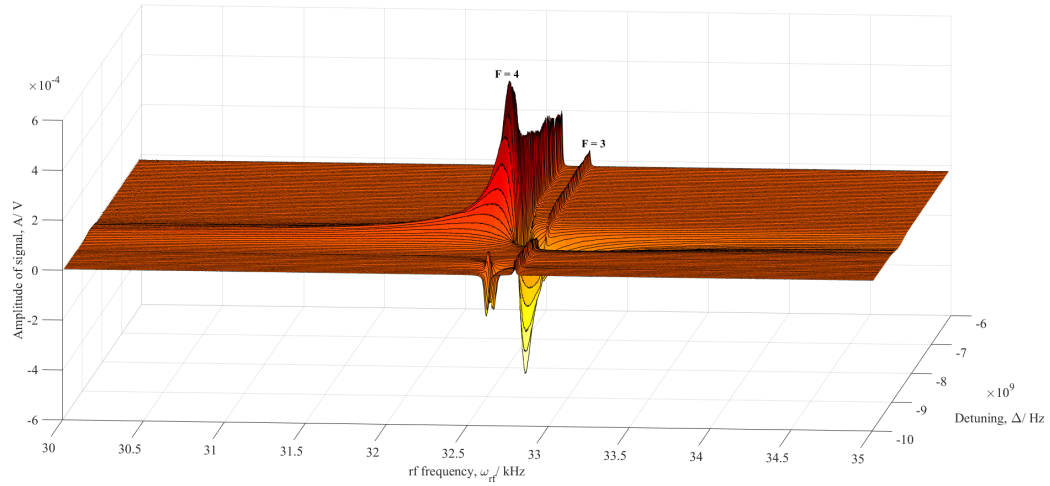

(b)

Figure 5.10: Dependence of the magneto-optical rotation signal amplitude on the probe beam detuning from the $6^2S_{\frac{1}{2}}F = 3 \rightarrow 6^2P_{\frac{3}{2}}F' = 2$ transition (**vicinity of the** $F = 4$ **lines**). Measurements have been done with probe beam power = 500 μW and pump power = 30 μW.

Figure 5.10 illustrates a 3D graph of how the $F = 4$ and $F = 3$ components change when the probe beam is in the vicinity of the $6^2S_{\frac{1}{2}}F = 4 \rightarrow 6^2P_{\frac{3}{2}}F' = 3,4,5$ transitions. This vicinity corresponds to when the probe beam is red detuned $8149 - 10050$ MHz from the $6^2S_{\frac{1}{2}}F = 3 \rightarrow 6^2P_{\frac{3}{2}}F' = 2$ transition. When the probe beam is resonant with the $6^2S_{\frac{1}{2}}F = 4 \rightarrow 6^2P_{\frac{3}{2}}F' = 3,4,5$ transitions, huge power broadening and saturation causes the $F = 4$ component to disappear, then a pronounced maximum or minimum $F = 4$ peak and small $F = 3$ peak are observed, as

demonstrated in Figure 5.10, and for specific detunings in Figures 5.11 and 5.12. These features reveal that there is no transfer of atomic population from the $F = 3$ to $F = 4$ ground state as was observed earlier. Most of the population accumulates in the $F = 4$ ground state with very little in the $F = 3$ ground state. This is due to the fact that most of the atoms excited by the probe beam jump to the $F' = 5$ level. When they decay, they can only return to the the $F = 4$ ground state because the $6^2P_{\frac{3}{2}}F' = 5 \rightarrow 6^2S_{\frac{1}{2}}F = 3$ is a forbidden transition, hence, they populate the $F = 4$ ground state only.

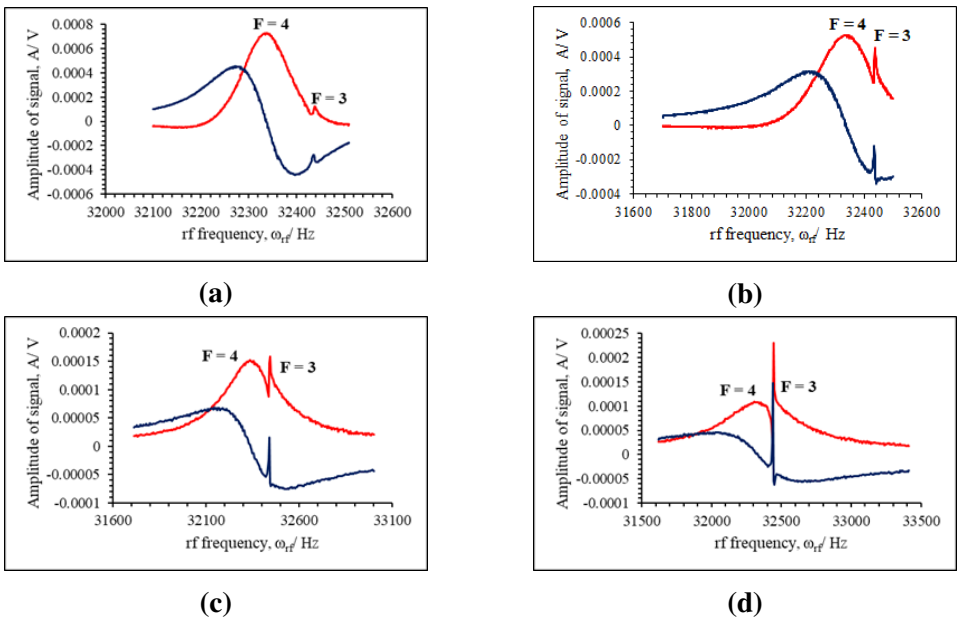

Figure 5.11: rf spectra showing absorption in the $F = 4$ ground state for different **red** detunings from the $6^2S_{\frac{1}{2}}F = 3 \rightarrow 6^2P_{\frac{3}{2}}F' = 2$ transition. Like Figure 5.1, the red solid line in each spectrum shows the in-phase component while the blue solid line shows the out-of-phase component. (a) and (b) correspond to a detuning of 8350 MHz at probe powers 500 μW and 1140 μW, respectively. (c) and (d) correspond to a detuning of 8550 MHz at probe powers 500 μW and 1140 μW, respectively. Note that (a), (b), and (c), (d) correspond to **blue** detunings of 239.5 MHz and 39.5 MHz from the $6^2S_{\frac{1}{2}}F = 4 \rightarrow 6^2P_{\frac{3}{2}}F' = 5$ transition, respectively. The rf spectra illustrate that the $F = 3$ ground state does not change shape so there is no transfer of atomic population between the $F = 3$ and $F = 4$ ground states. Most of the population accumulates in the $F = 4$ ground state. This is due to the fact that most of the atoms excited by the probe beam jump to the $F' = 5$ level. When they decay, they can only return to the the $F = 4$ ground state because the $6^2P_{\frac{3}{2}}F' = 5 \rightarrow 6^2S_{\frac{1}{2}}F = 3$ is a forbidden transition. Hence, they populate the $F = 4$ ground state only.

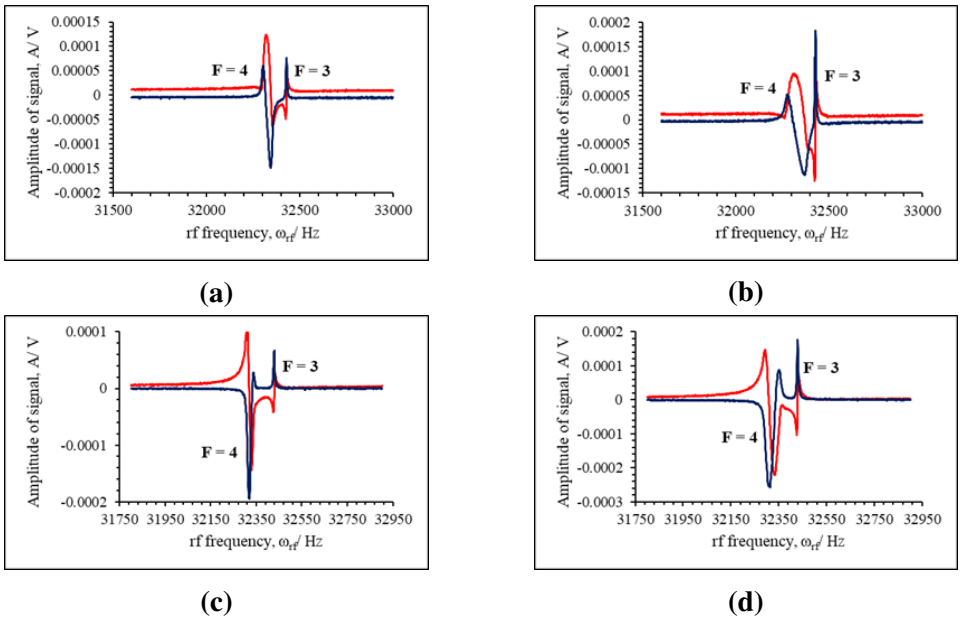

Figure 5.12: rf spectra showing absorption in the $F = 4$ ground state for different **red** detunings from the $6^2S_{\frac{1}{2}}F = 3 \rightarrow 6^2P_{\frac{3}{2}}F' = 2$ transition. Like Figure 5.1, the red solid line in each spectrum shows the in-phase component while the blue solid line shows the out-of-phase component. (a) and (b) correspond to a detuning of 9650 MHz at probe powers 500 μW and 1140 μW respectively. (c) and(d) correspond to a detuning of 10050 MHz at probe powers 500 μW and 1140 μW, respectively. Note that (a), (b), and (c), (d) correspond to **red** detunings of 157 MHz and 556.6 MHz from the $6^2S_{\frac{1}{2}}F = 4 \rightarrow 6^2P_{\frac{3}{2}}F' = 5$ transition, respectively. The rf spectra illustrate that the $F = 3$ ground state does not change shape so there is no transfer of atomic population between the $F = 3$ and $F = 4$ ground states. Most of the population accumulates in the $F = 4$ ground state. This is due to the fact that most of the atoms excited by the probe beam jump to the $F' = 5$ level. When they decay, they can only return to the the $F = 4$ ground state because the $6^2P_{\frac{3}{2}}F' = 5 \rightarrow 6^2S_{\frac{1}{2}}F = 3$ is a forbidden transition. Hence, they populate the $F = 4$ ground state only.

5.4 Summary of Important Results

This chapter has investigated the effect of the probe beam detuning on the atomic magnetometer signal. Three detuning regimes were observed.

The first regime, the off-resonant regime, was characterised by the dispersive dependence of the $F = 3$ and $F = 4$ signal amplitudes on the probe beam detuning. The linewidth of the magnetometer signal did not change when the probe is red or blue detuned by an amount greater than 4000 MHz from the $6^2S_{\frac{1}{2}}F = 3 \rightarrow 6^2P_{\frac{3}{2}}F' = 2$ transition, indicating that the probe falls within the QND regime. For detunings

smaller than 4000 MHz in the $F = 3$ ground state, the two terms in the effective Hamiltonian (chapter 2, section 2.5.3, equation (2.27)) begin to compete with each other with the tensor light shift dominating and leading to a splitting of the magnetic sublevels for red detunings between 750 MHz to 1150 MHz.

There are two absorptive regimes. These are when the probe beam is tuned in the vicinity of either the $6^2S_{\frac{1}{2}}F = 3 \rightarrow 6^2P_{\frac{3}{2}}F' = 2,3,4$ or $6^2S_{\frac{1}{2}}F = 4 \rightarrow 6^2P_{\frac{3}{2}}F' = 3,4,5$ transitions.

In the vicinity of the $6^2S_{\frac{1}{2}}F = 3 \rightarrow 6^2P_{\frac{3}{2}}F' = 2,3,4$ transitions, (probe beam is red detuned less than 750 MHz and blue detuned less than 652 MHz from the $6^2S_{\frac{1}{2}}F = 3 \rightarrow 6^2P_{\frac{3}{2}}F' = 2$ transition), the signal from the $F = 3$ component vanishes while the amplitude and shape of the $F = 4$ signal profile changes. This occurs because the linearly polarised probe beam becomes the leading pumping mechanism and transfers atoms from the $F = 3$ ground state to the $F = 4$ ground state.

When the probe beam is in the vicinity of the $6^2S_{\frac{1}{2}}F = 4 \rightarrow 6^2P_{\frac{3}{2}}F' = 3,4,5$ transitions (probe beam is red detuned $8149 - 10050$ MHz from the $6^2S_{\frac{1}{2}}F = 3 \rightarrow 6^2P_{\frac{3}{2}}F' = 2$ transition), a pronounced $F = 4$ peak and a small $F = 3$ peak are observed. This reveals that most of the population is found in the $F = 4$ ground state with very little in the $F = 3$ ground state. This signifies that most of the atoms excited by the probe beam jump to the $F' = 5$ level. Because the $6^2P_{\frac{3}{2}}F' = 5 \rightarrow 6^2S_{\frac{1}{2}}F = 3$ is a forbidden transition, these atoms can only spontaneously decay to the $F = 4$ ground state.

Chapter 6

Determining the Sensitivity of the Magnetometer

6.1 Introduction

In this chapter, the sensitivity of the rf atomic magnetometer is evaluated. As mentioned in chapter 3, section 3.3, the sensitivity is defined as either the smallest change in the magnetic field able to be detected or it is the smallest detectable magnetic field. Here, the focus is on finding the smallest magnetic field using the $F = 4$ ground state. This is because the indirect pumping technique discussed in chapter 2, section 2.5.1.1 is used, in which the master laser is locked to one of the transitions involving the $F = 3$ ground state. Through off-resonant pumping and SEC, orientation builds up in the $F = 4$ ground state. This will improve the sensitivity of the atomic magnetometer by addressing simultaneously two points: (1) depletion of the $F = 3$ ground state will enable more atoms to contribute to the amplitude of the measured signal and (2) a high degree of orientation will be created in the $F = 4$ ground state, which leads to narrowing of the largest rf resonances and improved signal to noise ratio.

The static magnetic field in the x-direction, $\boldsymbol{B}_0$, is used to tune the Zeeman sublevels of the $F = 4$ ground state in resonance with the weak oscillating rf magnetic field, $\boldsymbol{B}_{rf}$. Orientation within the $F = 4$ ground state is achieved by indirectly pumping atoms into the stretched state. This generates a longitudinal macroscopic

polarisation component along the static magnetic field, which serves as the quantisation axis. $\boldsymbol{B}_{rf}$, applied in the y-direction, alters the anisotropy of the atomic medium by producing a transverse magnetisation component which precesses about $\boldsymbol{B}_0$. The atomic coherence evolution in the magnetic field is monitored by the linearly polarised probe beam propagating orthogonally to the longitudinal macroscopic polarisation by utilising the Faraday effect in which the atomic spin is mapped onto the probe beam.

This chapter is divided into two parts. The first part investigates how the sensitivity of the magnetometer is determined at a probe beam detuning of 4740 MHz from the $6^2S_{\frac{1}{2}}F = 4 \rightarrow 6^2P_{\frac{3}{2}}F' = 5$ transition. The second part examines the relationship between the SNR and the probe beam detuning. Four detunings of the probe beam from the $6^2S_{\frac{1}{2}}F = 4 \rightarrow 6^2P_{\frac{3}{2}}F' = 5$ transition are explored.

6.2 Determining the rf magnetometer sensitivity

6.2.1 The rf Spectrum

The static magnetic field, $\boldsymbol{B}_0$, used was 141 μT which corresponds to $\omega_L \approx 493$ kHz. In such a field, the non-linear Zeeman effect lifts the degeneracy between sublevels. This leads to non-equal energy differences between the adjacent magnetic sublevels because the energy spacings grow quadratically with the field. Consequently, the Zeeman coherences between neighbouring sublevels are well separated, resulting in the observation of several different rf transition frequencies. The separation between the components is 53 Hz, according to equation (2.8) in chapter 2, section 2.2.1.

This magnetic field was chosen because it enables selective monitoring of the individual rf resonances between neighbouring $F = 4$ Zeeman sublevels. The master laser which generated the pump beam was locked to the $6^2S_{\frac{1}{2}}F = 3 \rightarrow 6^2P_{\frac{3}{2}}F' = 3$ transition and the slave laser which produced the probe was red detuned from that transition by 4000 MHz. This means that the slave was 5192 MHz from the $6^2S_{\frac{1}{2}}F = 4 \rightarrow 6^2P_{\frac{3}{2}}F' = 3$ transition, which itself is 452 MHz from the $6^2S_{\frac{1}{2}}F = 4 \rightarrow 6^2P_{\frac{3}{2}}F' = 5$ transition. Hence, the slave was detuned by 4740 MHz

from the $6^2S_{\frac{1}{2}}F = 4 \rightarrow 6^2P_{\frac{3}{2}}F' = 5$ transition. The circularly polarised (σ^+) pump beam polarised the atomic vapour using the indirect pumping technique. The frequency of $\boldsymbol{B}_{rf}$ was swept and the signal was demodulated by the lock-in amplifier. Sweeping the $\boldsymbol{B}_{rf}$ frequency allows a spectrum of eight peaks to be recorded. Figure 6.1 shows a typical rf spectrum acquired in the presence of $\boldsymbol{B}_0$.

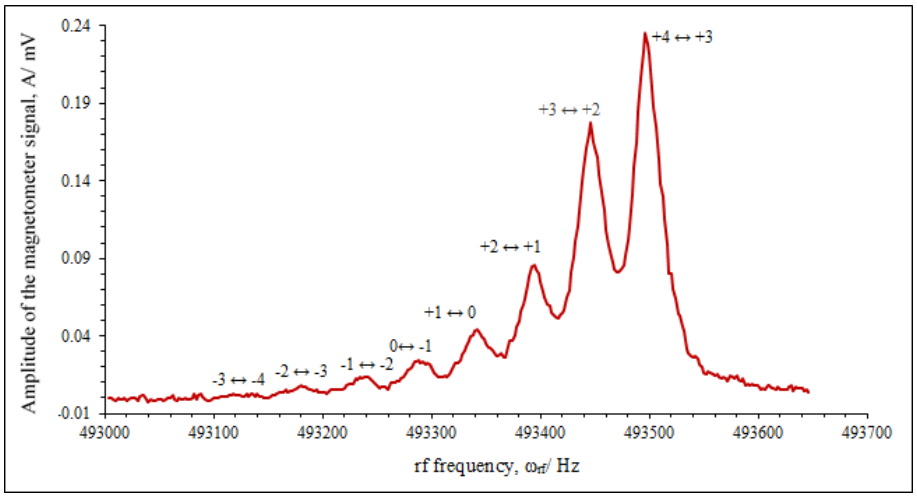

Figure 6.1: Typical rf spectrum obtained in a high magnetic field (14 μT). The non-linear Zeeman effect results in eight distinct rf resonances corresponding to the transitions between successive magnetic sublevels ($m \leftrightarrow m' = m - 1$) in the $F = 4$ ground state. Spectrum was taken for probe power = 573 μW and pump power = 993 μW.

The amplitude of each peak in Figure 6.1 is proportional to the population difference between neighbouring sublevels, and allows deduction of the population distribution at a given pumping intensity level.

One noticeable feature in Figure 6.1 is that the ratio of the two biggest resonances is 1.44. This is lower than the value obtained by Chalupczak et al. [100] in 2011, in which the strongest rf resonance was four times larger than the adjacent resonance (Figure 6.2). The discrepancy in the two values is due to the setup used. The setup used by Chalupczak et al. [100] used five layers of mu-metal shields to cancel the ambient magnetic field whilst the setup described in this thesis uses three layers. It confirms that the efficiency of the indirect pumping technique using three layers of shields is lower than that recorded with five layers. The purpose of the shields is to cancel the ambient magnetic field and any field inhomogeneities,

allowing the quantisation axis to be effectively defined by $\boldsymbol{B}_0$. A well defined quantisation axis ensures that optical pumping will produce a long polarisation lifetime which is essential for a sensitive atomic magnetometer. The more mu-metal shields there are, the better the cancellation of the ambient magnetic field and any stray inhomogeneities, hence the more efficient pumping will be.

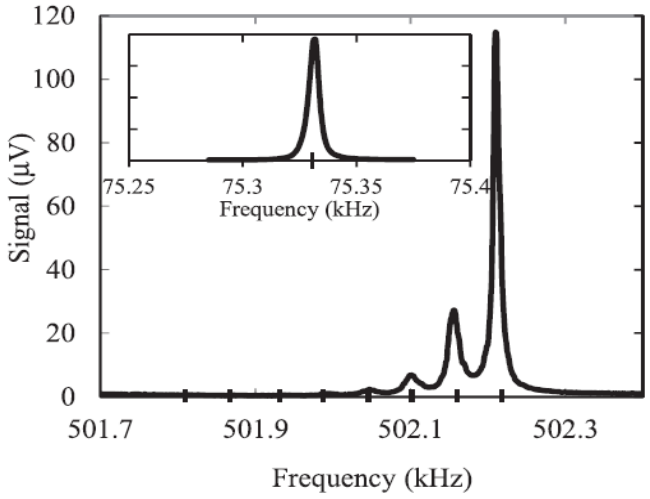

Figure 6.2: rf spectrum taken from Chalupczak et al. [100] showing that the amplitude of the largest resonance is about four times larger than the adjacent resonance. The efficiency of indirect optical pumping was very efficient within five layers of mu-metal magnetic shields because the shields are very good at cancelling the ambient magnetic field and any stray inhomogeneities. The inset picture shows the spectrum obtained in the low field regime. Spectra were measured with pump beam power = 600 μW and a probe beam power = 1 μW. Image taken from [100].

The second important observation is that as a consequence of indirect pumping, there is negligible power broadening of the components, even for the relatively high laser power (993 μW). The linewidths of the peaks can be affected by optical power broadening for laser powers above 1 μW [155].

The amplitudes of the rf resonances depend on the population difference between two rf-coupled Zeeman sublevels so achievement of the highest possible orientation in the atom is desired [100, 156]. In the experimental setup described in this thesis, the degree of orientation that can be produced within an atomic density at room temperature depends on the power of the pump laser. To gain a deeper insight into how the pump power affects the rf resonances of the ground state, the

rf spectra at various pump powers were recorded. The amplitudes and linewidths of the four largest rf components of each spectrum were fitted with a Lorentzian profile using a LabVIEW program in order to extract the amplitudes and linewidths of the resonances.

A plot of the change in linewidth of the magnetometer signal with increasing pump beam power in Figure 6.3 indicates that the $F = 4$ rf components are not power broadened by the pump beam as it is coupled to the $F = 3$ ground state.

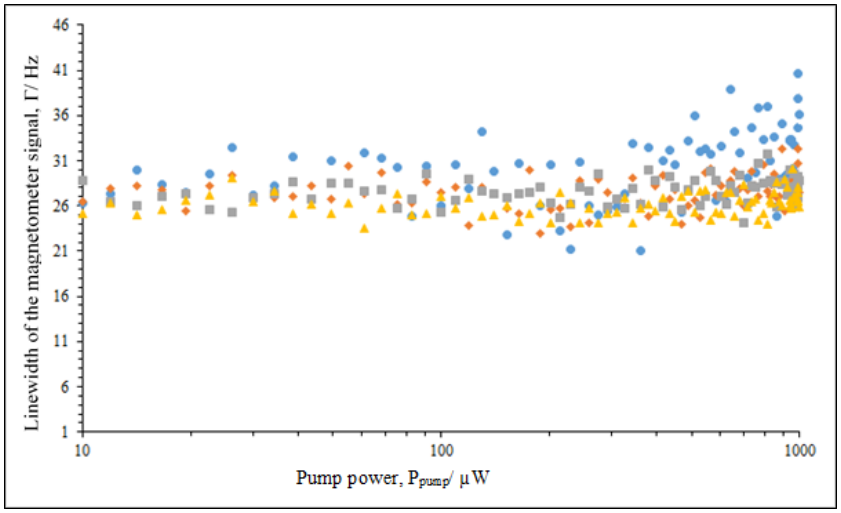

Figure 6.3: Linewidth of the four largest rf resonances of the $F = 4$ ground state against pump power. Yellow triangles indicate the $(+1 \leftrightarrow 0$ rf peak), grey squares indicate the $(+2 \leftrightarrow +1)$ rf peak, orange diamonds indicate the $(+3 \leftrightarrow +2)$ rf resonance and blue circles indicate the $(+4 \leftrightarrow +3)$ rf resonance.

Now, a plot of the change in amplitude of the magnetometer signal with increasing pump power reveals that as the pumping becomes better, the amplitudes of the last two peaks grow as more atoms come to occupy the last three sublevels. Each blue circle is proportional to the signal amplitude of the population difference between the penultimate and last sublevel at a given pump power. This indicates that there is a large population difference between those two peaks, and when compared with the orange circles which are proportional to the population difference between the third to last and penultimate sublevels, it is deduced that a large proportion of the atoms occupy the last magnetic sublevel (the stretched state). The optimum power of the strongest rf resonance ($m_F = +4 \leftrightarrow m_F = +3$ transition) occurs at 361 μW, and for the power range $396 - 991$ μW, it is noticed that the amplitude level

contracts slightly. This is attributed to a reduction in pump intensity caused by a decrease in diffraction efficiency of the AOM when the rf drive power is too high [157]. Because the strongest rf resonance corresponds to the $m_F = +4 \leftrightarrow m_F = +3$ transition, the magnetometer is operated using this rf resonance.

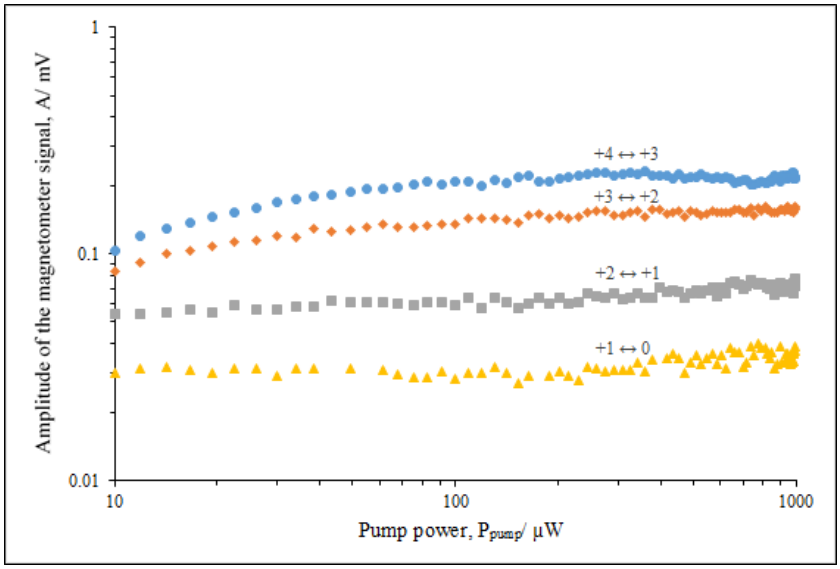

Figure 6.4: Amplitude of the four largest rf peaks of the $F = 4$ ground state versus pump beam power. The amplitudes of each peak is proportional to the population difference between the adjacent sublevels. Yellow triangles indicate the $(+1 \leftrightarrow 0$ rf peak), grey squares indicate the $(+2 \leftrightarrow +1)$ rf peak, orange diamonds indicate the $(+3 \leftrightarrow +2)$ rf resonance and blue circles indicate the $(+4 \leftrightarrow +3)$ rf resonance.

6.2.2 Signal to Noise Ratio (SNR)

Now that the optimum pump power for producing a high degree of orientation in the atomic vapour has been established in section, 6.2.1, the next stage is to find the SNR. This is done by looking at the amplitudes of the magnetometer signal and various noise components as a function of probe power. The probe power was varied from $0.19 - 4268\ \mu W$ while the pump power was fixed at 361 μW. For each probe power, rf spectra of the magnetometer signal and the various noise components were recorded by sweeping the rf field and processing the signal using the lock-in amplifier.

As stated in chapter 3 section 3.3, the sensitivity of the magnetometer is fundamentally limited by three sources of noise, excluding electronic noise: the atomic

projection noise, the photonic shot noise and quantum back-action. To record the atomic projection noise and probe beam quantum back-action at each probe power, $\boldsymbol{B}_{rf}$ was turned off. The atomic projection noise arises as a result of stochastic atomic spin fluctuations which are mapped onto the fluctuations of the polarisation plane of the probe beam. Aleksandrov and Zapasskii [158] pointed out that fluctuations of the magnetisation along the static magnetic field are caused by fluctuations of populations of the magnetic sublevels, while fluctuations of the transverse magnetisations are due to fluctuations of the coherences of the magnetic sublevels. So turning $\boldsymbol{B}_{rf}$ off enables the generation of the spontaneous coherences by the random fluctuations. As described in chapter 3 section 3.3.3, quantum back-action is due to a fictitious magnetic field produced along the propagation direction of the probe beam as a result of the quantum fluctuations in the degree of circular polarisation, that changes the atoms' precessional frequency by shifting the energy levels of the ground state, replicating the change by $\boldsymbol{B}_0$. So, in the absence of $\boldsymbol{B}_{rf}$, the spontaneous coherences between the shifted neighbouring sublevels reveal the presence of quantum back-action.

The photonic shot noise was obtained by turning off both $\boldsymbol{B}_0$ and $\boldsymbol{B}_{rf}$. This was done to record the photon flux hitting the two photodiodes.

Lastly, the electronic noise was recorded by again turning off $\boldsymbol{B}_0$ and $\boldsymbol{B}_{rf}$, along with blocking the pump and probe beams. This allowed only the fluctuations due to electrical components to be recorded.

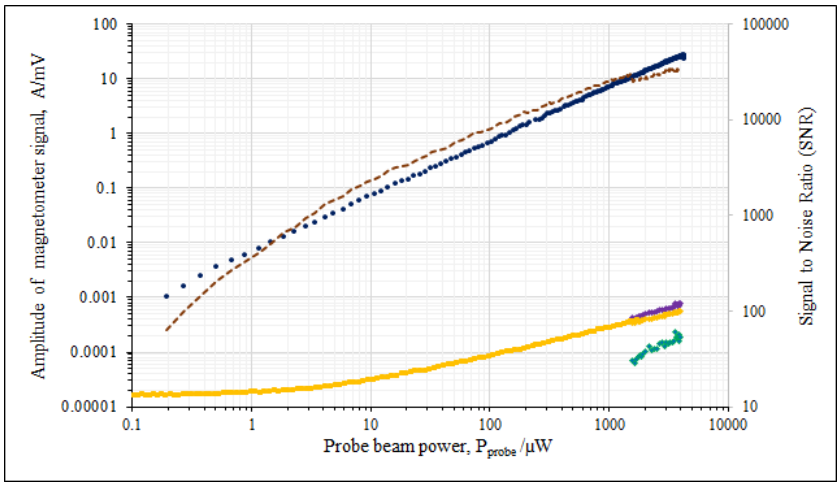

Figure 6.5: The blue circles show the amplitude of the magnetometer signal versus the probe beam power. Background of the noise (yellow squares) includes electronic noise and photonic shot noise, while the green diamonds is the noise component oscillating at ω_L. It consists of the atomic projection noise and probe beam quantum back-action. The sum of the various components of the noise is depicted by the purple diamonds. The brown dashed line represents the ratio between the signal and the noise. The probe laser is detuned by 4740MHz from the $6^2S_{\frac{1}{2}}F = 4 \rightarrow 6^2P_{\frac{3}{2}}F' = 5$ transition.

In Figure 6.5, the magnetometer signal is a linear function of the probe beam power. This is due to the relatively big detuning, 4740 MHz, of the probe laser from the $6^2S_{\frac{1}{2}}F = 4 \rightarrow 6^2P_{\frac{3}{2}}F' = 5$ transition. In other words, the probe beam does not affect the Zeeman coherences of the ground state, thus, there is no saturation in the signal, even at the highest probe powers.

For probe powers below 10 μW, the electronic noise of the detection system characterises the the noise level of the atomic magnetometer [159]. Above that power, the leading contribution comes from the photonic shot noise. This noise scales with the square root of the probe laser power. Both these components contribute to the background noise (yellow squares in Figure 6.5). The atomic projection noise and probe beam quantum back-action are visible from around 1562 μW (green diamonds in Figure 6.5). The small non-linearity in the amplitude of the atomic noise with probe power is due to a small modification by the tensor term in the effective Hamiltonian (equation (2.27) in chapter 2, section 2.5.3) that describes the atom-probe-light interaction [160]. The amplitude of the atomic noise component is inversely proportional to the probe beam detuning; smaller detunings

result in a larger atomic projection noise component. For the detuning used in current measurements (4740 MHz from the $6^2S_{\frac{1}{2}}F = 4 \rightarrow 6^2P_{\frac{3}{2}}F' = 5$ transition), this amplitude was lower than the amplitude of the photonic shot noise. The combined noise is shown with the purple diamonds. The brown dotted line represents the SNR which shows no saturation at the higher powers. This is because of the relatively low amplitude of the atomic noise component which is a consequence of the ratio between the probe laser power and its detuning from the $6^2S_{\frac{1}{2}}F = 4 \rightarrow 6^2P_{\frac{3}{2}}F' = 5$ transition.

6.2.3 The Calibrated rf Magnetic Field

To find the sensitivity of the magnetometer, it was necessary to calibrate the rf magnetic field. This was done using the atomic spins' response to the rf magnetic field. It relies on monitoring the amplitude and the linewidth of the $m_F = +4 \leftrightarrow m_F = +3$ coherence as a function of the amplitude of $\boldsymbol{B}_{rf}$. When the amplitude of $\boldsymbol{B}_{rf}$ (in terms of Rabi frequency) is equal to the linewidth of the coherence, saturation in the amplitude of the signal is observed, and simultaneously the linewidth of the rf resonance increases by the factor of $\sqrt{2}$.

The Rabi frequency is expressed as:

$$\omega_R = \gamma B_{rf} = \frac{g_s \mu_B}{2\hbar} B_{rf} = \frac{\mu_B}{\hbar} B_{rf} \tag{6.1}$$

where $g_s = 2.00231930436182(52)$ [56] is the absolute value of the electron spin g-factor. B_{rf} in terms of the Rabi frequency can be found by re-arranging equation (6.1):

$$B_{rf} = \frac{\omega_R \hbar}{\mu_B} \tag{6.2}$$

Figures 6.6a and 6.6b show how the amplitude and linewidth of the coherence vary with the amplitude of the rf magnetic field. The amplitude of the rf field was varied by changing the rf power (in dBm) of the waveform generator that produced the rf field and recording the rf spectrum by sweeping the rf field while keeping the pump and probe powers fixed at 361 μW and 100 μW, respectively. Then the $m_F = +4 \leftrightarrow m_F = +3$ coherence from each spectrum was fitted with a Lorentzian

profile using a LabVIEW program in order to extract the amplitude and linewidth. The results were plotted against the rf power to produce Figures 6.6a and 6.6b. The gap in both graphs is due to the fact that an additional two attenuators were added to the output of the waveform generator during the measurement taking. This was done because $\boldsymbol{B}_{rf}$ saturated very quickly so the two attenuators were added to decrease the output rf power. Thus, the gap in the graphs show which measurements were taken with the addition of the attenuators and which were taken without. From Figure 6.6a, it is observed that saturation of the signal occurs at -2 dBm. The linewidth at saturation, Γ_{SAT} is:

$$\Gamma_{SAT} = \sqrt{2}\omega_R \tag{6.3}$$

where $\Gamma_{SAT} = 2\pi \times 40$ Hz, according to Figure 6.6b.

Therefore, inserting equation (6.3) into equation (6.2) gives the rf magnetic field at saturation:

$$B_{rf}^{sat} = \frac{\Gamma_{SAT}}{\sqrt{2}} \frac{\hbar}{\mu_B} \tag{6.4}$$

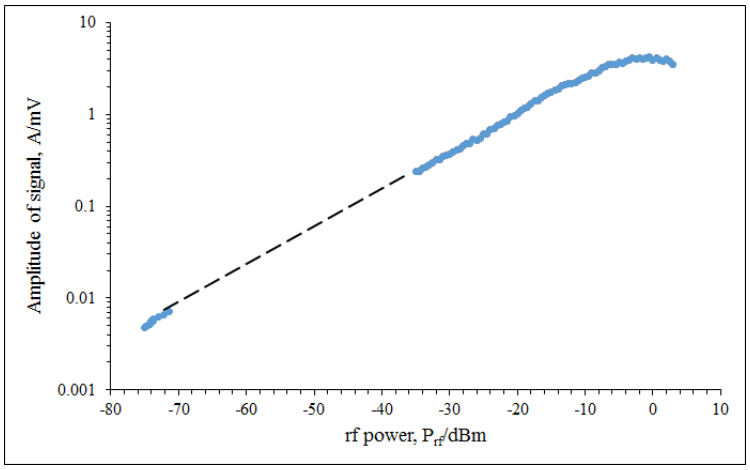

(a)

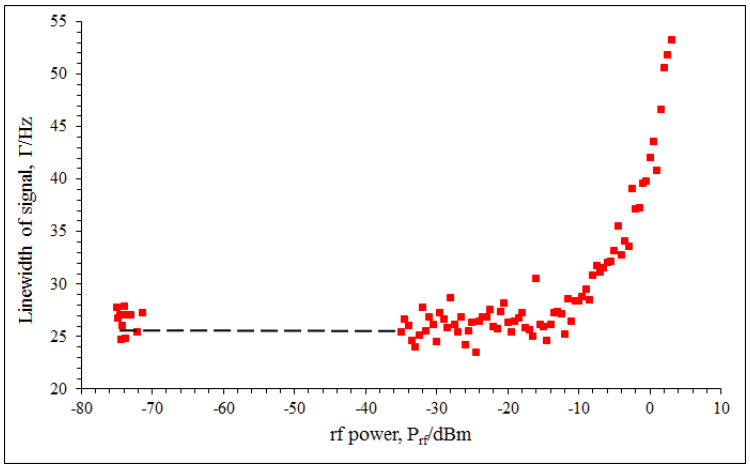

(b)

Figure 6.6: rf amplitude (a) and rf linewidth (b) of the $m_F = +4 \leftrightarrow m_F = +3$ coherence against rf power. The gap in both graphs is due to the fact that an additional two attenuators were added to the output of the waveform generator that generated the rf magnetic field, during the measurement taking.

B_{rf}^{sat} turns out to be 2.02 nT. The amplitude around saturation according to Figure 6.6a is 4.16 mV. For the experiments described here, an rf power of -75 dBm was set. This value was chosen because it enabled the generation of a large coherence signal without greatly affecting the linewidth of the signal. The amplitude corresponding to -75 dBm is 0.0048 mV. Looking at the graph, there is a linear dependence between the amplitude of B_{rf} and the rf power before saturation occurs. Therefore, the ratio of the rf amplitudes at -2 dBbm and -75 dBm can be used to determine the amplitude of the magnetic field at -75 dBm. This ratio is $\frac{4.16}{0.0048} = 863$. Consequently, the amplitude of B_{rf} at -75 dBm is

$\frac{2.02\times10^{-9}}{863} = 2.342\times10^{-12}$ T.

6.2.4 Sensitivity of the Magnetometer

Now, the next step is to use the calibrated rf magnetic field, $B_{rf} = 2.342 \times 10^{-12}$ T to find the sensitivity of the rf magnetometer. Figure 6.7 shows the magnetometer signal and noise components recorded by the Agilent N9010A spectrum analyser. The pump and probe powers were 361 μW and 4200 μW, respectively. The large peak tuned to the centre of the $m_F = +4 \leftrightarrow m_F = +3$ transition, represents the signal recorded with the rf field on. This peak is calibrated to be 2.342 x10^{-12} T or (2342 fT).

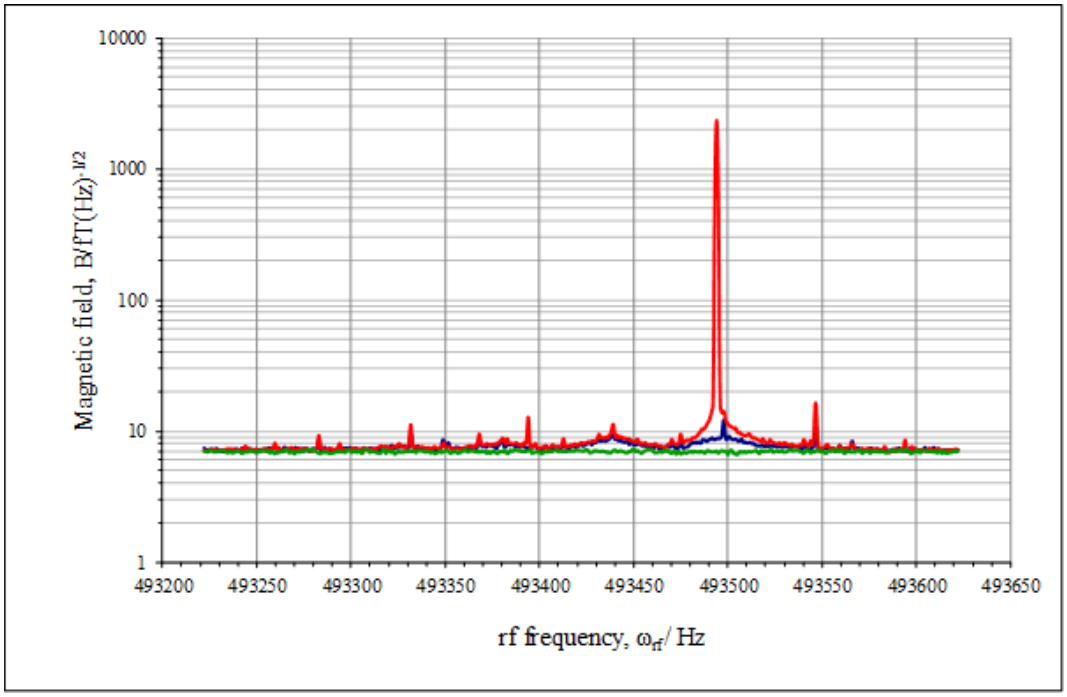

Figure 6.7: Noise spectrum of the magnetometer recorded with (red solid line) and without (blue solid line) an rf magnetic field. The blue sold line shows the atomic projection noise and probe beam quantum back-action spectrum while the photonic shot noise level is marked with a green solid line. The resolution bandwidth for the measurement was 1 Hz.

From Figure 6.7, the green solid line shows the photonic shot noise level which has a value of ≈ 7.34 fT$/\sqrt{\text{Hz}}$. The red solid line shows the rf spectrum recorded with $\boldsymbol{B}_{rf}$ turned on while the blue solid line depicts the rf spectrum recorded without any rf field. The blue solid line shows the probe beam quantum back-action, along

with the atomic projection noise spectrum which as a consequence of the fluctuation dissipation theorem, mirrors that generated by the interaction with an rf magnetic field [161]. When the atomic medium is not completely oriented, there will be components of the atomic projection noise and probe beam quantum back-action at frequencies lower than that of the $m_F = +4 \leftrightarrow m_F = +3$ transition [100]. At low static magnetic fields, the signal and the noise increase because the different transitions overlap. Thus, to first order, when noise is dominated by atomic projection noise and probe beam quantum back-action, the sensitivity of the magnetometer does not depend on frequency of the magnetic field to be detected. The value of this noise from Figure 6.7 is ≈ 12.08 fT$/\sqrt{\text{Hz}}$. Using this information, the smallest magnetic field that is able to be detected by the magnetometer is ≈ 12.08 fT$/\sqrt{\text{Hz}}$.

6.3 Evaluating the SNR at different probe beam detunings

One of the most important indicators of the sensitivity of a magnetometer is the SNR. The higher the SNR, the better the sensitivity. This section takes a closer look at the relationship between the SNR and probe beam detuning so as to explore what happens to the SNR when the detuning of the probe beam is changed. The SNRs at four probe beam detunings are explored.

The master laser was locked to the $6^2S_{\frac{1}{2}}F = 3 \rightarrow 6^2P_{\frac{3}{2}}F' = 3$ transition and the probe was red detuned by 6940 MHz, 7340 MHz, 7940 MHz and 8140 MHz from the master, so that it is closer to the $F = 4$ resonance. Hence, the probe is detuned 1800 MHz, 1400 MHz, 800 MHz and 600 MHz from the $6^2S_{\frac{1}{2}}F = 4 \rightarrow 6^2P_{\frac{3}{2}}F' = 5$ transition, respectively. The power of the pump used was 100 μW. However, it should be noted that it was not the optimum pump power as the focus of this experiment was the recording of the SNR at various probe beam detunings.

Like section 6.2.2, at every probe beam detuning, the amplitudes of the magnetometer signal and the various noise components, were recorded as a function of the probe power. These results are shown in Figure 6.10.

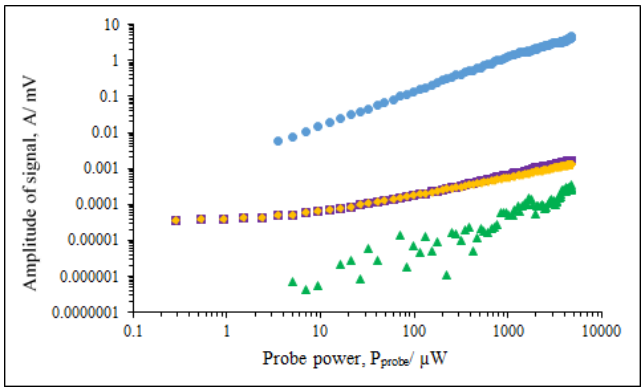

(a)

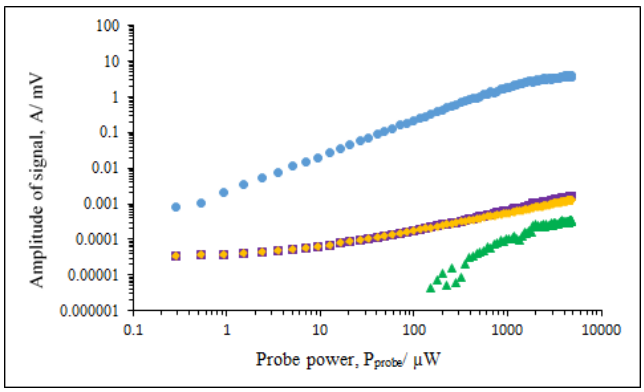

(b)

Figure 6.8: The blue circles show the amplitude of the magnetometer signal versus the probe beam power. Background of the noise (yellow diamonds) includes electronic noise and photonic shot noise, while the green triangles represent the noise component oscillating at ω_L which consists of the atomic projection noise and probe beam quantum back-action. The sum of the various components of the noise is depicted by the purple squares. The probe laser is detuned by 1800 MHz (a) and 1400 MHz (b) from the $6^2S_{\frac{1}{2}}F = 4 \rightarrow 6^2P_{\frac{3}{2}}F' = 5$ transition. The pump power used was 100 μW.

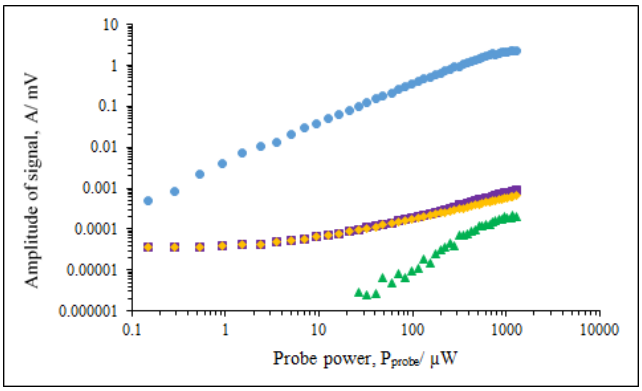

(a)

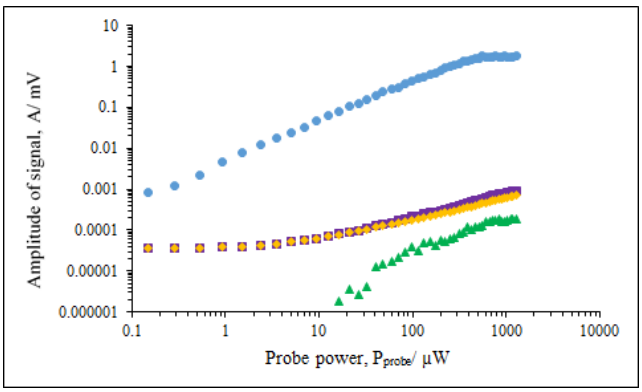

(b)

Figure 6.9: The blue circles show the amplitude of the magnetometer signal versus the probe beam power. Background of the noise (yellow diamonds) includes electronic noise and photonic shot noise, while the green triangles represent the noise component oscillating at ω_L which consists of the atomic-projection noise and probe beam quantum back-action. The sum of the various components of the noise is depicted by the purple squares. The probe laser is detuned by 800 MHz (a) and 600 MHz (b) from the $6^2S_{\frac{1}{2}}F = 4 \rightarrow 6^2P_{\frac{3}{2}}F' = 5$ transition. The pump power used was 100 μW.

In Figure 6.8a, it is observed that at the large detuning of 1800 MHz, there is no saturation in the signal. But as the detuning gets smaller, saturation of the signal is observed (Figures 6.8b, 6.9a, 6.9b). Figure 6.10 shows the comparison of the SNR for the different probe beam detunings as a function of the probe power.

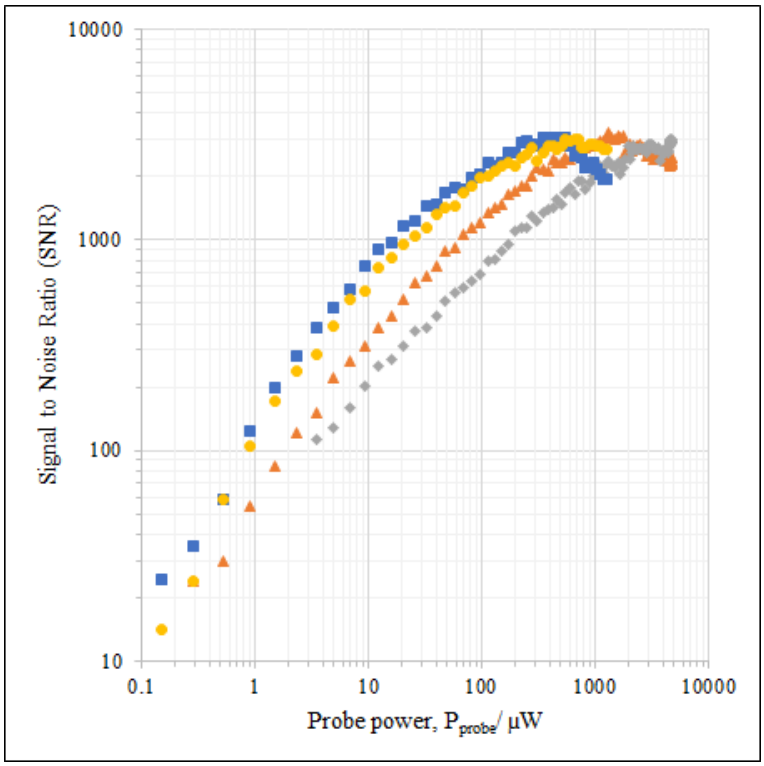

Figure 6.10: Signal to noise ratios (SNRs) of different probe beam detunings from the $6^2S_{\frac{1}{2}}F = 4 \rightarrow 6^2P_{\frac{3}{2}}F' = 5$ transition as a function of probe power. The detunings are 600 MHz (blue squares), 800 MHz (yellow circles), 1400 MHz (orange triangles) and 1800 MHz (grey diamonds).

The first important observation that can be made from Figure 6.10 is that the SNR does not change with probe beam detuning. Even though the difference between the largest and smallest detuning is 1800 MHz -600 MHz $= 1200$ MHz, the SNR remains constant at about 5000. This indicates that the sensitivity is not improved significantly the more off-resonant the probe beam is.

The second important observation is that in order to reach the optimum SNR at the probe beam detuning of 1800 MHZ, the probe power required is 3713 μW, while at the detuning of 600 MHz, only 348 μW is required. There is an order of magnitude difference in probe power for the largest and smallest detuning. This suggests that the further the probe beam is from the resonant transition, the higher the probe power needs to be in order to reach the optimum SNR.

6.4 Summary of Important Results

In this chapter, the sensitivity of the rf atomic magnetometer was evaluated at a probe beam detuning of 4740 MHz from the $6^2S_{\frac{1}{2}}F = 4 \rightarrow 6^2P_{\frac{3}{2}}F' = 5$ transition. The optimum pump power for producing orientation in the room temperature atomic vapour was found to be 361 μW. The signal from the magnetometer was a linear function of probe power, with no saturation. This indicated that the probe beam does not affect the Zeeman coherences of the $F = 4$ ground state and is a consequence of the probe beam detuning. In addition, there was no saturation of the SNR which is a result of the relatively low atomic-projection noise component. Using a calibrated rf magnetic field, the sensitivity of the rf magnetometer was determined to be ≈ 12.08 fT$/\sqrt{\text{Hz}}$.

When investigating the relationship between the SNR and probe beam detuning, it was found that the SNR does not change with probe beam detuning, hence, sensitivity is not significantly improved with detuning. However, to reach the optimum SNR at larger detunings, the higher the probe power needs to be.

Chapter 7

Summary and Conclusions

This thesis has described the development of a room temperature Cs rf magnetometer. Exploration of the atomic magnetometer commenced by examining the effect of probe beam detuning on the magnetometer signal of the $F = 3$ and $F = 4$ ground states. This was done using a small magnetic field (9.3 μT) so that the linear Zeeman effect dominated because it was only the total coherence amplitude that was of interest. Optical probing is divided into two categories depending on the detuning of the probe beam: absorptive or off-resonant.

It was found that there were two absorptive regimes. These were when the probe beam was in the vicinity of either the $6^2S_{\frac{1}{2}}F = 3 \rightarrow 6^2P_{\frac{3}{2}}F' = 2,3,4$ or the $6^2S_{\frac{1}{2}}F = 4 \rightarrow 6^2P_{\frac{3}{2}}F' = 3,4,5$ transitions. When in the vicinity of the $6^2S_{\frac{1}{2}}F = 3 \rightarrow 6^2P_{\frac{3}{2}}F' = 2,3,4$ transitions, the probe beam transferred atoms from the $F = 3$ ground state to the $F = 4$ ground state. This was evidenced by the disappearance of the signal amplitude of the $F = 3$ component, along with the changing of the amplitude and shape of the $F = 4$ ground state signal component. When near the $6^2S_{\frac{1}{2}}F = 4 \rightarrow 6^2P_{\frac{3}{2}}F' = 3,4,5$ transitions, there was no transfer of atomic population between the $F = 3$ and $F = 4$ ground states; only the $F = 4$ signal amplitude and shape changed. This is indicative of the fact that most of the atoms excited by the probe beam were excited to the $F' = 5$ level. When they decayed, they were only able to return to the $F = 4$ ground state because the $6^2P_{\frac{3}{2}}F' = 5 \rightarrow 6^2S_{\frac{1}{2}}F = 3$ is a forbidden transition.

The off-resonant regime was characterised by the dispersive dependence of

the $F = 3$ and $F = 4$ signal amplitudes on the probe beam detuning. The regime is described by the effective Hamiltonian which contains two terms: the first term represents the polarisation rotation by the Faraday effect and is a QND interaction while the second term represents an alignment tensor that represents a perturbation of the probe that alters the state of the atoms. The relative magnitude of these two terms depends on the probe beam detuning. There was no broadening of the linewdith of the $F = 3$ ground state component for detunings greater than 4000 MHz from the $6^2S_{\frac{1}{2}}F = 3 \rightarrow 6^2P_{\frac{3}{2}}F' = 2$ transition. This indicated that the the probe beam did not perturb the atomic spins. The tensor light shift was observed for red detunings between 750 MHz to 1150 MHz from the $6^2S_{\frac{1}{2}}F = 3 \rightarrow 6^2P_{\frac{3}{2}}F' = 2$ transition, indicating a perturbation by the probe beam.

The second stage of exploration entailed determining the sensitivity of the magnetometer. From a calibrated rf magnetic field, it was shown that the smallest magnetic field measurable by the rf atomic magnetometer was ≈ 12.08 fT$/\sqrt{\text{Hz}}$. When this value is compared with the sensitivities obtained in current research, it is found to be not as good. Chalupczak et al. [100] in 2012 demonstrated a sensitivity of ≈ 1 fT$/\sqrt{\text{Hz}}$ using a room temperature Cs rf atomic magnetometer. The setup used five layers of mu-metal shields to cancel the ambient magnetic field and stray inhomogeneities. This resulted in a high degree of orientation (92%) within the atomic vapour because the quantisation axis was well defined by the static magnetic field, $\boldsymbol{B}_0$. Sheng et al. [162] in 2013 demonstrated a sensitivity of 0.34 fT$/\sqrt{\text{Hz}}$ with a Rb scalar atomic gradiometer that used two multipass optical cells. It operated in a pulsed pump-probe mode and took advantage of spin-squeezing techniques. As mentioned in the introductory chapter, the most sensitive atomic magnetometers are the SERF magnetometers. In 2009, Smullin et al.[163] demonstrated a sensitivity of 7 fT$/\sqrt{\text{Hz}}$ using a high density optically pumped K atomic magnetometer with an active measurement volume of 1.5 cm^3. Sheng et al. [164] in 2017 demonstrated a sensitivity of 10 fT$/\sqrt{\text{Hz}}$ using a compact Cs atomic magnetometer. Their value was attributed to the higher atomic density (temperature of the cell was heated to approximately 120°), the five layer magnetic shielding which suppressed the back-

ground magnetic noise, and the higher purity of the polarisation. In 2016, Savukov et al. [165] demonstrated a sensitivity of 5 fT/$\sqrt{\text{Hz}}$ at 50 Hz using a high density Rb atomic magnetometer, operating in the SERF regime. This was achieved by heating the cell of Rb atomic vapour to 200°. The sensitivity of the rf atomic magnetometer described in this thesis is limited by the number of magnetic shields used. As discussed in chapter 6 section 6.2.1, the efficiency of the indirect pumping technique used to produce orientation within the atomic vapour is lower with three layers of mu-metal shields than with five layers, which was the number used by Chalupczak et al. [100]. Effective optical pumping will produce a long polarisation lifetime which is essential for a sensitive atomic magnetometer. The more mu-metal shields there are, the better the cancellation of the ambient magnetic field and any stray inhomogeneities, hence the more efficient pumping will be. A good solution to this limitation would be to use compensation coils within the shields to cancel the magnetic field noise. The other limitation is the atomic density used. Sensitivity increases with density. However, the atomic density used in the experiments described in this thesis was kept at room temperature because a potential use for the atomic magnetometer is in real world applications so there was a trade-off between sensitivity and mimicking real world conditions.

In addition, the investigation into the relationship between the SNR of the magnetometer and the probe beam detuning revealed that the SNR does not change with detuning, however, for bigger detunings, a higher probe power was necessary to obtain the optimum SNR.

One of the limitations of the experimental method was the significant loss of intensity at the output of the fibre due to the very large divergent beam. It was impossible to collimate the entire beam. The beam diverged very quickly with a diameter larger than the diameter of the lens used. Another limitation was the use of the AOM in a double pass configuration. Only fifty percent of the light was able to be injected into the AOM on the second pass while eighty percent of the light was injected on the first pass. Thus, for future experiments the optical elements breadboard will be modified for single pass AOMs.

In terms of the results, a larger slave offset frequency range would have been useful to examine the $F = 4$ component thoroughly. Secondly, a better model of the absorptive regime is currently being devised.

The next step in the exploration of the rf atomic magnetometer is in the field of biomedical applications, where it will be used as the sensor in Magnetic Induction Tomography (MIT). Magnetic induction tomography is a recently developed technique for the investigation of the electrical and magnetic properties of an object [166, 167]. It is a non-invasive technique for imaging the passive electromagnetic properties of materials at frequencies below 2 MHz. It uses a magnetic field generated by an excitation coil to induce eddy currents in the object of interest, causing them to produce their own magnetic fields, which are then detected by sensing coils. Its non-invasive nature allows a direct mapping of conductivity, σ, permittivity, ε, and permeability, μ, without requiring any physical contact [167].

MIT applies an AC magnetic field (the primary magnetic field), $\boldsymbol{B}_1$, from an excitation coil in order to induce eddy currents in the object of interest [166, 167]. The density of these currents depends on the electromagnetic properties of the object [168]. They produce a secondary magnetic field, $\boldsymbol{B}_2$ which opposes $\boldsymbol{B}_1$. The amplitude and phase of the total magnetic field, $\boldsymbol{B}_{TOT} = \boldsymbol{B}_1 + \boldsymbol{B}_2$, contains information about the distribution of σ, ε and μ [168]. By performing position-resolved measurements of $\boldsymbol{B}_{TOT}$, a map of the electromagnetic properties can be constructed [168].

If the penetration depth of $\boldsymbol{B}_1$ is larger than the thickness of the object of interest, then $\boldsymbol{B}_2$, oscillating at the frequency ω, can be estimated as:

$$\boldsymbol{B}_2(\omega) = Q\omega\mu_0[\omega\varepsilon_0(\varepsilon_r - 1) - i\sigma] + P(\mu_r - 1)\boldsymbol{B}_1(\omega) \tag{7.1}$$

where Q and P are geometrical factors, ε_r is the relative permittivity, and μ_r is the relative permeability [169]. The eddy currents in the material cause a component of $\boldsymbol{B}_2$ which is proportional to ω and lags $\boldsymbol{B}_1$ by 90° [166]. In general, $\boldsymbol{B}_2$ will have real and imaginary components representing the permittivity and conductivity of the sample, respectively [166]. The conductivity (imaginary component) in biological

tissues is normally dominant [166].

The ultimate performance of an MIT system is dependent on the magnetic sensor [118]. A typical MIT setup consists of a standard coil of wire which produces $\boldsymbol{B}_1$, along with either a second single coil or an array of coils for detection. However, such devices suffer from the limitations and drawbacks of the coils. Some of the limitations of conventional setups include reduced sensitivity at low frequencies, insufficient bandwidth to adapt to different, non-conductive objects, and cannot be reduced below the physical size of the sensing coil/s, thus, limiting the spatial resolution [167]. Consequently, there have been advances in alternative detection techniques. One such advancement is using the atomic magnetometer. Because they have been shown to have sensitivities as good as SQUIDs and potential for miniaturisation, atomic magnetometers are a very attractive option for MIT setups. Indeed, MIT measurements with an atomic magnetometer have been very promising. In 2013, Wickenbrock et al. [118] showed that when a conductive material is placed in close proximity (1.5 cm) to the magnetometer, it is possible to measure the phase variation of the magnetic fields produced by eddy currents in the material and in 2014, Wickenbrock et al. [170] created a conductivity map of a few 2 mm thick aluminium objects of different shapes and sizes. Subsequent research has been just as successful in creating conductivity maps of metallic objects using atomic magnetometers [171, 172].

MIT has found use in many different areas such as the process industry [173–176], and the defence and surveillance industry [177–180]. Within the biomedical field, there is currently no technique for mapping the conductivity of biological tissues such as the heart. Traditional techniques such as MCG and electrocardiography (ECG) do not provide any direct information on conductivity. Combining the advantages of MIT with that of atomic magnetometers will provide a sensitive means of acquiring information about the conductivity of biological tissues.

Appendix A

Alkali Vapour Densities

The saturated density of the alkali vapour in units of cm^{-3} at a temperature T in Kelvin is given by the equation:

$$n = \frac{1}{T} 10^{21.866 + A - \frac{B}{T}} \tag{A.1}$$

The appropriate value of the constants, A and B, are given in table A.1

Atomic Metal	Melting Point (°C)	Solid		Liquid	
		A	B	A	B
Potassium	63.5	4.961	4646	4.402	4453
Rubidium	39.3	4.857	4215	4.312	4040
Caesium	28.5	4.711	3999	4.165	3830

Table A.1: Values for equation (A.1) to find the alkali vapour density at a given temperature. The parameters are different depending on whether the metal is above or below the melting point. Density parameters are taken from [181].

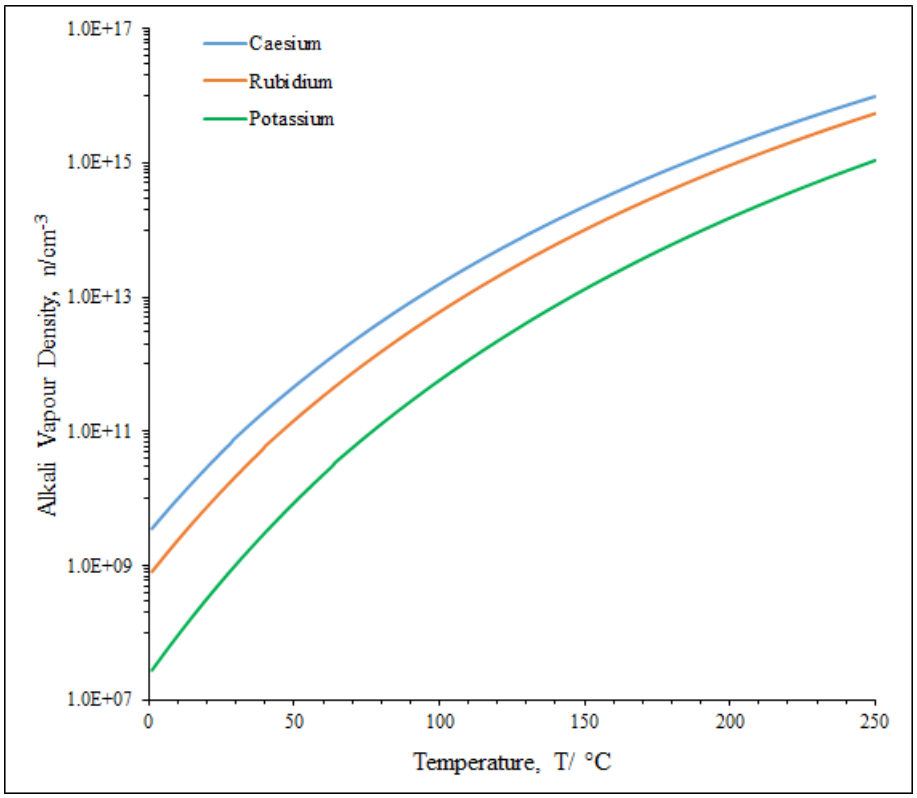

Figure A.1: Comparison of the alkali vapour densities, caesium (blue), rubidium (orange) and potassium (potassium), as a function of temperature. The alkali metal vapour densities were calculated from equation (A.1).

Bibliography

[1] Magnetometer-the history. http://www.ctsystems.eu/support/magnetometer-the-history/. Accessed: 2017-09-30.

[2] Scott Jeffrey Seltzer. *Developments in alkali-metal atomic magnetometry*. Princeton University, 2008.

[3] Dmitry Budker and Derek F Jackson Kimball. *Optical magnetometry*. Cambridge University Press, 2013.

[4] F Bloch, AC Graves, M Packard, and RW Spence. Relative moments of H^1 and H^3. *Physical Review*, 71(8):551, 1947.

[5] Felix Bloch. Nuclear induction. *Physical review*, 70(7-8):460, 1946.

[6] M Packard. Free nuclear induction in earth's magnetic field. *Phys. Rev.*, 93:941, 1954.

[7] FD Colegrove and PA Franken. Optical pumping of helium in the $^3s_1$ metastable state. *Physical Review*, 119(2):680, 1960.

[8] GK Walters, FD Colegrove, and LD Schearer. Nuclear polarization of He^3 gas by metastability exchange with optically pumped metastable He^3 atoms. *Physical Review Letters*, 8(11):439, 1962.

[9] FD Colegrove, LD Schearer, and GK Walters. Polarization of He^3 gas by optical pumping. *Physical Review*, 132(6):2561, 1963.

[10] R Slocum and B Marton. A nuclear free precession magnetometer using optically polarized He^3 gas. *IEEE Transactions on Magnetics*, 10(3):528–531, 1974.

[11] John Clarke and Alex I Braginski. The squid handbook, vol. 1. *I Fun*, 2004.

[12] Brian David Josephson. Possible new effects in superconductive tunnelling. *Physics letters*, 1(7):251–253, 1962.

[13] Philip W Anderson and John M Rowell. Probable observation of the josephson superconducting tunneling effect. *Physical Review Letters*, 10(6):230, 1963.

[14] Squids. http://hyperphysics.phy-astr.gsu.edu/hbase/Solids/Squid.html. Accessed: 2017-09-30.

[15] Asaf Grosz, Michael J Haji-Sheikh, and Subhas C Mukhopadhyay. *High sensitivity magnetometers*. Springer, 2017.

[16] Igor Savukov. Ultra-sensitive optical atomic magnetometers and their applications. In *Advances in Optical and Photonic Devices*. InTech, 2010.

[17] Stefan Groeger, Anatoly S Pazgalev, and Antoine Weis. Comparison of discharge lamp and laser pumped cesium magnetometers. *Applied Physics B: Lasers and Optics*, 80(6):645–654, 2005.

[18] Peter DD Schwindt, Svenja Knappe, Vishal Shah, Leo Hollberg, John Kitching, Li-Anne Liew, and John Moreland. Chip-scale atomic magnetometer. *Applied Physics Letters*, 85(26):6409–6411, 2004.

[19] S Knappe, PDD Schwindt, Vladislav Gerginov, V Shah, L Liew, J Moreland, HG Robinson, L Hollberg, and J Kitching. Microfabricated atomic clocks and magnetometers. *Journal of Optics A: Pure and Applied Optics*, 8(7):S318, 2006.

[20] JC Allred, RN Lyman, TW Kornack, and MV Romalis. High-sensitivity atomic magnetometer unaffected by spin-exchange relaxation. *Physical review letters*, 89(13):130801, 2002.

[21] IK Kominis, TW Kornack, JC Allred, and MV Romalls. A subfemtotesla multichannel atomic magnetometer. *Nature*, 422(6932):596, 2003.

[22] Riccardo Fenici, Donatella Brisinda, and Anna Maria Meloni. Clinical application of magnetocardiography. *Expert review of molecular diagnostics*, 5(3):291–313, 2005.

[23] Vishal K Shah and Ronald T Wakai. A compact, high performance atomic magnetometer for biomedical applications. *Physics in medicine and biology*, 58(22):8153, 2013.

[24] S Knappe, R Mhaskar, Jan Preusser, J Kitching, Lutz Trahms, and T Sander. Chip-scale room-temperature atomic magnetometers for biomedical measurements. In *5th European Conference of the International Federation for Medical and Biological Engineering*, pages 1330–1333. Springer, 2011.

[25] K Kamada, Y Ito, and T Kobayashi. Human mcg measurements with a high-sensitivity potassium atomic magnetometer. *Physiological measurement*, 33(6):1063, 2012.

[26] Robert Wylie. *The development of a multichannel atomic magnetometer array for fetal magnetocardiography*. University of Wisconsin–Madison, 2012.

[27] G Bison, R Wynands, and A Weis. A laser-pumped magnetometer for the mapping of human cardiomagnetic fields. *Applied Physics B*, 76(3):325–328, 2003.

[28] G Bison, R Wynands, and A Weis. Dynamical mapping of the human cardiomagnetic field with a room-temperature, laser-optical sensor. *Optics Express*, 11(8):904–909, 2003.

[29] G Bison, R Wynands, and A Weis. Mapping of the cardiomagnetic field using a room-temperature magnetometer. *Development of an optical cardiomagnetometer*, 48:61, 2004.

[30] Matti Hämäläinen, Riitta Hari, Risto J Ilmoniemi, Jukka Knuutila, and Olli V Lounasmaa. Magnetoencephalographytheory, instrumentation, and applications to noninvasive studies of the working human brain. *Reviews of modern Physics*, 65(2):413, 1993.

[31] H Xia, A Ben-Amar Baranga, D Hoffman, and MV Romalis. Magnetoencephalography with an atomic magnetometer. *Applied Physics Letters*, 89(21):211104, 2006.

[32] Claude Cohen-Tannoudji, Jacques Dupont-Roc, Serge Haroche, and Franck Laloë. Detection of the static magnetic field produced by the oriented nuclei of optically pumped he 3 gas. *Physical Review Letters*, 22(15):758, 1969.

[33] VV Yashchuk, J Granwehr, DF Kimball, SM Rochester, AH Trabesinger, JT Urban, D Budker, and A Pines. Hyperpolarized xenon nuclear spins detected by optical atomic magnetometry. *Physical review letters*, 93(16):160801, 2004.

[34] IM Savukov and MV Romalis. Nmr detection with an atomic magnetometer. *Physical review letters*, 94(12):123001, 2005.

[35] Adam J Moulé, Megan M Spence, Song-I Han, Juliette A Seeley, Kimberly L Pierce, Sunil Saxena, and Alexander Pines. Amplification of xenon nmr and mri by remote detection. *Proceedings of the National Academy of Sciences*, 100(16):9122–9127, 2003.

[36] IM Savukov, SJ Seltzer, and MV Romalis. Detection of nmr signals with a radio-frequency atomic magnetometer. *Journal of Magnetic Resonance*, 185(2):214–220, 2007.

[37] BJ Venema, PK Majumder, SK Lamoreaux, BR Heckel, and EN Fortson. Search for a coupling of the earths gravitational field to nuclear spins in atomic mercury. *Physical review letters*, 68(2):135, 1992.

[38] JM Brown, SJ Smullin, TW Kornack, and MV Romalis. New limit on lorentz-and c p t-violating neutron spin interactions. *Physical review letters*, 105(15):151604, 2010.

[39] Szymon Pustelny, Derek F Jackson Kimball, Chris Pankow, Micah P Ledbetter, Przemyslaw Wlodarczyk, Piotr Wcislo, Maxim Pospelov, Joshua R Smith, Jocelyn Read, Wojciech Gawlik, et al. The global network of optical magnetometers for exotic physics (gnome): A novel scheme to search for physics beyond the standard model. *Annalen der Physik*, 525(8-9):659–670, 2013.

[40] CA Baker, Y Chibane, M Chouder, P Geltenbort, K Green, PG Harris, BR Heckel, P Iaydjiev, SN Ivanov, I Kilvington, et al. Apparatus for measurement of the electric dipole moment of the neutron using a cohabiting atomic-mercury magnetometer. *Nuclear Instruments and Methods in Physics Research Section A: Accelerators, Spectrometers, Detectors and Associated Equipment*, 736:184–203, 2014.

[41] K Green, PG Harris, P Iaydjiev, DJR May, JM Pendlebury, KF Smith, M Van der Grinten, P Geltenbort, and S Ivanov. Performance of an atomic mercury magnetometer in the neutron edm experiment. *Nuclear Instruments and Methods in Physics Research Section A: Accelerators, Spectrometers, Detectors and Associated Equipment*, 404(2):381–393, 1998.

[42] Thomas Whitmore Kornack. *A test of CPT and Lorentz symmetry using a K-3He co-magnetometer*. PhD thesis, Princeton University Princeton, NJ, USA, 2005.

[43] TW Kornack and MV Romalis. Dynamics of two overlapping spin ensembles interacting by spin exchange. *Physical review letters*, 89(25):253002, 2002.

[44] TW Kornack, RK Ghosh, and MV Romalis. Nuclear spin gyroscope based on an atomic comagnetometer. *Physical review letters*, 95(23):230801, 2005.

[45] Chip-scale absolute scalar magnetometer for space applications. http://www.jhuapl.edu/techdigest/TD/td2803/38KorthChip.pdf. Accessed: 2017-09-30.

[46] Dmitry Budker and Michael Romalis. Optical magnetometry. *Nature Physics*, 3(4):227–234, 2007.

[47] Christopher J. Foot. *Atomic Physics*. Oxford University Press, 2005.

[48] W Dentröder and Molecules Atoms. Photons: An introduction to atomic-, molecular-and quantum physics (graduate texts in physics), 2010.

[49] Hattie Lucille Ring. *Applications of Atomic Magnetometry and Hyperpolarized Xenon*. University of California, Berkeley, 2012.

[50] Daniel A. Steck. Cesium D line data, 1998.

[51] Georg Bison. *Development of an optical cardio-magnetometer*. PhD thesis, Université de Fribourg, 2004.

[52] William M Haynes. *CRC handbook of chemistry and physics*. CRC press, 2014.

[53] Gordon Kemble Woodgate. Elementary atomic structure. 1970.

[54] Gregory Breit and II Rabi. Measurement of nuclear spin. *Physical Review*, 38(11):2082, 1931.

[55] Almanac Bruker. Analytical tables and product overview, 2011.

[56] Peter J Mohr and Barry N Taylor. The fundamental physical constants. *Physics Today*, 2000.

[57] Norman Ramsey. *Molecular beams*, volume 20. Oxford University Press, 1956.

[58] A Ben-Amar Baranga, S Appelt, CJ Erickson, AR Young, and W Happer. Alkali-metal-atom polarization imaging in high-pressure optical-pumping cells. *Physical Review A*, 58(3):2282, 1998.

[59] Brian Julsgaard, Jacob Sherson, JL Sørensen, and Eugene S Polzik. Characterizing the spin state of an atomic ensemble using the magneto-optical resonance method. *Journal of Optics B: Quantum and Semiclassical Optics*, 6(1):5, 2003.

[60] R Gartman and W Chalupczak. Amplitude-modulated indirect pumping of spin orientation in low-density cesium vapor. *Physical Review A*, 91(5):053419, 2015.

[61] NV Vitanov, BW Shore, L Yatsenko, K Böhmer, T Halfmann, T Rickes, and K Bergmann. Power broadening revisited: theory and experiment. *Optics communications*, 199(1):117–126, 2001.

[62] Daryl W Preston. Doppler-free saturated absorption: Laser spectroscopy. *American Journal of Physics*, 64(11):1432–1436, 1996.

[63] AJ Hachtel, JD Kleykamp, DG Kane, MD Marshall, BW Worth, JT Barkeloo, JCB Kangara, JC Camenisch, MC Gillette, and S Bali. An undergraduate measurement of radiative broadening in atomic vapor. *American Journal of Physics*, 80(8):740–743, 2012.

[64] Miles Padgett and L Allen. Light with a twist in its tail. *Contemporary Physics*, 41(5):275–285, 2000.

[65] Miles Padgett, Johannes Courtial, and Les Allen. Light's orbital angular momentum. *Physics Today*, 57(5):35–40, 2004.

[66] William H McMaster. Polarization and the stokes parameters. *American Journal of Physics*, 22(6):351–362, 1954.

[67] Edward Collett. The description of polarization in classical physics. *American Journal of Physics*, 36(8):713–725, 1968.

[68] Sonja Franke-Arnold. Optical angular momentum and atoms. *Phil. Trans. R. Soc. A*, 375(2087):20150435, 2017.

[69] Alfred Kastler. Quelques suggestions concernant la production optique et la détection optique d'une inégalité de population des niveaux de quantifigation spatiale des atomes. application à l'expérience de stern et gerlach et à la résonance magnétique. *J. phys. radium*, 11(6):255–265, 1950.

[70] Alfred Kastler. Optical methods of atomic orientation and of magnetic resonance. *JOSA*, 47(6):460–465, 1957.

[71] Claude Cohen-Tannoudji and Alfred Kastler. I optical pumping. *Progress in optics*, 5:1–81, 1966.

[72] Marcis Auzinsh, Dmitry Budker, and Simon Rochester. *Optically polarized atoms: understanding light-atom interactions*. Oxford University Press, 2010.

[73] V. Tiporlini and K. Alameh. High sensitivity optically pumped quantum magnetometer. *The Scientific World Journal*, 2013:1–8, 2013.

[74] V. Tiporlini and K. Alameh. High sensitivity optically pumped quantum magnetometer. *The Scientific World Journal*, 2013:1–8, 2013.

[75] SB Bayram and R Marhatta. Anisotropy-dependent circular polarization spectroscopy. *Physical Review A*, 78(3):033403, 2008.

[76] Oleg Igorevich Popov. *Quantum beat spectroscopy of hyperfine structure in the 8p2P3/2 level of atomic cesium*. PhD thesis, Miami University, 2012.

[77] Claire Vallance. Generation, characterisation, and applications of atomic and molecular alignment and orientation. *Physical Chemistry Chemical Physics*, 13(32):14427–14441, 2011.

[78] Witold Chalupczak, Rachel M Godun, Paweł Anielski, Adam Wojciechowski, Szymon Pustelny, and Wojciech Gawlik. Enhancement of op-

tically pumped spin orientation via spin-exchange collisions at low vapor density. *Physical Review A*, 85(4):043402, 2012.

[79] IM Savukov and MV Romalis. Effects of spin-exchange collisions in a high-density alkali-metal vapor in low magnetic fields. *Physical Review A*, 71(2):023405, 2005.

[80] Brian Julsgaard. *Entanglement and quantum interactions with macroscopic gas samples*. PhD thesis, Aarhus Universitetsforlag, 2003.

[81] Stark effect in atomic spectra. http://hyperphysics.phy-astr.gsu.edu/hbase/Atomic/stark.html. Accessed: 2017-09-30.

[82] M Arditi and TRt Carver. Pressure, light, and temperature shifts in optical detection of 0-0 hyperfine resonance of alkali metals. *Physical Review*, 124(3):800, 1961.

[83] Fam Le Kien, Philipp Schneeweiss, and Arno Rauschenbeutel. Dynamical polarizability of atoms in arbitrary light fields: general theory and application to cesium. *The European Physical Journal D*, 67(5):92, 2013.

[84] BS Mathur, H Tang, and W Happer. Light shifts in the alkali atoms. *Physical Review*, 171(1):11, 1968.

[85] Elena Zhivun. *Vector AC Stark shift in 133 Cs atomic magnetometers with antirelaraxion coated cells*. University of California, Berkeley, 2016.

[86] Claude Cohen-Tannoudji and Jacques Dupont-Roc. Experimental study of zeeman light shifts in weak magnetic fields. *Physical Review A*, 5(2):968, 1972.

[87] Witold Chalupczak, Adam Wojciechowski, Szymon Pustelny, and Wojciech Gawlik. Competition between the tensor light shift and nonlinear zeeman effect. *Physical Review A*, 82(2):023417, 2010.

[88] Graham Thomas Purves. *Absorption and dispersion in atomic vapours: applications to interferometery*. PhD thesis, Durham University, 2006.

[89] DA Van Baak. Resonant faraday rotation as a probe of atomic dispersion. *American Journal of Physics*, 64(6):724–735, 1996.

[90] BEA Saleh and MC Teich. Fundamental of photonics, ch 5, 1991.

[91] Amnon Yariv. *Optical electronics*. Holt, Rinehart and Winston, 1985.

[92] Philippe Grangier, Juan Ariel Levenson, and Jean-Philippe Poizat. Quantum non-demolition measurements in optics. *Nature*, 396(6711):537, 1998.

[93] A Kuzmich, L Mandel, J Janis, YE Young, R Ejnisman, and NP Bigelow. Quantum nondemolition measurements of collective atomic spin. *Physical Review A*, 60(3):2346, 1999.

[94] Vladimir B Braginsky, Vladimir Borisovich Braginskiĭ, and Farid Ya Khalili. *Quantum measurement*. Cambridge University Press, 1995.

[95] Slichter Charles P. Principles of magnetic resonance: with examples from solid state physics, 1963.

[96] Robert Thornton Schumacher. *Introduction to magnetic resonance: principles and applications*, volume 1. WA Benjamin, 1970.

[97] William E Bell and Arnold L Bloom. Optically driven spin precession. *Physical Review Letters*, 6(6):280, 1961.

[98] IM Savukov, SJ Seltzer, MV Romalis, and KL Sauer. Tunable atomic magnetometer for detection of radio-frequency magnetic fields. *Physical review letters*, 95(6):063004, 2005.

[99] S-K Lee, KL Sauer, SJ Seltzer, O Alem, and MV Romalis. Subfemtotesla radio-frequency atomic magnetometer for detection of nuclear quadrupole resonance. *Applied Physics Letters*, 89(21):214106, 2006.

[100] W Chalupczak, RM Godun, S Pustelny, and W Gawlik. Room temperature femtotesla radio-frequency atomic magnetometer. *Applied Physics Letters*, 100(24):242401, 2012.

[101] I Savukov, T Karaulanov, and MG Boshier. Ultra-sensitive high-density rb-87 radio-frequency magnetometer. *Applied Physics Letters*, 104(2):023504, 2014.

[102] Timo Varpula and Torsti Poutanen. Magnetic field fluctuations arising from thermal motion of electric charge in conductors. *Journal of applied physics*, 55(11):4015–4021, 1984.

[103] B Chéron, H Gilles, J Hamel, O Moreau, and E Noel. A new optical pumping scheme using a frequency modulated semi-conductor laser for ^4he magnetometers. *Optics communications*, 115(1-2):71–74, 1995.

[104] B Chéron, H Gilles, J Hamel, O Moreau, and E Noël. ^4he optical pumping with frequency modulated light. *Journal de Physique II*, 6(2):175–185, 1996.

[105] B Chéron, H Gilles, and J Hamel. Spatial frequency isotropy of an optically pumped 4 he magnetometer. *The European Physical Journal-Applied Physics*, 13(2):143–145, 2001.

[106] D Budker, DF Kimball, VV Yashchuk, and M Zolotorev. Nonlinear magneto-optical rotation with frequency-modulated light. *Physical Review A*, 65(5):055403, 2002.

[107] Wojciech Gawlik, Leszek Krzemień, Szymon Pustelny, D Sangla, Jerzy Zachorowski, M Graf, AO Sushkov, and D Budker. Nonlinear magneto-optical rotation with amplitude modulated light. *Applied physics letters*, 88(13):131108, 2006.

[108] H Gilles, B Cheron, and J Hamel. ^4he optical pumping with polarization modulated light. *Optics communications*, 81(6):369–374, 1991.

[109] Harald Klepel and Dieter Suter. Transverse optical pumping with polarization-modulated light. *Optics communications*, 90(1-3):46–50, 1992.

[110] A Ben-Kish and MV Romalis. Dead-zone-free atomic magnetometry with simultaneous excitation of orientation and alignment resonances. *Physical review letters*, 105(19):193601, 2010.

[111] M Huang and JC Camparo. Coherent population trapping under periodic polarization modulation: Appearance of the cpt doublet. *Physical Review A*, 85(1):012509, 2012.

[112] Ilja Fescenko, Paul Knowles, Antoine Weis, and Evelina Breschi. A bell-bloom experiment with polarization-modulated light of arbitrary duty cycle. *Optics express*, 21(13):15121–15130, 2013.

[113] MV Balabas, D Budker, J Kitching, PDD Schwindt, and JE Stalnaker. Magnetometry with millimeter-scale antirelaxation-coated alkali-metal vapor cells. *JOSA B*, 23(6):1001–1006, 2006.

[114] Szymon Pustelny, Adam Wojciechowski, Michael Gring, Mateusz Kotyrba, Jerzy Zachorowski, and Wojciech Gawlik. Magnetometry based on nonlinear magneto-optical rotation with amplitude-modulated light. *Journal of Applied Physics*, 103(6):063108, 2008.

[115] SJ Seltzer, PJ Meares, and MV Romalis. Synchronous optical pumping of quantum revival beats for atomic magnetometry. *Physical Review A*, 75(5):051407, 2007.

[116] SJ Seltzer and MV Romalis. Unshielded three-axis vector operation of a spin-exchange-relaxation-free atomic magnetometer. *Applied physics letters*, 85(20):4804–4806, 2004.

[117] J Belfi, G Bevilacqua, V Biancalana, Y Dancheva, and L Moi. All optical sensor for automated magnetometry based on coherent population trapping. *JOSA B*, 24(7):1482–1489, 2007.

[118] A. Wickenbrock, F. Tricot, and F. Renzoni. Magnetic induction measurements using an all optical 87Rb atomic magnetometer. *Applied Physics Letters*, 103, 2013.

[119] John B Johnson. Thermal agitation of electricity in conductors. *Nature*, 119(2984):50–51, 1927.

[120] John Bertrand Johnson. Thermal agitation of electricity in conductors. *Physical review*, 32(1):97, 1928.

[121] Jennifer Eve Hoffman. *A Search for Alternative Electronic Order in the High Temperature Superconductor Bi2Sr2CaCu2O+ [delta] by Scanning Tunneling Microscopy*. PhD thesis, University of California, Berkeley, 2003.

[122] H Warren Moos and Richard H Sands. Study of spin-exchange collisions in vapors of rb 85, rb 87, and cs 133 by paramagnetic resonance. *Physical Review*, 135(3A):A591, 1964.

[123] ND Bhaskar, J Pietras, J Camparo, W Happer, and J Liran. Spin destruction in collisions between cesium atoms. *Physical Review Letters*, 44(14):930, 1980.

[124] Robert A Bernheim. Spin relaxation in optical pumping. *The Journal of Chemical Physics*, 36(1):135–140, 1962.

[125] Robert J McNeal. Disorientation cross sections in optical pumping. *The Journal of Chemical Physics*, 37(11):2726–2727, 1962.

[126] Norman F Ramsey. Resonance experiments in successive oscillatory fields. *Review of Scientific Instruments*, 28(1):57–58, 1957.

[127] HG Robinson, ES Ensberg, and HG Dehmelt. Preservation of spin state in free atom-inert surface collisions. *Bull. Am. Phys. Soc*, 3(9), 1958.

[128] RP Photonics. Distributed bragg reflector lasers. *Encyclopedia of Laser Physics and Technology*, 2006.

[129] SD Roh, RB Swint, and JJ Coleman. Distributed bragg reflector lasers. *Wiley Encyclopedia of Electrical and Electronics Engineering*, 1999.

[130] D2-100-dbr laser module. http://www.vescent.com/products/lasers/d2-100-dbr-laser/. Accessed: 2017-09-30.

[131] D2-210-spectroscopy module. http://www.vescent.com/manuals/doku.php?id=d2:spectroscopy_module_210. Accessed: 2017-09-30.

[132] Doppler-free saturated absorption spectroscopy: Laser spectroscopy. http://massey.dur.ac.uk/resources/grad_skills/LaserSpectroscopy.pdf. Accessed: 2017-09-30.

[133] D2-135 offset phase lock servo. http://www.vescent.com/products/electronics/d2-135-offset-phase-lock-servo/. Accessed: 2017-09-30.

[134] D2-135 offset phase lock servo. http://www.vescent.com/manuals/doku.php?id=d2:offset_phase_lock_servo. Accessed: 2017-09-30.

[135] D2-150 heterodyne module. http://www.vescent.com/products/electro-optics/d2-150-heterodyne-module/. Accessed: 2017-09-30.

[136] DJ McCarron. A guide to acousto-optic modulators. Technical report, Technical report, Durham University, 2007.

[137] 3080-120 specifications. https://goochandhousego.com/wp-content/pdfs/3080_120_99_48201_11rF.pdf. Accessed: 2017-09-30.

[138] EA Donley, TP Heavner, F Levi, MO Tataw, and SR Jefferts. Double-pass acousto-optic modulator system. *Review of Scientific Instruments*, 76(6):063112, 2005.

[139] IP Kaminow. Polarization-maintaining fibers. In *New directions in guided wave and coherent optics*, pages 209–224. Springer, 1984.

[140] Polarization-maintaining single mode optical fiber. https://www.thorlabs.com/newgrouppage9.cfm?objectgroup_id=1596. Accessed: 2017-09-30.

[141] Mounted glan-thompson polarizers. https://www.thorlabs.com/newgrouppage9.cfm?objectgroup_id=5707. Accessed: 2017-11-03.

[142] Eric W Weisstein. Steinmetz solid. 2005.

[143] Branislav KuzmanovicZoran BausSrete Nikolovski. Multi–layered spherical magnetic shielding. *Journal of Electrical Engineering*, 60(6):350–353, 2009.

[144] TJ Sumner, JM Pendlebury, and KoF Smith. Convectional magnetic shielding. *Journal of Physics D: Applied Physics*, 20(9):1095, 1987.

[145] Helmholtz coils. http://physicsx.pr.erau.edu/HelmholtzCoils/. Accessed: 2017-09-30.

[146] Helmholtz coils. http://physicsx.pr.erau.edu/HelmholtzCoils/. Accessed: 2017-11-12.

[147] Serge Huard. Polarization of light. *Polarization of Light, by Serge Huard, pp. 348. ISBN 0-471-96536-7. Wiley-VCH, January 1997.*, 1, 1997.

[148] Luke HC Patterson, Kenneth E Kihlstrom, and Michael A Everest. Balanced polarimeter: A cost-effective approach for measuring the polarization of light. *American Journal of Physics*, 83(1):91–94, 2015.

[149] M Bouchiat, D Chauvat, J Guéna, Ph Jacquier, M Lintz, and MD Plimmer. High precision balanced mode polarimetry with a pulsed laser beam. *Optics communications*, 119(3-4):403–414, 1995.

[150] Dmitry Budker, W Gawlik, DF Kimball, SM Rochester, VV Yashchuk, and A Weis. Resonant nonlinear magneto-optical effects in atoms. *Reviews of modern physics*, 74(4):1153, 2002.

[151] J Belfi, G Bevilacqua, V Biancalana, S Cartaleva, Y Dancheva, K Khanbekyan, and L Moi. Dual channel self-oscillating optical magnetometer. *JOSA B*, 26(5):910–916, 2009.

[152] J Skalla, S Lang, and G Wäckerle. Magnetic resonance line shapes in optical pumping and light-shift experiments in alkali atomic vapors. *JOSA B*, 12(5):772–781, 1995.

[153] Szymon Pustelny. *Nonlinear magneto-optical effects*. PhD thesis, University of California at Berkeley, 2007.

[154] F Mitschke, R Deserno, W Lange, and J Mlynek. Magnetically induced optical self-pulsing in a nonlinear resonator. *Physical Review A*, 33(5):3219, 1986.

[155] W Chalupczak, P Josephs-Franks, S Pustelny, and W Gawlik. Optical–radio-frequency resonances free from power broadening. *Physical Review A*, 81(1):013422, 2010.

[156] S Appelt, A Ben-Amar Baranga, CJ Erickson, MV Romalis, AR Young, and W Happer. Theory of spin-exchange optical pumping of 3 he and 129 xe. *Physical Review A*, 58(2):1412, 1998.

[157] Introduction to acousto-optic modulators and deflectors. http://www.optoscience.com/maker/gooch/pdf/IntroductionAO.pdf. Accessed: 2017-09-30.

[158] EB Aleksandrov and VS Zapasskii. Magnetic resonance in the faraday rotation noise spectrum. *Zh. Eksp. Teor. Fiz*, 81:132–138, 1981.

[159] W. Chalupczak, R. M. Godun, S. Pustelny, and W. Gawlik. Room temperature femtotesla radio-frequency atomic magnetometer. *Applied Physics Letters*, 100:1–4, 2012.

[160] W Chalupczak and RM Godun. Near-resonance spin-noise spectroscopy. *Physical Review A*, 83(3):032512, 2011.

[161] SA Crooker, DG Rickel, AV Balatsky, and DL Smith. Spectroscopy of spontaneous spin noise as a probe of spin dynamics and magnetic resonance. *arXiv preprint cond-mat/0408107*, 2004.

[162] D Sheng, S Li, N Dural, and MV Romalis. Subfemtotesla scalar atomic magnetometry using multipass cells. *Physical review letters*, 110(16):160802, 2013.

[163] SJ Smullin, IM Savukov, G Vasilakis, RK Ghosh, and MV Romalis. Low-noise high-density alkali-metal scalar magnetometer. *Physical Review A*, 80(3):033420, 2009.

[164] Jingwei Sheng, Shuangai Wan, Yifan Sun, Rongshe Dou, Yuhao Guo, Kequan Wei, Kaiyan He, Jie Qin, and Jia-Hong Gao. Magnetoencephalography with a cs-based high-sensitivity compact atomic magnetometer. *Review of Scientific Instruments*, 88(9):094304, 2017.

[165] Igor Savukov and Malcolm G Boshier. A high-sensitivity tunable two-beam fiber-coupled high-density magnetometer with laser heating. *Sensors*, 16(10):1691, 2016.

[166] H Griffiths. Magnetic induction tomography. *Measurement science and technology*, 12(8):1126, 2001.

[167] Luca Marmugi and Ferruccio Renzoni. Optical magnetic induction tomography of the heart. *Scientific reports*, 6:23962, 2016.

[168] Luca Marmugi, Sarah Hussain, Cameron Deans, and Ferruccio Renzoni. Magnetic induction imaging with optical atomic magnetometers: towards applications to screening and surveillance. In *SPIE Proceedings*, volume 9652, 2015.

[169] H Griffiths, WR Stewart, and W Gough. Magnetic induction tomography: a measuring system for biological tissues. *Annals Of The New York Academy Of Sciences*, 873(1):335–345, 1999.

[170] Arne Wickenbrock, Sarunas Jurgilas, Albert Dow, Luca Marmugi, and Ferruccio Renzoni. Magnetic induction tomography using an all-optical 87 rb atomic magnetometer. *Optics letters*, 39(22):6367–6370, 2014.

[171] Deans C., Marmugi L., Hussain S., and Renzoni F. Electromagnetic induction imaging with a radio-frequency atomic magnetometer. *Applied Physics Letters*, 108, 2016.

[172] Renzoni F Deans C., Marmugi L. Through-barrier electromagnetic imaging with an atomic magnetometer. *Optics Express*, 25(15):17911–17917, 2017.

[173] G Miller, P Gaydecki, S Quek, M Zaid, and B Fernandes. A sensor for imaging steel in reinforced concrete structures and visualisation of surface corrosion, incorporating real-time dsp. *Insight-Non-Destructive Testing and Condition Monitoring*, 46(2):82–84, 2004.

[174] X Ma, AJ Peyton, SR Higson, and P Drake. Development of multiple frequency electromagnetic induction systems for steel flow visualization. *Measurement Science and Technology*, 19(9):094008, 2008.

[175] L Perez, J Le Hir, C Dolabdjian, and L Butin. Investigation in detection of fatigue cracks under rivet head airframe using improved gmr magnetometer in an eddy current system. *Journal of Electrical Engineering*, 55(10s):73–76, 2004.

[176] Lu Ma, Hsin-Yu Wei, and Manuchehr Soleimani. Pipelines inspection using magnetic induction tomography based on a narrowband pass filtering method. *Progress In Electromagnetics Research M*, 23:65–78, 2012.

[177] Brendan J Darrer, Joseph C Watson, Paul A Bartlett, and Ferruccio Renzoni. Electromagnetic imaging through thick metallic enclosures. *AIP Advances*, 5(8):087143, 2015.

[178] Brendan J Darrer, Joe C Watson, Paul Bartlett, and Ferruccio Renzoni. Magnetic imaging: a new tool for uk national nuclear security. *Scientific reports*, 5, 2015.

[179] Roberta Guilizzoni, Joseph C Watson, Paul Bartlett, and Ferruccio Renzoni.

Penetrating power of resonant electromagnetic induction imaging. *AIP Advances*, 6(9):095017, 2016.

[180] Jack Wood, Robert Ward, Chris Lloyd, Paul Tatum, Caroline Shenton-Taylor, Stuart Taylor, Gil Bagley, Maxim Joseph, and Joe C Watson. Effect of shielding conductivity on magnetic induction tomographic security imagery. *IEEE Transactions on Magnetics*, 53(4):1–6, 2017.

[181] CB Alcock, VP Itkin, and MK Horrigan. Vapour pressure equations for the metallic elements: 298–2500k. *Canadian Metallurgical Quarterly*, 23(3):309–313, 1984.